Constraining Cosmological Models of Dark Energy

PhD Memoir

Ivan Duran Sancho

Departament de Física

June 3, 2013

Per l'Anna, la Paula, la Laia i la Mariona; sou la meva vida.

Per la Paqui, la Maria i el Pepe; us ho dec tot.

Acknowledgments

I thank my supervisor Diego Pavón who gave me the chance of working in the amazing field of Cosmology. I am also indebted to him for his guidance and effort in stimulating and solving an ample variety of questions, his patience and time, and for reading and correcting the writing of this Memoir. I also thank my supervisor Fernando Atrio-Barandela for instilling in me his enthusiasm, his help in better understanding the physical processes; for encouraging me in computing more efficiently, and for his very cordial reception in Salamanca. Discussions with Bin Wang on dark energy perturbations have been very inspiring, and his guide and company very pleasant. Ramon Miquel has been of great aid in dealing with statistical problems. I also thank the Institute of Cosmology and Gravitation of the University of Portsmouth for warm hospitality during my stay there. Special thanks go to Marco Bruni and David Wands for their time and advice. Guido Walter Pettinari was of great help in guiding me through the CLASS code. I am not mentioning the rest of the ICG people because I dont wish to forget anyone, but all of them, without exception, were very kind to me. Likewise, I am indebted to Ninfa Radicella and Luca Parisi for fruitful discussions and nice friendship. Also to Gaetano Vilasi and Rosangela Canonico for their warm hospitality during my visits to the University of Salerno. I have enjoyed the friendship of Ignacio Gómez Portillo as well as his passion for physics and sociology. Xavier Álvarez has helped me much through my continuous visits. All the other members of unit of the statistical physics have been very helpful and kind. The chats with Pedro da Cunha Ferreira have been a pleasure and our lunch times really enjoyable. I acknowledge financial support from the Univesitat Autònoma de Barcelona through a PIF fellowship. I was also supported by the Ministerio Español de Ciencia e innovación under Grant No. FIS2009-13370-C02-01 and by the Direcció de Recerca de la Generalitat under Grant No. 2009SGR-00164. I also benefited from a fellowship to visit the ICG of the University of Portsmouth from the Agència de Gestió d'Ajuts Universitaris i de Recerca de la Generalitat de Catalunya through the program BG-DGR 2012 and from the ICG. During my visits to Salerno, I was also supported by an INFN/MICINN collaboration under Grant. No. AIC10-D-000481.

Contents

Notation and conventions

Here we introduce the notation and conventions to be used throughout this Memoir

- Except otherwise indicated, will be used units where $c = k_B = h = 1$.
- Metric signature $[-, +, +, +]$.
- Greek indices are for the four space-time coordinates; Latin indices are just for the spatial components.
- An overdot $\dot{(\,)}$ indicates derivative with respect to cosmic time, t.
- A prime $(\,)'$ denotes derivative with respect to conformal time, τ.
- When dealing with perturbations the background quantities will be noted by an overbar $\bar{(\,)}$.
- A semicolon ($T^{\mu\nu}{}_{;\mu}$) indicates covariant derivative; a coma ($T^{\mu\nu}{}_{,\mu}$) indicates partial derivative.
- 3-vectors are indicated by bold characters.
- A subscript 0 denotes the present value of the corresponding quantity.
- $\nabla^2 \equiv g^{i\,j}\partial_i\partial_j$.
- Symbols commonly used in this Memoir are shown in table 1.

Background

	Metric
$g_{\mu\nu}$	space-time metric tensor
$\gamma_{\mu\nu}$	3-space metric tensor
a	cosmic scale factor
κ	curvature of the 3-space; $\kappa = -1, 0, 1$
	Energy content
ρ	total energy density
ρ_A	energy density of the Ath energy component
H	Hubble factor, $H \equiv \frac{\dot{a}}{a}$
h	parameter for Hubble constant H_0, $H_0 \equiv 100h$ km s^{-1} Mpc^{-1}
$\mathcal{H}$	conformal Hubble factor, $\mathcal{H} \equiv \frac{a'}{a}$
P	total pressure
P_A	pressure of the Ath energy component
w_A	equation of state parameter of the Ath energy component
Ω_A	density parameter of the Ath component; $\Omega_A \equiv \frac{8\pi G}{3}\frac{\rho_A}{H^2}$
$c_{s\,A}$	effective speed of sound of the ith component $c^2_{s\,A} \equiv \frac{\delta P_A}{\delta \rho_A}$
$c_{a\,A}$	adiabatic speed of sound of the ith component $c^2_{a\,A} \equiv \frac{\dot{P}_A}{\dot{\rho}_A}$
	Distances
z	redshift; $z \equiv a^{-1} - 1$
χ	comoving distance
d_L	luminosity distance
d_A	angular diameter distance

Perturbations

	Metric
B	Amplitude of perturbations in the shift vector in a general gauge
E	Amplitude of anisotropic distortion of the constant time hypersurfaces in a general gauge
ψ	Amplitude of perturbations in the lapse function in a general gauge. Newtonian potential in longitudinal gauge
ϕ	Amplitude of perturbations in a unit 3-space volume in a general gauge. Scalar potential in longitudinal gauge
h_{ij}	metric perturbation in the synchronous gauge
h	trace of the metric perturbation in the synchronous gauge
η	traceless part of the metric perturbation in the synchronous gauge
	Energy content
$\bar{\rho}_A$	background energy density of the Ath component
$\delta\rho_A$	perturbed energy density of the Ath component
δ_A	density contrast of the Ath component; $\delta_A \equiv \frac{\delta\rho_A}{\bar{\rho}_A}$
$\bar{P}_A$	background pressure of the Ath component
δP_A	pressure perturbation of the Ath component
π_A	anisotropic stress perturbation of the Ath component

Table 1: Most frequently used symbols

Most Frequently Used Acronyms

- BAO ..... baryon acoustic oscillations
- CDM ..... cold dark matter
- CMB ..... cosmic microwave background
- COBE ..... Cosmic background explorer
- CPL ..... Chevallier-Polarski-Linder
- EoS ..... equation of state
- FLRW ..... Friedmann-Lemaître-Robertson-Walker
- HZ ..... Harrison-Zel'dovich
- IR ..... infra-red
- ISW ..... integrated Sachs-Wolfe
- ΛCDM ..... lambda-cold-dark-matter
- LSS ..... large scale structure
- SN Ia ..... supernovae type Ia
- SW ..... Sachs-Wolfe
- UV ..... ultraviolet
- WMAP ..... Wilkinson-microwave-anisotropy-probe

Chapter 1

Introduction

Nowadays the Universe appears to be undergoing a phase of accelerated expansion, as witnessed by supernovae data [1], [2], and later corroborated by a host a cosmological measurements -very recently by the Planck satellite [3]. While this expansion can be described in Einstein's theory of gravity by invoking the existence of a positive but exceedingly small cosmological constant, Λ, connected to the quantum vacuum, many alternative, and sometimes sophisticated, explanations have been proposed [4].

Roughly, the energy content of the present universe can be split into 5% of baryonic matter and 95% of a non-visible (dubbed the "dark sector" because its components do not interact electromagnetically) whose 25% consists of non-relativistic, weakly interacting massive particles ("cold dark matter") and a 75% of a component with a huge negative pressure, the so-called "dark energy". The nature of the latter component is completely unknown; this justifies that many "trial" candidates have been proposed. By far, the simplest and most successful one is the cosmological constant, mentioned above. However, it suffers from two main drawbacks at the theoretical level: the coincidence problem and the fine tuning problem. The aim of this Memoir is to propose and constrain cosmological models of dark energy that circumvent these difficulties.

This Memoir is organized as follows: The next three Chapters (§2, §3 and §4) introduce basic concepts widely used when considering the different models that conforms our research work. The following Chapters focus on the different cosmological models.

In §5 dark energy is considered connected to the holographic principle and posits that it interacts (also non-gravitationally) with dark matter. The holographic principle sets a length scale, in this case the Hubble length, i.e.,

the scale of the causally connected events.

In §6 the previous model is studied more deeply and an alternative to it is presented. Both models share identical background evolution but each component behaves differently, which induces a diverse behavior at the perturbative level. This allows to observationally discriminate one model from the other.

A further holographic dark energy model is proposed in §7; this one based on the Ricci length (i.e., the maximum size a perturbation can have leading to a black hole). Again, a non-gravitational interaction is assumed between dark energy and dark matter.

In §8, a unified dark model (featuring a unification between dark matter ad dark energy) previously proposed is studied. Since the parameter space that fits the observational data is very narrow (and also in view of its theoretical interest), we decompose the single energy component into cold dark matter and quantum vacuum interacting with one another. As a consequence the allowed parameter space gets substantially augmented.

Although the models mentioned above mimic at the background level the standard ΛCDM model, the dark components evolve very differently. To rigorously study them, the numerical codes for the cosmological perturbations must be suitably modified, with the drawback of notably increasing the computational time. This is much alleviated in §9 where a novel method to calculate the matter power spectrum of dark energy models is proposed.

Finally, in §10 three model independent parameterizations of the deceleration parameter, based on solid thermodynamic arguments, are proposed and contrasted with the observational data.

In order not to burden the main text with calculations, the most conventional ones have been relegated to six appropriate Appendices.

Chapter 2

The homogeneous and isotropic Universe

According to the cosmological principle, our solar system does not take a privileged position in the Universe. Observational data from the COsmic Background Explorer (COBE) [5] satellite showed that the radiations reaching us from different directions of the sky is highly isotropic, with variations of the order of one part in one hundred thousand. This has been confirmed by the satellite probes Wilkinson Microwave Anisotropy Probe (WMAP) [6] and Planck [7]. As the Universe we see is isotropic at large scales and our position must be equivalent to any other, as a working hypothesis we assume that the Universe is extremely homogeneous and isotropic[1] at sufficiently big scales (about 200 Mpc and beyond). Then, to the space-time corresponds a spherically (maximally) symmetric and homogeneous geometry [8], described by the Friedmann-Lemaître-Robertson-Walker (FLRW) metric

$$ds^2 = -dt^2 + a^2(t)\left[\frac{dr^2}{1-\kappa r^2} + r^2\left(d\theta^2 + \sin^2\theta d\phi^2\right)\right] , \tag{2.1}$$

or, equivalently,

$$ds^2 = a^2(\tau)\left[-d\tau^2 + \frac{dr^2}{1-\kappa r^2} + r^2\left(d\theta^2 + \sin^2\theta d\phi^2\right)\right] , \tag{2.2}$$

where ds is the space-time interval separating two neighboring events, $a(t)$ is the scale factor that describes the expansion of the Universe, and the cosmic time t is related to conformal time τ by $dt = a(\tau)d\tau$. κ is the curvature

[1] In [8], chapter 13, it is demonstrated that any space isotropic about every point is also homogeneous.

of the 3-space and is normalized so that $\kappa = -1$ for the negatively curved (open) universes, $\kappa = 0$ for the flat, and $\kappa = 1$ for the positively curved (closed) ones.
The change of coordinates $d\chi \equiv \frac{dr}{\sqrt{1-\kappa r^2}}$ (where χ describes the physical distance regardless of the curvature of the 3-space), brings the metric (2.1) into

$$ds^2 = -dt^2 + a^2(t)\left[d\chi^2 + f^2(\chi)\left(d\theta^2 + \sin^2\theta d\phi^2\right)\right] , \tag{2.3}$$

where

$$\chi = \begin{cases} \arcsin r & (\kappa = +1) \\ r & (\kappa = 0) \\ \operatorname{arcsinh} r & (\kappa = -1) \end{cases} \quad \text{and} \quad f(\chi) = \begin{cases} \sin\chi & (\kappa = +1) \\ \chi & (\kappa = 0) \\ \sinh\chi & (\kappa = -1) \end{cases} . \tag{2.4}$$

From eq. (2.3), it is easy to understand why a Universe with $\kappa = +1$ is called closed, since the volume of the entire 3-space is finite, flat for $\kappa = 0$ as it is the familiar Euclidian 3-space, and open for $\kappa = -1$ since its volume its infinite as in the flat case, but the geometry is the one of an hyperboloid embedded in a 4-dimensional Lorentzian space[2].

2.1 Unperturbed Einstein field equations

According to Wheeler, "space tells matter how to move, and matter tells space how to curve" [9]. This is described by Einstein equations

$$G^{\mu\nu} = 8\pi G T^{\mu\nu} , \tag{2.5}$$

which imply the conservation of energy and momentum

$$T^{\mu\nu}_{\ \ ;\nu} = 0 , \tag{2.6}$$

via the Bianchi identities. The left hand side of eq. (2.5) describes the geometry of space time through the Einstein tensor

$$G^{\mu\nu} \equiv R^{\mu\nu} - \frac{1}{2} g^{\mu\nu} R , \tag{2.7}$$

that can be obtained from the Ricci tensor $R^{\mu\nu}$ and the Ricci scalar R, by contracting indices (once and twice, respectively) of the Riemann tensor

$$R^{\alpha}_{\mu\nu\beta} \equiv \Gamma^{\alpha}_{\mu\nu,\beta} - \Gamma^{\alpha}_{\mu\beta,\nu} + \Gamma^{\lambda}_{\mu\nu}\Gamma^{\alpha}_{\beta\lambda} - \Gamma^{\lambda}_{\mu\beta}\Gamma^{\alpha}_{\nu\lambda} , \tag{2.8}$$

$$R_{\mu\nu} \equiv R^{\alpha}_{\mu\alpha\nu} , \tag{2.9}$$

$$R \equiv g^{\mu\nu} R_{\mu\nu} . \tag{2.10}$$

[2] See §2.2 of [10]

On their part, the Christoffel symbols are defined from the metric as

$$\Gamma^{\alpha}_{\mu\nu} \equiv \frac{1}{2} g^{\alpha\beta} \left(g_{\beta\nu,\mu} + g_{\mu\beta,\nu} - g_{\mu\nu,\beta} \right) \ . \tag{2.11}$$

So, the left hand side of equation (2.5), can be obtained from the metric tensor $g_{\mu\nu}$. The right hand side of eq. (2.5), the stress-energy tensor, accounts for the energy content of matter and fields, and is the source of the gravitational field. Besides being homogeneous and isotropic at large scales, the energy content of the Universe is usally described by a mixture of perfect fluids, each one with stress-energy tensor given by

$$T^{\mu\nu}_{A} = (\rho_A + P_A) u^{\mu} u^{\nu} + P_A g^{\mu\nu} \qquad \text{(A=1,2,...,n)}, \tag{2.12}$$

where $u^{\mu} = \left[\frac{1}{a}, 0, 0, 0 \right]$ is the four-velocity of the fluids, with $u_{\mu} u^{\mu} = -1$, which is shared by every energy component. The quantities P_A and ρ_A denote the pressure and energy density of the components, respectively. The total stress-energy tensor will then be

$$T^{\mu\nu} = \sum_{A=1}^{n} T^{\mu\nu}_{A} \ . \tag{2.13}$$

Projecting $T^{\mu\nu}$ in the parallel and normal directions to u^{μ} the total energy density and pressure are

$$T^{0}_{0} = -\rho \qquad , \qquad T^{i}_{j} = P \delta^{i}_{j} \ , \tag{2.14}$$

respectively, with δ^{i}_{j} the Kronecker delta. The 00 and ii components of the Einstein tensor defined by eq. (2.7) are

$$G^{0}{}_{0} = -3 \left[\left(\frac{\dot{a}}{a} \right)^2 + \frac{\kappa}{a^2} \right] \ , \tag{2.15}$$

$$G^{i}{}_{j} = -2 \frac{\ddot{a}}{a} - \left[\left(\frac{\dot{a}}{a} \right)^2 + \frac{\kappa}{a^2} \right] \delta^{i}_{j} \ . \tag{2.16}$$

All geometric quantities in the FLRW metric are displayed in appendix A.1. From eqs. (2.14) - (2.16) we solve the 00 and ii component of eq. (2.5) to obtain the Friedmann equation

$$\left(\frac{\dot{a}}{a} \right)^2 = \frac{8\pi G}{3} \rho - \frac{\kappa}{a^2} \ , \tag{2.17}$$

and the Raychaudhuri equation (also called 2nd Friedmann equation)

$$\frac{\ddot{a}}{a} = -\frac{4\pi G}{3}(\rho + 3P) \ . \tag{2.18}$$

Here, for later use, we introduce the deceleration parameter $q \equiv -\ddot{a}a/\dot{a}^2$. For $q > 0$ ($q < 0$), the Universe decelerates (accelerates) its expansion. Using eqs. (2.17) and (2.18), last expression can be recast as

$$q = -1 - \frac{\dot{H}}{H^2} \ . \tag{2.19}$$

2.2 Conservation equations for non interacting fluids

By using the stress-energy tensor of different perfect fluids, eq.(2.12), in the conservation equation (2.6) with the FLRW metric (2.1) we obtain

$$T_A^{\mu\nu}{}_{;\mu} = T_A^{\mu\nu}{}_{,\mu} + \Gamma^{\mu}_{\alpha\mu} T_A^{\alpha\nu} + \Gamma^{\nu}_{\alpha\mu} T_A^{\mu\alpha} = 0 \ , \tag{2.20}$$

where A stands for the different fluids (radiation, baryons, cold dark matter, dark energy, ...) which we assume are separately conserved. If we consider just the 00 component of the equations (2.20), it follows

$$T_A^{\mu 0}{}_{;\mu} = T_A^{\mu 0}{}_{,\mu} + \Gamma^{\mu}_{\alpha\mu} T_A^{\alpha 0} + \Gamma^{0}_{\alpha\mu} T_A^{\mu\alpha} = 0 \ , \tag{2.21}$$

and substituting the expression of the Christoffel symbols of the unperturbed FLRW metric (appendix A.1), we get

$$\dot{\rho}_A + 3H(1 + w_A)\rho_A = 0 \ , \tag{2.22}$$

where $H \equiv \frac{\dot{a}}{a}$ and w_A is the equation of state (EoS) parameter, given by $P_A = w_A \rho_A$. If, moreover w_A is a constant, after integration we obtain

$$\rho_A = a^{-3(w_A+1)} \ . \tag{2.23}$$

We consider the Universe filled with baryons (subscript B), that accounts for all the known non relativistic matter (including protons and neutrons and leptons), cold dark matter (subscript CDM), such as weakly interacting massive particles, and radiation (subscript R), that include all relativistic particles (photons, massless neutrinos, etc). Non relativistic matter and baryons have $w_{CDM} = w_B = 0$, while for radiation $w_R = \frac{1}{3}$. Therefore,

$$\rho_{CDM} = \rho_{CDM\,0} a^{-3} \ , \tag{2.24}$$

$$\rho_B = \rho_{B\,0} a^{-3} \ , \tag{2.25}$$

$$\rho_R = \rho_{R\,0} a^{-4} \ . \tag{2.26}$$

2.3 Conservation equations for interacting fluids

If some (or all) components interact with each other, the total stress-energy tensor will still be conserved, but not so the stress-energy tensor of the interacting component. Their (non) conservation equation reads

$$T_A^{\mu\nu}{}_{;\mu} = T_A^{\mu\nu}{}_{,\mu} + \Gamma^{\mu}_{\alpha\mu} T_A^{\alpha\nu} + \Gamma^{\nu}_{\alpha\mu} T_A^{\mu\alpha} = Q_A^{\mu} \, . \tag{2.27}$$

Then, $\sum_A Q_A^{\mu} = 0$. The interaction term at background level fulfills

$$Q_A^{\mu} = [Q_A, \mathbf{0}] \, , \tag{2.28}$$

where Q_A is a function of time to be specified. After solving eq. (2.27) in a similar manner to the non-interacting case, we obtain

$$\dot{\rho}_A + 3H(1 + w_A)\rho_A = Q_A \, , \tag{2.29}$$

that is the equation that describes the evolution of the mean density of interacting fluids.

2.4 The standard cosmological model

Nowadays, the simplest most successful model is the so-called ΛCDM. This model assumes Einstein's general relativity and considers that the energy density is contributed solely by pressureless matter, radiation and a cosmological constant, Λ. The latter is supposedly connected to the energy of the quantum vacuum [11] , though there is a severe fine tunning that will be commented on §2.4.1. It was first introduced by Einstein in 1917 to keep the Universe static. When inserted in the Einstein eq. (2.5), the Bianchi identities are fulfilled and so the total stress-energy tensor is also conserved. Since the metric is covariantly conserved, i.e., $g^{\mu\nu}_{;\nu} = 0$, we can add a term proportional to the metric and then (2.5) generalizes to

$$G^{\mu\nu} + \Lambda g^{\mu\nu} = 8\pi G T^{\mu\nu} \, . \tag{2.30}$$

After this, the Friedmann and Raychaudhuri equations read

$$\left(\frac{\dot{a}}{a}\right)^2 = \frac{8\pi G}{3}\rho - \frac{\kappa}{a^2} + \frac{\Lambda}{3} \, , \tag{2.31}$$

$$\frac{\ddot{a}}{a} = -\frac{4\pi G}{3}(\rho + 3P) + \frac{\Lambda}{3} \, . \tag{2.32}$$

Cosmological parameters of the ΛCDM model
$H_0 = 67.4 \pm 1.4$ km s^{-1} Mpc^{-1}
$\Omega_{CDM\,0} h^2 = 0.1196 \pm 0.0031$
$\Omega_{B\,0} h^2 = 0.022078 \pm 0.00033$
$\Omega_\Lambda = 0.686 \pm 0.0016$
$100\Omega_{K\,0} = -0.10^{+0.62}_{-0.65}$
$t_0 = 13.813 \pm 0.058$ Gyr
$z_\star = 1090.37 \pm 0.65$
$r_{s\,\star} = 144.75 \pm 0.66$

Table 2.1: Cosmological parameters for the ΛCDM model borrowed from [3]. $h \equiv H_0/100$. $z_\star$ is the recombination redshift at which electron and hydrogen nuclei formed atoms and the Universe became transparent to radiation, and $r_{s\,\star}$ the sound horizon at that time. $t_0 = \int_0^{a_0} \frac{da}{aH}$ is the age of the Universe.

The conservation equation follows from Friedmann equations (2.31) and (2.32) or through the conservation of the stress-energy tensor. In both cases we get

$$\rho_\Lambda = \rho_{\Lambda\,0} \ , \tag{2.33}$$

where $\rho_{\Lambda\,0} \equiv \frac{\Lambda}{8\pi G}$ and $w_\Lambda = -1$ through eq. (2.23). Thus, the quantum vacuum has a negative pressure. Introducing the fractional energy density, $\Omega_A = \frac{8\pi G}{3H^2}\rho_A$ we recast the first Friedman equation as

$$\Omega_{CDM} + \Omega_B + \Omega_R + \Omega_\Lambda + \Omega_\kappa = 1 \ , \tag{2.34}$$

where $\Omega_\kappa \equiv -\kappa/(aH)^2$.
At the end of the XXth century, two groups independently found (through observations of supernovae type Ia (SN Ia) [1, 2]), that the expansion of the Universe was accelerated at present, i.e., $\ddot{a}|_0 > 0$. This could not be explained within general relativity using matter and radiation as the only energy components. Some new component with negative pressure $P < -\frac{1}{3}\rho$ - see eq. (2.18) - was needed. The first, and so far the most successful candidate is the cosmological constant [3]. Within this model, the most recent values of the parameters that determine the cosmological evolution at the background level are listed in table 2.1.

2.4.1 Fine tunning problem

From the fractional energy density Ω_Λ and the cosmological data from table 2.1, the value of the energy density associated to the cosmological constant

results $\rho_\Lambda \approx 10^{26}\,\frac{kg}{m^3} \approx 10^{-47}\,GeV^4$. Quantum field theory relates Λ to the vacuum energy density as the sum of the zero-point energies of all the normal modes of a field of mass m as

$$\rho_\Lambda = \frac{1}{4\pi^2}\int_0^{k_{max}} dk k^2\sqrt{k^2+m^2} \approx \frac{k_{max}^4}{16\pi^2}\,, \tag{2.35}$$

where $k_{max} \simeq (8\pi G)^{-\frac{1}{2}}$ is the ultraviolet (UV) cutoff at which quantum field theory breaks down. If general relativity is to describe gravity up to Planck scales, then $\rho_\Lambda \approx \frac{(8\pi G)^{-2}}{16\pi^2} \approx 10^{74} GeV^4$. So, there is a difference of 121 orders of magnitude between the observed vacuum energy density and its quantum field value. A more conservative UV cutoff such as the energy scale of quantum chromo-dynamics, leads to discrepancies of about 60 orders of magnitude. Albeit the radiative contributions to the vacuum energy can be of either sign, a fine tunning of at least one part in 10^{60} remains. Approaches to solve the cosmological constant problem are considered in [12]. At the moment, no universally accepted argument exists by which Λ should take such non-vanishing low value.

2.4.2 The Coincidence problem

Equations (2.24), (2.25) and (2.33) tell us that the pressureless matter (baryons plus cold dark matter) and the vacuum energy densities evolve very differently. This means that when the hydrogen atoms formed, around $z_\star \approx 1100$, $r_\star \equiv \frac{\rho_{M\,\star}}{\rho_{\Lambda\,\star}} \approx 10^{11}$ while today the ratio between energy densities is $r_0 \equiv \frac{\rho_{M\,0}}{\rho_{\Lambda\,0}} \approx 1$. The fact that just recently the two energy densities became of the same order despite of evolving so differently is the so-called *Coincidence problem*, i.e., "why are the densities of matter and dark energy of the same order precisely today?" [13]. It is fair to add that anthropic arguments have been advanced to sustain the view that in reality the coincidence problem is not a problem at all - see e.g. [14]. However, these arguments are rather unattractive and not convincing.

2.5 Dark energy alternatives to the standard cosmological model

To solve the two above problems of the standard ΛCDM model, many other candidates to drive the accelerated expansion have been proposed. We divide them in two main groups: the first one includes those models based on general relativity that introduce exotic forms of energy components with

a huge negative pressure - the so-called dark energy. The second one comprehends those models that do not introduce exotic components but modify Einstein relativity. Amongst them, let us mention f(R) and f(T) proposals, massive gravity, quantum loop gravity, etc. - see [15] and references therein. We shall restrict ourselves to the first group; so we consider general relativity as the theory that correctly describes gravity from the Planck era onwards.

2.5.1 Quintessence

A first option is to consider dark energy (the energy component meant to accelerate the expansion thanks to its huge negative pressure) as the one corresponding to a canonical scalar field, ϕ_Q, [16, 17], dubbed "quintessence". It derives from the action

$$S = \int dx^4 \sqrt{-g} \left(\frac{R}{16\pi G} + \mathcal{L}_{SM} + \mathcal{L}_Q \right) , \tag{2.36}$$

where g is the determinant of the metric, R is the Ricci scalar and $\mathcal{L}_{SM}$ the Lagrangian of the particles in the Standard Model. $\mathcal{L}_Q$, the Lagrangian describing quintessence, is that of a canonical scalar field

$$\mathcal{L}_Q = -\frac{1}{2}\phi^Q_{;\mu}\phi^{;\mu}_Q - V(\phi_Q) \tag{2.37}$$

where $V(\phi_Q)$ is the potential. Introducing the Hilbert stress-energy tensor, $T_{\mu\nu} = \frac{2}{\sqrt{-g}}\frac{\delta(\sqrt{-g}\mathcal{L}_A)}{\delta g_{\mu\nu}} = 2\frac{\delta \mathcal{L}_A}{\delta g_{\mu\nu}} + g_{\mu\nu}\mathcal{L}_A$, where A is any energy component, one follows

$$T_{\mu\nu} = \phi^Q_{;\mu}\phi^Q_{;\nu} + g_{\mu\nu}\mathcal{L}_Q \ , \tag{2.38}$$

see [18] for details on Lagrangian formulation of general relativity. After this, the energy density and the pressure for quintessence turn out to be

$$\rho_{\phi_Q} = \frac{1}{2}\dot{\phi}^2_Q + V(\phi_Q) \ , \qquad P_Q = \frac{1}{2}\dot{\phi}^2_Q - V(\phi_Q) \ . \tag{2.39}$$

Every potential $V(\phi_Q)$ has an EoS parameter, w_Q, associated to it and vice versa; as well as an expansion history, $H(a)$. Last statement is true if, and only if, $\dot{\phi}_Q \neq 0$. To learn more about the state of the art see [17, 19, 20, 21, 22].

2.5.2 Phantom

Since many cosmological data are compatible with a value of the EoS of dark energy parameter, $w_X < -1$ Caldwell proposed a type of dark energy

dubbed "phantom" [23]. In these models the dominant energy condition is violated, i.e., $\rho_X + P_X < 0$. Phantom models are based on the action

$$S = \int dx^4 \sqrt{-g} \left(\frac{R}{16\pi G} + \mathcal{L}_{SM} + \mathcal{L}_P \right) , \tag{2.40}$$

where $\mathcal{L}_P$ stands for the phantom field Lagrangian, which has a non-canonical kinetic term

$$\mathcal{L}_P = \frac{1}{2} \phi^P_{;\mu} \phi_P^{;\mu} - V(\phi_P) . \tag{2.41}$$

Notice that the sign of the kinetic term has been varied with respect to the one in quintessence models (2.37). This gives rise to the following equations

$$\rho_P = -\frac{1}{2}\dot{\phi}_P^2 + V(\phi_P) , \qquad P_P = -\frac{1}{2}\dot{\phi}_P^2 - V(\phi_P) . \tag{2.42}$$

The phantom field climbs the potential instead of rolling down it to its minimum, i.e., the energy density augments with time rather than decreases. Since the Hamiltonian has no lower bound, the phantom field is unstable from the quantum point of view unless a cutoff at low energies is set [24]. Another characteristic of this kind of models is that there is a future singularity in the scale factor, called the big rip, at which the whole Universe rips apart [25]. In the literature there are many studies on phantom models. Some representative examples can be found in [26]. It is worth of mention that behind a quintessence or phantom scalar field, there can be a running cosmological constant arising from a fundamental quantum field theory [27]. Another group of models with non-canonical kinetic term, dubbed k-essence, was introduced in [28].

2.5.3 Holographic dark energy

This kind of models have become popular as they rest on the very reasonable assumption that the entropy of every bounded region of the Universe, of size L, should not exceed the entropy of a Schwarzschild black hole of the same size [29]. That is to say,

$$L^3 \Lambda^3 \leq S_{BH} \simeq M_P^2 L^2 \qquad \left(M_P^2 = (8\pi G)^{-1} \right) , \tag{2.43}$$

where Λ stands for the ultraviolet cutoff; the infrared cutoff is set by L. However, as demonstrated by Cohen *et al.* [30], an effective field theory that saturates the above inequality necessarily includes states for which the

Schwarzschild radius exceeds L. It is therefore natural to replace the said bound by another that excludes such states right away, namely,

$$L^3\Lambda^4 \leq M_P^2 L \ . \tag{2.44}$$

This bound guarantees that the energy $L^3\Lambda^4$ in a region of size L remains lower than the energy of a black hole of the same size [30]. By saturating the inequality (2.43) and identifying Λ^4 with the density of holographic dark energy, ρ_X, it follows that [31]

$$\rho_X = \frac{3c^2}{8\pi G L^2} \ , \tag{2.45}$$

where numerical factors are introduced for convenience and c^2 is a dimensionless quantity, usually assumed constant, introduced to encode the uncertainties present in the theory (such as the number particle species and so on). However, the latter parameter can vary with time [32, 33], if the variation is slow enough to preserve the holographic dependence, i.e., $\frac{dc^2}{dt} < \frac{dL^2}{dt}$. The relationship (2.45) is widely used in models of holographic dark energy that aim to explain the present stage of cosmic accelerated expansion, [32, 34, 35, 36, 37, 38, 39], via the huge negative pressure associated to them. Broadly speaking, holographic dark energy models fall into three main groups depending on the choice of the infrared cutoff, L. One is the Hubble radius [32], the length scale that describes the size over which physical processes operate causally

$$R_H = H^{-1} \ , \tag{2.46}$$

Another choice is the event horizon radius [31, 40],

$$R_{fe} = \int_t^\infty \frac{dt}{a} \ . \tag{2.47}$$

It correspond to the distance covered by light from the instant t up to the event horizon. However, this choice presents two severe problems: (i) It suffers from causality, i.e., today's energy density depends on the future evolution of the Universe rather than the other way around. (ii) It also suffers from circularity: to have acceleration as $t \to \infty$ is a necessary condition for the event horizon to exist.
Another option is to consider the Ricci (or causal) radius [36]

$$-R_{CC} = \left(\frac{R}{6}\right)^{-\frac{1}{2}} = \left(\dot{H} + 2H^2\right)^{-\frac{1}{2}} \ , \tag{2.48}$$

where R is the Ricci scalar. This scale describes the maximum size that a density perturbation can have in order to form a black hole [41]. The particle horizon radius was also used [34] but it presents the severe drawback of leading to a cosmology incompatible with a transition from deceleration to acceleration in the expansion of the Universe. It is to be emphasized that holographic models with dynamical length scales do not contain the ΛCDM model as a limiting case since the energy density of the quantum vacuum, being constant, cannot be holographic.

2.5.4 Unified models

Since neither the nature of dark matter nor dark energy is known, a more ambitious project is to unify them in a single component -see e.g. [42, 43, 44, 45, 46, 47]. In this case, the coincidence problem disappears, and the cosmological constant problem reduces to justify the vanishing of Λ. Here we shall briefly describe some of them. Possibly the most studied are the original Chaplygin gas [42] and the generalized Chaplygin model [43]. These can be derived from a generalized Nambu-Goto action in a perturbed d-brane in a (d + 1,1) spacetime. Its equation of state is

$$P_{Ch} = -\frac{\beta}{\rho_{Ch}^{\alpha}} \, , \tag{2.49}$$

and its energy density evolves with the scale factor as

$$\rho_{Ch} = \left(\beta + \frac{B}{a^{3(1+\alpha)}} \right)^{\frac{1}{1+\alpha}} \, , \tag{2.50}$$

where α and β are constant free parameters. For the original model [42], $\alpha = 1$. This energy density behaves as a cosmological constant in the far future, $a \to \infty$, and as cold dark matter in the past, $a \ll 1$. However, it has been shown that best fit value of the free parameter is very close to $\alpha = 0$, in which case the model reduces to the standard ΛCDM. But it is also a possible that $\alpha \approx 300$, which results in a behavior completely different from that of the standard model [44].
The model of Ref. [45] treats the dark sector as a barotropic fluid that experiences a transition from a Einstein-de Sitter [48] expansion in the past to a de Sitter one in the future, as in the previous case. The equation of state is

$$P_U = -\rho_\Lambda \left[\frac{1 - \tanh(\frac{\rho_U - \rho_t}{\rho_s})}{1 - \tanh(\frac{\rho_\Lambda - \rho_t}{\rho_s})} \right] \, , \tag{2.51}$$

where ρ_t is a constant energy scale at which the transition between the two regimes took place; the bigger ρ_t, the earlier the transition. ρ_s, another free parameter of the model, is related to the suddenness of the transition; the smaller ρ_s the faster it occurs. Lastly, ρ_Λ is just the asymptotic value of ρ_U. This model has two allowed regions in the parameter space. In one $\rho_s \leq \rho_t$ and the transition proceeds very fast. In the other, $\rho_s \geq \rho_t$ and the transition proceeds slowly. In both regions the ΛCDM is included as a limiting case. The model of Ref. [46] behaves similarly, but it describes the dark sector by a scalar field.

2.6 Distances

To determine distances in an expanding Universe it is of a great importance and not an easy matter. We first consider the comoving size to the horizon, τ, i.e., the distance traveled by light from the Big Bang ($t = 0$) up to now. It can be derived from the metric given in eq. (2.3) by setting $ds^2 = 0$. Then,

$$\tau = \int_0^t \frac{d\hat{t}}{a} \, . \tag{2.52}$$

If we just consider the light emitted by a source at a scale factor $a < a_0$, then the comoving distance traveled by it is

$$\chi(a) = \int_{t(a)}^t \frac{d\hat{t}}{a} = \int_{a_0}^a \frac{d\hat{a}}{\hat{a}^2 H} \, . \tag{2.53}$$

Typically distances are determined in astronomy by measuring the flux F received from a given source of known luminosity L. By definition, $F = \frac{L(\chi)}{4\pi\chi^2(a)}$ where the $L(\chi)$ is the luminosity observed in a shell of (comoving) size χ. The energy emitted by the source in a interval dt_1 is Ldt_1 and the one received is $L(\chi)dt_0$ with $\frac{dt_1}{a(t_1)} = \frac{dt_0}{a(t_0)}$. The energy of an emitted photon will be $\epsilon_1 = \frac{1}{a_1\lambda}$ and observed as $\epsilon_0 = \frac{1}{a_0\lambda}$; so the luminosities given off and received will be related by $L(\chi) = a_1^2 L$. So we can recast the flux as $F = \frac{La^2}{4\pi\chi^2(a)}$ and define the luminosity distance for spatially flat ($\kappa = 0$) models as

$$d_L \equiv \frac{\chi(a)}{a} = \frac{1}{a}\int_{t(a)}^t \frac{d\hat{t}}{a} = (1+z)\int_0^z \frac{d\hat{z}}{H(\hat{z})} \, , \tag{2.54}$$

where $z = (1/a) - 1$ is the redshift.
Another way to define distances in astronomy considers measuring the angle θ subtended by an object of physical size D in a flat Universe ($\kappa = 0$), that

due to the fact that the size we observe is enlarged by the expansion to a size aD, $d_A \equiv aD/\theta$. This distance is called angular diameter distance. The subtended observed angle is $\theta = \frac{aD}{a\chi}$, and so, the angular distance, with $\Omega_\kappa = 0$, results

$$d_A \equiv a\chi = a \int_{t(a)}^{t} \frac{d\hat{t}}{a} = \frac{1}{1+z} \int_0^z \frac{d\hat{z}}{H(\hat{z})} \, . \tag{2.55}$$

These magnitudes are very useful to fit dark energy models with observational data, SN Ia, BAO and X-ray in galaxy clusters. We will further elaborate on this point in §4.

Chapter 3

First order perturbation theory

In dealing with cosmological perturbations data, e.g., cosmic structures and anisotropies of the CMB one must, obviously, relax the assumption of isotropy and homogeneity. To do this one first perturbs the FLRW metric and then explores the consequences. We shall consider just small deviations from the metric of the background, i.e.,

$$g_{\mu\nu} = \bar{g}_{\mu\nu} + \delta g_{\mu\nu} \ , \tag{3.1}$$

where $\bar{g}_{\mu\nu}$ is the background FLRW metric described by eq. (2.2), and $\delta g_{\mu\nu}$ are small perturbations around the background. These perturbations fall in three different types: scalar, vectorial, and tensorial. At first order, these metric perturbations decouple from one another and can be treated separately. This can be easily seen as follows: the background quantities are all scalar since any vector or tensor would set a privileged direction, and break the isotropy assumption. In a scalar equation every term should be a scalar, and the same holds true for vector and tensor equations. Since first order terms can only be formed by background quantities multiplied by a perturbation term, the perturbations of different kind do not mix[1]. We shall restrict our analysis to first order in perturbation theory. Due to the fact that observations show that the spatial curvature of the Universe is very small, if at all [3], we just consider the case of a spatially flat Universe. Useful reviews on perturbation theory can be found in Refs. [50, 51, 52, 53].

[1] In §5.4 of [49] the decomposition of scalar and tensor types is demonstrated in a straightforward way. In appendix B of [50] is demonstrated for all cases.

3.1 Scalar metric perturbations

The most general form of scalar metric perturbations in conformal time is

$$\delta g_{\mu\nu} = a^2(\tau) \begin{pmatrix} 2\phi & -B_{,i} \\ -B_{,i} & 2\left(-\psi\delta_{ij} + E_{,ij}\right) \end{pmatrix} , \tag{3.2}$$

whence the corresponding line element takes the form

$$ds^2 = a^2(\tau)\left\{-(1+2\phi)d\tau^2 - 2B_{,i}dx^i d\tau + \left[(1-2\psi)\delta_{ij} + 2E_{,ij}\right]dx^i dx^j\right\} . \tag{3.3}$$

Since the density perturbations are the source of scalar metric perturbations, as shown in §3.4, they are the only type to be considered here, for they are decoupled from vector and tensor perturbations. Nevertheless, we next give a brief description of these two types.

3.2 Vector metric perturbations

Vector perturbations decay at large scales in an expanding Universe so they do not leave an observable imprint, and are not of a big interest in cosmology. Nevertheless, here we shall describe the vector type metric perturbations:

$$\delta g_{\mu\nu} = a^2(\tau) \begin{pmatrix} 0 & -S_i \\ -S_i & F_{i;j} + F_{j;i} \end{pmatrix} , \tag{3.4}$$

where $F_i{}^{;j} = S_i{}^{;j} = 0$ because the gradient is normal to a divergenceless vector, and then F_i or S_i cannot be expressed as a divergenceless vector plus the gradient of a scalar. If they could, the functions would not be pure vector perturbations.

3.3 Tensor metric perturbations

Although tensor perturbations can, in principle, be detected as CMB anisotropies on large scales [54], we will not consider them in much detail because we are just interested in density perturbations. The general metric for tensor perturbations is

$$\delta g_{\mu\nu} = a^2(\tau) \begin{pmatrix} 0 & 0 \\ 0 & h_{ij} \end{pmatrix} , \tag{3.5}$$

with the constraints $h^i{}_i = h_{ij}{}^{;j} = 0$ and $h_{ij} = h_{ji}$ to ensure, as in the case of vector perturbations, that they are purely tensorial. Tensor perturbations

are, at first order, gauge invariant quantities [50, 55]. Gauge invariance is considered below in §3.8. Summing up, the independent functions describing all types of metric perturbations are 10 in total (4 scalars, 4 vectorials and 2 tensorials), one for each independent component of the metric.

3.4 Perturbed Einstein field equations

By perturbing eq. (2.5) we get

$$\delta G^{\mu\nu} = 8\pi G \delta T^{\mu\nu} \ . \tag{3.6}$$

As before, the left hand side depends on the metric perturbations only, and the right hand side on the perturbations of the energy content of the Universe. All perturbations of the geometric functions are calculated in appendix A.2. We use the perturbed Einstein tensor, together with the perturbed stress-energy tensor of a fluid

$$T^{\mu\nu}_A = (\rho_A + P_A) u^\mu_A u^\nu_A + P_A g^{\mu\nu} + \pi^\mu_{\nu\ A} \ , \tag{3.7}$$

keeping in mind that $T^{\mu\nu} = \sum_A T^{\mu\nu}_A$. The total energy density and the pressure for every component is: $\rho_A = \bar{\rho}_A + \delta\rho_A$ and $P_A = \bar{P}_A + \delta P_A$. On the other hand, $\pi^\mu_{\nu\ A}$ ($\pi^0_{\nu\ A} = 0$ and $\pi^i_{j\ A} = \left(\partial^i\partial_j - \frac{1}{3}\delta^i_j\nabla^2\right)\pi_A$) denotes the anisotropic stress tensor. The expression for the perturbed four-velocity is

$$u^\mu = \frac{1}{a}\left[(1-\phi), v^{,i}\right] \ , \tag{3.8}$$

$$u_\mu = -a\left[(1+\phi), (v+B)_{,i}\right] \ , \tag{3.9}$$

where v is the scalar part of the velocity perturbation $v^i = v^{,i} + v^{\star i}$ (with $v^{\star i}_{;i} = 0$) and the expression of u^0 and u_i can be obtained through the metric (3.2) and the conditions $u_\mu u^\mu = -1$ and $u_i = g_{i\mu}u^\mu$, respectively. Using eqs. (3.2), (3.8) and (3.9) in eq. (3.7) we obtain the components of the stress-energy tensor, namely

$$T^0_{0\ A} = -(\bar{\rho}_A + \delta\rho_A) \ , \tag{3.10}$$

$$T^0_{i\ A} = (\bar{\rho}_A + \bar{P}_A) v_{,i\ A} \ , \tag{3.11}$$

$$T^i_{j\ A} = (\bar{P}_A + \delta P_A)\delta^i_j + \pi^i_{j\ A} \ . \tag{3.12}$$

Solving the perturbed Einstein field equations we get

$$3\mathcal{H}^2\phi + \mathcal{H}\nabla^2(B + E') + 3\mathcal{H}\psi' - \nabla^2\psi = -4\pi G a^2 \sum_A \delta\rho_A \ , \tag{3.13}$$

$$-\left(\mathcal{H}\phi+\psi'\right)_{,i}=\frac{a^2}{2}\sum_A(\bar{\rho}_A+\bar{P}_A)v_{,i\ A}\ , \tag{3.14}$$

$$\left[\left(2\mathcal{H}'+\mathcal{H}^2\right)\phi+\mathcal{H}\phi'+2\mathcal{H}\psi'+\psi''+\frac{1}{2}\nabla^2 D\right]\delta^i_j+\frac{1}{2}D^{,i}_{,j}=\frac{a^2}{2}\sum_A\left(\delta P_A\delta^i_j+\pi^i_{j\ A}\right) \tag{3.15}$$

where $D\equiv-\phi+\psi+2\mathcal{H}\left(B+E'\right)+\left(B+E'\right)'$, $\mathcal{H}\equiv a'/a$ and the prime means derivative with respect to conformal time, τ.

3.5 Perturbed equations of motion for non interacting fluids

In the absence of any interaction other than gravity between the different components, they conserve separately, i.e., $T^{\mu\nu}_{A\ ;\nu}=0$. Here we will covariantly derive the perturbed energy momentum tensor (3.7) using the perturbed Christoffel symbols listed in table A.5. Proceeding as in the background case, we obtain for the 0 and i components

$$\delta\rho'_A+3\mathcal{H}(\delta\rho_A+\delta P_A)-3(\rho_A+P_A)\psi'-k^2(\rho_A+P_A)(v_A+E')=0\ , \tag{3.16}$$

$$[(\rho_A+P_A)(v_A-B)]'+4\mathcal{H}(\rho_A+P_A)(v_A-B)+(\rho_A+P_A)\phi+\delta P_A-\frac{2}{3}\frac{k^2}{a^2}\pi_A=0\ , \tag{3.17}$$

respectively, where we have used the Fourier transform for space derivatives: $v_{,i}=-ik_iv$.

3.6 Perturbed equations of motion for interacting fluids

When the fluid components interact with one another, usually dark matter and dark energy, the stress-energy tensor of each component does not conserve in general, $T^{\mu\nu}_{A\ ;\nu}=Q^\mu_A$, but the total stress-energy tensor does, $\sum Q^\mu_A=0$. Relative to the average four velocity u^μ, the covariant stress-energy transfer of a fluid A splits as [50, 55]

$$Q^\mu_A=Q_Au^\mu+F^\mu_{\ A}\ ,\qquad Q_A=\bar{Q}_A+\delta Q_A\ ,\qquad u^\mu_AF_\mu{}^A=0\ , \tag{3.18}$$

where Q_A is the energy density transfer, and $F^\mu_{\ A}$ is the momentum density transfer rate relative to u^μ. Thus, one can introduce a momentum transfer

potential, f^A, as $F^{\mu}{}_A = a^{-1}\left[0, f_A{}^{,i}\right]$. It follows

$$Q^A{}_{\mu} = a\left[-Q_A(1+\phi) - \delta Q_A, (f_A + Q_A(v-B))_{,i}\right] \ , \tag{3.19}$$

where v is a velocity set once the interaction is defined. Using eq.(2.27) for the perturbed stress-energy tensor in a general gauge, the evolution equations for the density and velocity perturbations are

$$\begin{aligned} \delta\rho'_A + 3\mathcal{H}(\delta\rho_A + \delta P_A) &= 3(\rho_A + P_A)\psi' - k^2(\rho_A + P_A)(v_A + E') \\ &= aQ_A\phi + a\delta Q \ , \end{aligned} \tag{3.20}$$

$$\begin{aligned} [(\rho_A + P_A)(v_A - B)]' &+ 4\mathcal{H}(\rho_A + P_A)(v_A - B) + (\rho_A + P_A)\phi + \delta P_A - \frac{2}{3}\frac{k^2}{a^2}\pi_A \\ &= aQ_A(v - B) + af_A \ . \end{aligned} \tag{3.21}$$

One can notice that the interaction introduces a new function at the perturbation level, f_A. If we wish to fix it without adding an extra degree of freedom, we have two main options: (i) consider that the momentum transfer between fluids is in the direction of the velocity of the dark matter particles $Q^{\mu}_A \propto u^{\mu}_C$ [56]; and (ii) if dark energy is just vacuum, one can consider that the total pressure perturbations are adiabatic $\frac{\delta P_{Total}}{\delta\rho_{Total}} = \frac{\dot{P}_{Total}}{\dot{\rho}_{Total}}$ [57] and the perturbations behave as if the whole dark sector was unified in a single component.

3.6.1 Geodesic case

If the interaction is in the direction of the the cold dark matter particles flow, from eqs. (3.18) and (3.19), there is no momentum transfer, and cold dark matter particles will follow geodesics. In this case the interaction is defined by

$$Q^C{}_{\mu} = -Q^X{}_{\mu} = a\left[-Q_A(1+\phi) - \delta Q_A, Q_A(v_c - B)_{,i}\right] \ , \tag{3.22}$$

$$f_C = -f_X = 0 \ . \tag{3.23}$$

Bearing in mind that $P_C = 0$ and $\pi_A = 0$ (since CDM behaves as a perfect fluid without anisotropic stress), we can set the CDM density and momentum (non) conservation equation as

$$\delta\rho'_C + 3\mathcal{H}\delta\rho_C - 3\rho_C\psi' - k^2\rho_C(v_C + E') = aQ_C\phi + a\delta Q \ , \tag{3.24}$$

$$[\rho_C(v_C - B)]' + 4\mathcal{H}\rho_C(v_C - B) + \rho_C\phi = aQ_C(v_C - B) \ . \tag{3.25}$$

The corresponding equations for the dark energy component are

$$\begin{aligned}
\delta\rho_X' + 3\mathcal{H}(\delta\rho_X + \delta P_X) &- 3(\rho_X + P_X)\psi' - k^2(\rho_X + P_X)(v_X + E') \\
&= aQ_X\phi + a\delta Q \ , \qquad (3.26) \\
[(\rho_A + P_X)(v_X - B)]' &+ 4\mathcal{H}(\rho_X + P_X)(v_X - B) + (\rho_X + P_X)\phi + \delta P_X \ , \\
&= aQ_X(v_C - B) \ . \qquad (3.27)
\end{aligned}$$

If the interaction is in the direction of the dark energy flow, the equations will be the same as (3.24) - (3.27) but with v_X replacing v_C in the last term of eqs. (3.25) and (3.27).

3.6.2 Barotropic case

In this instance the dark energy is simply the vacuumm energy, so the background equation (2.22) for CDM and vacuum boils down to

$$\begin{aligned}
\dot\rho_{CDM} + 3H\rho_{CDM} &= Q_{CDM} \ , \qquad (3.28) \\
\dot\rho_V &= Q_V \ . \qquad (3.29)
\end{aligned}$$

Here it is assumed that the interaction is a total derivative of the vacuum energy density, $Q_\mu^C = -Q_\mu^V[-\dot\rho_V, -\partial_i\rho_V]$ and also that that ρ_C is a function of ρ_V. Further, since it should be a monotonically decreasing function of time, it must be invertible whereby we can express $\rho_V\,(\rho_C)$. By imposing the global adiabaticity condition

$$\frac{\delta P_C + \delta P_V}{\delta\rho_C + \delta\rho_V} = \frac{\dot P_C + \dot P_V}{\dot\rho_C - \dot\rho_V} \ , \qquad (3.30)$$

we obtain

$$\delta\rho_V = \frac{\dot\rho_V}{\dot\rho_C}\delta\rho_C \ . \qquad (3.31)$$

Consequently, the velocity and density perturbation conservation equations for CDM are

$$\begin{aligned}
\delta\rho_C' + 3\mathcal{H}\delta\rho_C - 3\rho_C\psi' - k^2\rho_C(v_C + E') &= -\delta'\rho_V \ , \qquad (3.32) \\
[\rho_C(v_C - B)]' + 4\mathcal{H}\rho_C(v_C - B) + \rho_C\phi &= k^2\delta\rho_V \ , \qquad (3.33)
\end{aligned}$$

respectively, and the ones for dark energy are just constraint equations.

3.7 Sound speed and pressure perturbations

In purely adiabatic fluids the effective sound speed in the reference rest frame of the fluid,

$$c^2_{s\,A} \equiv \left.\frac{\delta P}{\delta \rho}\right|_{rf} , \tag{3.34}$$

coincides with its adiabatic speed of sound,

$$c^2_{a\,A} \equiv \frac{P'}{\rho'} = w_A + \frac{w'_A \rho_A}{\rho'_A} . \tag{3.35}$$

However, dissipative processes generate entropy perturbations and the speed of sound is no longer defined solely by background quantities. Under a gauge transformation $x^\mu \to x^\mu + [d\tau_A, \delta x_{A\,,i}]$ from the rest gauge to a general one [50, 56] we have that

$$v_A + B = (v_A + B)|_{rf} + d\tau_A\,, \qquad \delta P_A = \delta P_A|_{rf} - P'_A d\tau_A$$

and

$$\delta \rho_A = \delta \rho_A|_{rf} - \rho'_A d\tau_A\,. \tag{3.36}$$

The A rest frame is comoving ($v_A|_{rf} = 0$) and orthogonal to the time slicing ($B|_{rf} = 0$), thus $v_A + B = d\tau_A$. Using this together with eq.(3.35) and the transformations (3.36), one finds

$$\delta P = c^2_{a\,A}\delta\rho_A + (c^2_{s\,A} - c^2_{a\,A})\left[\delta\rho_A + \rho'_A(v_A + B)\right] . \tag{3.37}$$

3.8 Gauge invariance

In the active approach to the gauge transformations in cosmology, one considers two manifolds: the physical manifold, $\mathcal{M}$, and the background space time manifold, $\bar{\mathcal{M}}$, on which coordinates are stiff. A coordinate systems in $\mathcal{M}$ is related to one in $\bar{\mathcal{M}}$ through a diffeomorphism $\mathcal{D} : \bar{\mathcal{M}} \to \mathcal{M}$. The perturbations in a point p of a function $\mathcal{Q}$ in $\mathcal{M}$ is defined as

$$\delta\mathcal{Q}(p) = \mathcal{Q}(p) - \bar{\mathcal{Q}}(\mathcal{D}^{-1}(p)) . \tag{3.38}$$

Though general relativity should be invariant under coordinates change, the relation between background and physical functions will depend on the selected diffeomorphism. In an equivalent approach, dubbed passive, one considers a physical space-time manifold $\mathcal{M}$ with some coordinate system x^μ on it. To define background magnitudes, a background function $\bar{\mathcal{Q}}(x^\mu)$

is assigned to every function $\mathcal{Q}$ on $\mathcal{M}$. Then the perturbations $\delta\mathcal{Q}$ of the magnitude $\mathcal{Q}$ is defined in a point p as

$$\delta\mathcal{Q}(p) = \mathcal{Q}(p) - \bar{\mathcal{Q}}(p) \;, \tag{3.39}$$

they, therefore, depend on the coordinate system x^μ chosen. A detailed explanation of gauge transformations can be found in [51]. Following the latter approach, we consider an infinitesimal coordinate transformation

$$\tilde{x^\mu} = x^\mu + \epsilon^\mu \;, \tag{3.40}$$

that allows us to define the function $\mathcal{Q}$ in the new coordinate system

$$\delta\mathcal{Q}(\tilde{x^\mu}) = \delta\mathcal{Q}(x^\mu) + \mathcal{L}_\epsilon\bar{\mathcal{Q}} \;, \tag{3.41}$$

$\mathcal{L}_\epsilon$ being the Lie derivative along the trajectory of ϵ. Notice that not every diffeomorphism (3.40) preserves the scalar nature of metric perturbations. The ones that do fulfill it are given by

$$\tilde{x^0} = x^0 + \epsilon^0 \qquad \text{and} \qquad \tilde{x^i} = x^i + \gamma^{ij}\epsilon_{,j} \;, \tag{3.42}$$

where the 3-vector part ϵ^i of the vector $\epsilon^\mu = [\epsilon^0, \epsilon^i]$ can be written as $\epsilon^i = \epsilon^i + \gamma^{ij}\epsilon_{,j}$, a sum of a scalar and a vector perturbation. The change in the scalar metric perturbations induced by the gauge transformation (3.42) is

$$\begin{aligned} \tilde{g}_{\mu\nu}(x) &\approx \frac{\partial x^\mu}{\partial\tilde{x}^\alpha}\frac{\partial x^\nu}{\partial\tilde{x}^\beta}g_{\mu\nu}(x-\epsilon) \\ &\approx g_{\mu\nu}(x) - g_{\mu\nu,\alpha}\epsilon^\alpha - g_{\alpha\nu}\epsilon^\alpha_{,\mu} - g_{\mu\alpha}\epsilon^\alpha_{,\nu} \\ &= g_{\mu\nu}(x) + \mathcal{L}_{-\epsilon}g_{\mu\nu} \;. \end{aligned} \tag{3.43}$$

Thus, the transformation equations read

$$\tilde{\phi} = \phi - \mathcal{H}\epsilon^0 - \epsilon^{0\prime} \;, \tag{3.44}$$

$$\tilde{\psi} = \psi + \mathcal{H}\epsilon^0 \;, \tag{3.45}$$

$$\tilde{B} = B - \epsilon^0 + \epsilon' \;, \tag{3.46}$$

$$\tilde{E} = E - \epsilon \;. \tag{3.47}$$

One can introduce linear combinations of the scalar metric functions to construct gauge-invariant variables. The most frequently used, first proposed by Bardeen [58], are

$$\Phi \equiv \phi - \mathcal{H}(B + E') - (B + E')' \;, \tag{3.48}$$

$$\Psi \equiv -\psi - \mathcal{H}\left(B + E'\right) \;. \tag{3.49}$$

Another widely used one is the curvature perturbation. This is related to the Bardeen variables in spatially flat cosmologies by

$$\zeta \equiv \Psi + \frac{\mathcal{H}}{\mathcal{H}^2 - \mathcal{H}'} \left(\Psi' - \mathcal{H}\Phi\right) \ . \tag{3.50}$$

In general, a scalar function $f(x^\mu)$, splits in its background and perturbation parts,

$$f(x^\mu) = f(\bar{x}^0) + \delta f(x^\mu) \ . \tag{3.51}$$

Frequently $\delta f(x^\mu)$ will not be a gauge-invariant variable (unless $\delta f(x^\mu)$ is a constant); it will be modified under a gauge transformation (3.42) as

$$\tilde{\delta f}(x^0, \mathbf{x}) = \delta f(x^0 - \epsilon^0, \mathbf{x} - \epsilon) \approx \delta f(x^\mu) - \bar{f}'(x^0)\epsilon^0 \ . \tag{3.52}$$

However, one is free to construct a gauge-invariant variable adding a linear combination of the metric perturbations like

$$\tilde{\delta f}_{gi} = \delta f + \bar{f}'(B - E') \ . \tag{3.53}$$

So, there are two gauge degrees of freedom left (ϵ^0 and ϵ) that should be fixed. Depending on how one set them (i.e., in the gauge we choose), the coordinate system in which perturbations are considered will be fixed. The most widely used gauges in cosmology are the synchronous gauge and the longitudinal (or conformal Newtonian) gauge, described in the next sections. To do so, the Fourier transform will be used to move to the k-space, and the divergence of the velocity, $\theta \equiv v^i_{,i} = -k^2(v + B)$, will be used.

3.9 Synchronous gauge

In this gauge one has $\phi = B = 0$. Under these conditions, the proper time lapse between two hypersurfaces coincides with the coordinate time between those hypersurfaces ($\psi = 0$). Here, the metric is defined by

$$ds^2 = a^2(\tau) \left\{-(1 + 2\phi)d\tau^2 + \left[(1 - 2\psi)\delta_{ij} + 2h_{ij}\right] dx^i dx^j\right\} \ , \tag{3.54}$$

where the metric perturbations $h_{ij}(\tau, \mathbf{x})$ are described in the Fourier space by two potential functions, $h(\tau, \mathbf{k})$ (the trace part) and $\eta(\tau, \mathbf{k})$ (the traceless part) through the integral

$$h_{ij}(\tau, \mathbf{x}) = \int d^3k e^{i\mathbf{kx}} \left[h(\tau, \mathbf{k})\hat{k}_i\hat{k}_j + 6\left(\hat{k}_i\hat{k}_j - \frac{1}{3}\delta_{ij}\right)\eta(\tau, \mathbf{k})\right] \ , \tag{3.55}$$

with $\mathbf{k} = k\hat{k}$. This gauge has the drawback of having some gauge degrees of freedom remaining because some integration constants are not fixed in the coordinates [50, 51, 52]. These can lead to unphysical gauge modes. In this gauge the perturbed Einstein field equations (3.13), (3.14) and (3.15) read

$$k^2\eta - \frac{1}{2}\mathcal{H}\dot{h} = -4\pi G a^2 \sum_A \delta\rho_A(syn) \ , \tag{3.56}$$

$$k^2\dot{\eta} = 4\pi G a^2 \sum_A \left(\bar{\rho}_A + \bar{P}_A\right)\theta_A(syn) \ , \tag{3.57}$$

$$\ddot{h} + 2\mathcal{H}\dot{h} - 2k^2\eta = -8\pi G a^2 \delta T^i_{A\ i}(syn) \ , \tag{3.58}$$

$$\ddot{h} + 6\ddot{\eta} + 2\mathcal{H}\left(\dot{h} + 6\dot{\eta}\right) - 2k^2\eta = -16\pi G a^2 \bar{P}_A \pi_A(syn) \ . \tag{3.59}$$

The general equations of motion for an interacting fluid, A, in the synchronous gauge can be obtained from the general ones (3.20) and (3.21) by the identifications $\frac{h}{2} = \frac{h^i_j}{2} = -\psi\delta^i_j + E^{,i}_{,j}$. Then, one gets

$$\begin{aligned}
\delta'_A &+ 3\mathcal{H}(c^2_{s\,A} - w_A)\delta_A + (1+w_A)\left(\theta_A + \frac{h'}{2}\right) + 3\mathcal{H}\left[3\mathcal{H}(1+w_A)(c^2_{s\,A} - w_A) + w'_A\right] \\
&= \frac{a}{\rho_A}\left\{Q_A\left[-\delta_A + 3\mathcal{H}\left(c^2_{s\,A} - w_A\right)\frac{\theta_A}{k^2}\right] + \delta Q\right\} \ , \qquad (3.60) \\
\theta'_A &+ \mathcal{H}(1 - 3c^2_{s\,A})\theta_A - \frac{c^2_{s\,A}}{(1+w_A)}k^2\delta_A + \frac{2}{3a^2(1+w_A)\rho_A}k^4\pi_A \\
&= \frac{a}{(1+w_A)\rho_A}\left\{Q_A\left[\theta - (1+c^2_{s\,A})\theta_A\right] + k^2 f_A\right\} \ . \qquad (3.61)
\end{aligned}$$

By setting $Q_A = f_A = 0$, last equations reduce themselves to the corresponding expression for a non interacting fluid.

3.10 Longitudinal gauge

The longitudinal (or conformal Newtonian) gauge is characterized by $E' = B = 0$, and the constant time hypersurfaces and the constant space lines are orthogonal to each other. Also the spatial part of the metric perturbations is isotropic,

$$ds^2 = a^2(\eta)\left\{-(1+2\phi)d\eta^2 + (1-2\psi)\delta_{ij}dx^i dx^j\right\} \ . \tag{3.62}$$

In this gauge, as one can check, the Bardeen gauge invariant variables of eqs. (3.48) and (3.49) are equal to the potentials, $\phi = \Phi$ and $\psi = -\Psi$. Likewise,

the Einstein field equations take the form

$$k^2\psi + 3\mathcal{H}\left(\mathcal{H}\phi + \dot{\psi}\right) = -4\pi G a^2 \sum_A \delta\rho_A(long)\ , \tag{3.63}$$

$$\left(\mathcal{H}\phi + \dot{\psi}\right) = 4\pi G a^2 \sum_A \left(\bar{\rho}_A + \bar{P}_A\right)\theta_A(long)\ , \tag{3.64}$$

$$\ddot{\psi} + \mathcal{H}\left(\dot{\phi} + 2\dot{\phi}\right) + \left(2\mathcal{H}' + \mathcal{H}^2\right)\phi + \frac{k^2}{3}\left(\psi - \phi\right) = -\frac{4\pi}{3} G a^2 \delta T^i_{A\ i}(long)\ , \tag{3.65}$$

$$k^2\left(\psi - \phi\right) = -16\pi G a^2 \bar{P}_A \pi_A(long)\ . \tag{3.66}$$

And the (non) conservation equations become

$$\begin{aligned} \delta'_A &+ 3\mathcal{H}(c^2_{s\,A} - w_A)\delta_A + (1+w_A)\left(\theta_A - 3\psi'\right) + 3\mathcal{H}\left[3\mathcal{H}(1+w_A)(c^2_{s\,A} - w_A) + w'_A\right] \\ &= \frac{a}{\rho_A}\left\{Q_A\left[\phi - \delta_A + 3\mathcal{H}\left(c^2_{s\,A} - w_A\right)\right] + \delta Q\right\}\ , \end{aligned} \tag{3.67}$$

$$\begin{aligned} \theta'_A &+ \mathcal{H}(1 - 3c^2_{s\,A})\theta_A - \frac{c^2_{s\,A}}{(1+w_A)}k^2\delta_A + \frac{2}{3a^2(1+w_A)\rho_A}k^4\pi_A - k^2\phi \\ &= \frac{a}{(1+w_A)\rho_A}\left\{Q_A\left[\theta - (1+c^2_{s\,A})\theta_A\right] + k^2 f_A\right\}\ . \end{aligned} \tag{3.68}$$

The relation between the potentials of Newtonian (ϕ and ψ) and Synchronous gauge (h and η) are related by

$$\phi = \dot{\alpha} + \mathcal{H}\alpha \qquad \text{and} \qquad \psi = \eta - \mathcal{H}\alpha\ , \tag{3.69}$$

where $\alpha \equiv \frac{\dot{h}+6\dot{\eta}}{2k^2}$, and the transformations of variables from one gauge to the other are [52]

$$\delta_A(syn) = \delta_A(long) - \alpha\frac{\dot{\bar{\rho}}_A}{\bar{\rho}_A}\ , \tag{3.70}$$

$$\theta_A(syn) = \theta_A(long) - \alpha k^2\ , \tag{3.71}$$

$$\delta P_A(syn) = \delta P_A(long) - \alpha\dot{\bar{P}}_A\ , \tag{3.72}$$

$$\pi_A(syn) = \pi_A(long)\ . \tag{3.73}$$

This linear transformations permit to transform the equations from the synchronous gauge to the longitudinal gauge, and viceversa.

Chapter 4

Observational constraints

To constrain the free parameters of the cosmological models considered in this Memoir, we use observational data from SN Ia (557 data points), the CMB-shift, BAO, and gas mass fractions in galaxy clusters as inferred from X-ray data (42 data points) and the Hubble rate (15 data points) as geometrical data. Being the likelihood function defined as $\mathcal{L} \propto \exp(-\chi^2/2)$ the best fit follows from minimizing the sum $\chi^2_{\rm total} = \chi^2_{sn} + \chi^2_{cmb} + \chi^2_{bao} + \chi^2_{X-rays} + \chi^2_{Hubble}$. The data analysis realized in this memoir is briefly depicted in appendix A.3.

4.1 Super novae type Ia

The SN Ia type refers to supernovae produced in binary systems, a carbon-oxigen white dwarf and a bigger companion, such as a red giant. The collapsed object accretes gas and dust from its companion until the Chandrasekhar mass limit is reached, $M \simeq 1.4 M_{\odot}$. Beyond that point, the degenerate gas pressure can not withstand the star weight and a gravitational collapse ensues, leading to a thermonuclear explosion. Since the mass and constituents of white dwarfs when they explode are alike, these supernovae have a very similar light curve and maximum absolute magnitude. Therefore, they are considered as nearly "standard candles". However, there different shapes at different bands have been found, and for different SN Ia. Nevertheless, an empirical recipe that can convert them into "calibrated candles" has been established [59]. Thus, SN Ia are now routinely used as extragalactic distance indicators. Once the data are calibrated, we contrast

the theoretical distance modulus

$$\mu_{th}(z_i) = 5\log_{10}\left(\frac{D_L}{10\text{pc}}\right) + \mu_0\,, \tag{4.1}$$

where $\mu_0 = 42.38 - 5\log_{10} h$, of the cosmological model under study with the observed distance modulus $\mu_{obs}(z_i)$ of the 557 SN Ia compiled in the Union2 set [60]. The latter assemble is much richer than previous SN Ia compilations and has some other advantages, especially the refitting of all light curves with the SALT2 fitter and an enhanced control of systematic errors. In (4.1) $D_L = (1+z)\int_0^z \frac{dz'}{E(z';\mathbf{p})}$ denotes the Hubble-free luminosity distance defined in eq. (2.54), with $\mathbf{p}$ the model parameters (Ω_{X0}, c^2, r_f, and H_0), and $E(z;\mathbf{p}) := H(z;\mathbf{p})/H_0$. The χ^2 from the 557 SN Ia is given by

$$\chi^2_{sn}(\mathbf{p}) = \sum_{i=1}^{557} \frac{[\mu_{th}(z_i) - \mu_{obs}(z_i)]^2}{\sigma^2(z_i)}\,, \tag{4.2}$$

where σ_i denotes the 1σ uncertainty associated to the ith data point. To eliminate the effect of the nuisance parameter μ_0 we resort to the method of [61] to obtain $\tilde{\chi}^2_{sn} = \chi^{2\,(minimum)}_{sn}$.

4.2 The cosmic microwave background

In 1965 Penzias and Wilson, from the Bell laboratories, found a very homogeneous and isotropic noise when working in a ultra-sensitive cryogenic microwave antenna [62]. After contacting Dicke's group at Princeton, it was proposed that the noise corresponded to be the Cosmic Microwave Background (CMB) radiation [63] predicted nearly twenty years before by Alpher and Herman [64]. The black body temperature detected by the antenna was $T = 2.3 \pm 0.3$ Kelvin. This discovery supposed a strong support for the hot Big Bang theory, and shed light on how the Universe was at recombination, but did not tell much of its matter content, its expansion rate, nor its spatial curvature. Their anisotropies, detected much later by the COBE satellite probe, shed further light on this. Figure 4.1 depicts this anisotropies as seen by the Planck satellite.

The light of the CMB comes from the recombination epoch, around $z_\star \approx 1100$, the time when electrons combined with protons to form neutral atoms, and photons could propagate freely. Before then, photons and baryons were tightly coupled by the Compton effect. The last scattering

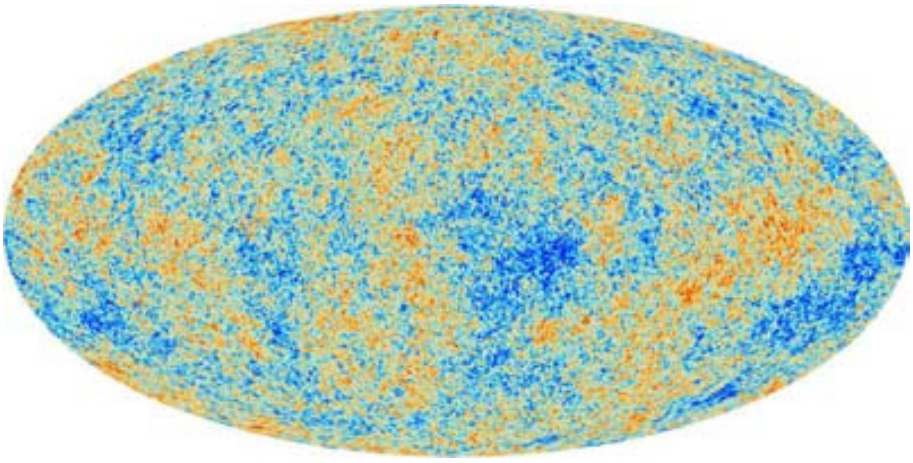

Figure 4.1: Temperature anisotropies detected by the Planck mission [7]. The blue spots are colder regions than average and the red ones hotter.

surface is the spherical surface with radius determined by the distance traveled by light from the recombination epoch until the present. The temperature anisotropies detected nowadays are of two main types: (i) primary anisotropies; those imprinted in the photons before and while leaving the last scattering surface (the physical processes that took place during recombination are quite well known); and (ii) secondary anisotropies, those imprinted on the radiation when propagating from the last scattering surface to the observer.

4.2.1 Primary anisotropies

While matter and radiation interact mainly due to Compton effect, both, behave as a single fluid. The primordial perturbations set up by inflation led to pressure gradients that propagated as sound waves. Normal mode analysis breaks the system into a set of independent oscillators, and so, each mode k of the temperature anisotropies $\Theta = \Delta T/T$ corresponds to a forced oscillator: $(1+R)\ddot{\Theta} + k^2 c_s^2 \Theta \simeq (1+R)g$, where, $R \simeq 3\rho_B/4\rho_\gamma$ is the effective mass of the oscillator and $c_s = 1/\sqrt{3(1+R)}$ the speed of sound of the coupled fluid before recombination. $g = -k^2 c_s^2 \phi/3 - \ddot{\psi}$ is the effective acceleration provided by gravity, ϕ the Newtonian potential, and $\psi \simeq -\phi$ (since neutrinos were decoupled before the recombination epoch) the spatial curvature perturbation, both introduced in §3.10. At recombination

the Universe was already matter dominated and the gravitational potentials remained nearly constant; the *acoustic oscillations* present in the baryon-photon plasma were frozen once the radiation decoupled from the baryons. The size of the sound horizon at that time is described by the wavenumber $k_A \equiv \pi/r_{s\star}$ with $r_{s\star} = \int c_{s\star} d\eta$ the horizon size at recombination. This wave number sets the fundamental scale of the acoustic oscillations. The position of the first acoustic peak in the power spectrum - Fig. 4.2 - is given by this scale, $l_A \simeq k_A d_A$, where l_A gives us the size of the horizon at recombination. Since this size depends on the geometry of space, and knowing the angular diameter distance d_A, that depends just on the model used, the said position is a probe of the spatial curvature of the Universe, $\Omega_{\kappa 0}$ -see fig. 4.3.

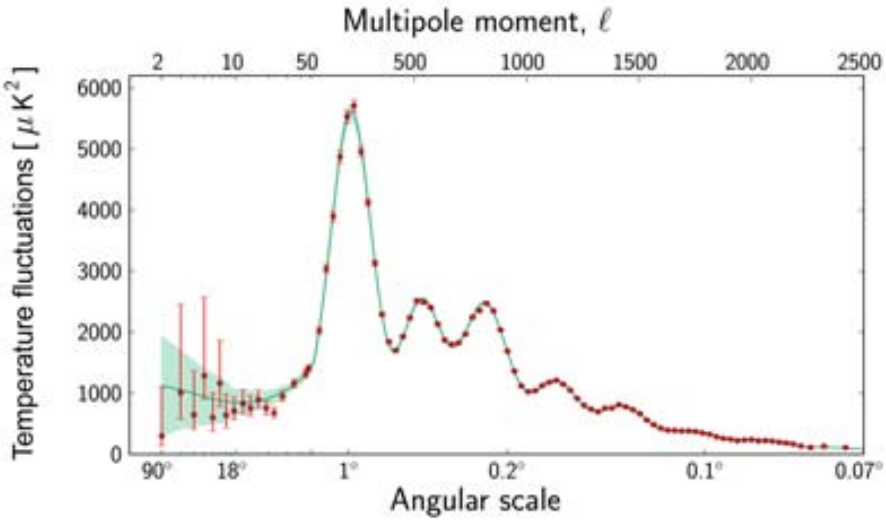

Figure 4.2: Temperature anisotropies power spectrum as a function of the angle (lower scale) and the multipole moment (upper scale) detected by the Planck mission [7]. The solid line correspond to the best fit ΛCDM model. The position of the first acoustic peak ($1^\circ - 2^\circ$) is compatible with $|\Omega_{\kappa 0}| \ll 1$.

Photons that escape from the last scattering surface suffered a gravitational redshift, that added to its intrinsic fluctuations, are known as the *Sachs-Wolfe effect* [66]. The higher density regions attract matter and radiation

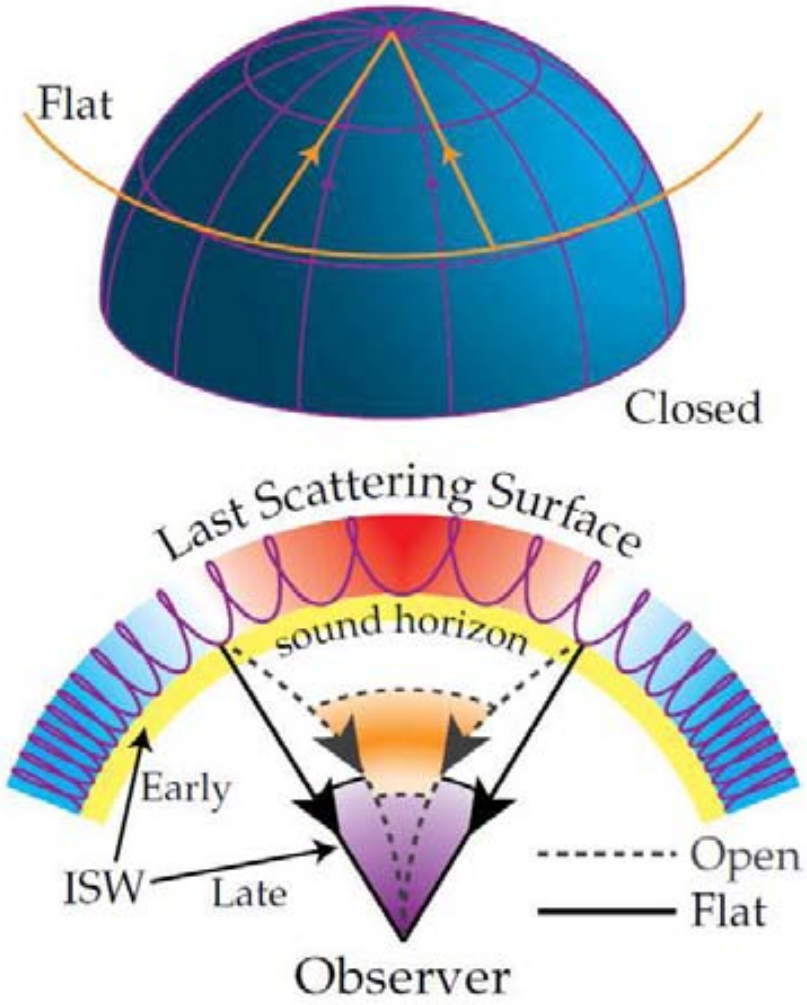

Figure 4.3: The angular size of the sound horizon at recombination depends on the geometry of the Universe and the distance to the last scattering surface. At a fixed distance, a smaller physical scale is required to subtend the same angle in a closed universe, and a larger one in an open universe. Figure borrowed from [65].

that is pushed away from the lower density regions, and due to the presence of a higher baryon density, it results harder for the photons to escape, so the

corresponding temperature is enhanced with respect to the one of that very region without baryons. In the underdense regions, the pressure is weaker, and accordingly, due to the presence of baryons it results also harder for the photons to climb the potential well, being the region less colder than it should in the absence of baryons. This effect, known as *baryon dragg*, is the cause of the alternating heights of the odd (over densities) and even peaks (under densities) seen in the temperature anisotropies power spectrum -see Fig. 4.2. This effect is crucial in determining the present baryon fraction $\Omega_{B\,0}h^2$ ($\simeq 0.022$).
Albeit recombination took place well in the matter dominated era, i.e., after the equality redshift, z_{eq}, the potentials ϕ and ψ were not exactly constant. This effect, called the *driving effect* introduces an enhancement of the peaks, and since the wavenumber k_{eq} (describing the sound horizon scale at z_{eq}) is the critical scale to change the potential behavior. The peak-to-plateau ratio is a test for $\Omega_{CDM\,0}$. Since recombination lasted a while ($\Delta z \simeq 80$), the photons mean free path increased in that period. Thus, for short wavelengths, the photons mean free paths overtook them. This mixed up the hot with the cold regions and damped the anisotropies somewhat. This effect, known as *diffusion damping* (or *Silk damping*), decreased the power of the high multipoles $l \geq 1000$ (small scales) seen in the Fig. 4.2. For details on the CMB, see Ref. [67].

Cosmic Microwave Background shift parameter, R

As we have seen, the CMB power spectrum is sensitive to the distance to the decoupling epoch via the locations of peaks. More specifically, thanks to CMB data one can measure two distance ratios. The first one, defined by the ratio between the distance to decoupling to the Hubble horizon at that time $H^{-1}(z_\star)$, is the so called CMB-shift $\mathcal{R}$ [68, 69]. It measures the displacement of the first acoustic peak of the CMB temperature spectrum with respect to the location it would have taken in the Einstein-de Sitter Universe

$$\mathcal{R} = \sqrt{\Omega_{M_0}} \int_0^{z_\star} \frac{dz}{\frac{H(z)}{H_0}} \,. \tag{4.3}$$

This parameter is approximately model-independent but not quite as the above expression somehow assumes a negligible dark energy density at decoupling, and should be suitably modified if not used in ΛCDM or wCDM models [70, 71, 72]. The 7-year WMAP data provides $\mathcal{R}(z_{rec}) = 1.725 \pm 0.018$ [70].

Acoustic scale l_A

The other ratio provided by the CMB is the acoustic scale, l_A, described by the angular distance to the decoupling surface divided by the sound horizon at that time

$$l_A = \pi \frac{d_A(z_\star)}{r_s(z_\star)} \,. \tag{4.4}$$

Both quantities, $d_A(z)$ and $r_s(z)$ are comoving. The 7-year WMAP data yields $l_A = 302.09 \pm 0.76$ [70].

4.2.2 Secondary anisotropies

Here we briefly describe gravitational effects that affect the evolution of the perturbations. In addition to that, there are other effects from reionization that we will not consider here [65, 67]. One effect, null in a matter dominated Universe, that alters the perturbations is the Integrated Sachs-Wolfe (ISW) effect. It is due to the evolution of the potentials ϕ and ψ. Just after recombination, the radiation content is not negligible though small, and so the potential evolves modifying the CMB radiation field. This is known as the *early ISW effect*. When dark energy begins dominating the Universe, the potentials start to evolve again. So when a photon coming from the last scattering surface falls into a potential well, e.g. created by a galaxy cluster, the blueshift due to the infall is overcompensated by the redshift arising when emerging from the evolving potential well. This is known as *late ISW effect*. It has been detected a signal of this kind of anisotropy by correlating WMAP data with large scale structures data [73, 74].
Other smaller perturbations affecting the CMB field are tensor perturbations due to gravitational waves. The main consequence of gravitational waves is to enhance the quadrupole ($l = 2$) [75]. Due to the high cosmic variance the imprint of gravitational waves in the CMB has not been detected as yet.
Gravitational lensing can also affect the propagation of photons when passing close to potential wells. It should smooth the peaks of the spectrum, especially on small scales [76, 77]; but, in any case, it will be just a second order effect.

4.2.3 Temperature anisotropies power spectrum

Since the dark matter models considered in this Memoir little or nothing modify the pre-recombination scenario of the standard ΛCDM model, here, we describe some aspects of the temperature anisotropies formalism very

schematically. For details see [49, 67]. In this section conformal time will be denoted by η, to distinguish it from opacity described by τ. Several non-equilibrium processes, governed by the Boltzmann-Einstein equation played a crucial role in the evolution of the Universe, such as the formation of light elements in the Big Bang nucleosynthesis, the capture of electrons by protons to form neutral hydrogen and reionization. Neglecting polarization, the said equation reads

$$\Theta' + (ik\mu - \tau')\Theta = -\Phi' - ik\mu\Psi - \tau' \left[\Theta_0 + \mu v_B - \frac{1}{2}\mathcal{P}_2(\mu)\Theta_2\right] . \qquad (4.5)$$

Here $\Theta \equiv \delta T/\bar{T}$ is the photon temperature perturbation, μ the photon propagation direction, v_B the baryons velocity, P_2 the second order Legendre polynomial described in appendix A.4, while Θ_0 and Θ_2 are, the monopole (density) and quadrupole (velocity) moment in the multipole expansion of the temperature field

$$\Theta_l \equiv \frac{1}{(-1)^l}\int_{-1}^{1}\frac{d\mu}{2}\mathcal{P}_l(\mu)\Theta(\mu) , \qquad (4.6)$$

respectively. Atrio-Barandela *et al* [78] and Hu and Sugiyama [79] gave expressions for the monopole and dipole in the tight coupled limit, that are the dominant moment at recombination. However, effects like diffusion have a non negligible quadrupole moment. These moments will be the source of the CMB temperature anisotropies at recombination, but we wish to compute them today. From the last scattering surface, photons travel in a free streaming regime. Considering that $\tau(\eta_0) = 0$ and $\tau(\eta_i) \gg 1$ for $\eta_i \ll \eta_\star$, and noticing that $[\Theta' + (ik\mu - \tau')\Theta]\, e^{ik\mu\eta - \tau} = \frac{d}{d\eta}\left(\Theta\, e^{ik\mu\eta-\tau}\right)$, one gets

$$\Theta(k,\mu,\eta_0) = \int_0^{\eta_0} d\eta \tilde{S}(k,\mu,\eta)\, e^{ik\mu(\eta-\eta_0)-\tau} , \qquad (4.7)$$

where $\tilde{S}$ is the source function equal to the right hand side of eq. (4.5). One eliminates the μ dependence of $\tilde{S}$ by the replacement $\mu \to \frac{1}{ik}\frac{d}{d\eta}$, justified because of the exponential in (4.8). Then one multiplies both sides of eq. (4.7) by $\mathcal{P}_l$ and then integrate over μ to obtain

$$\Theta_l(k,\eta_0) = \int_0^{\eta_0} d\eta S(k,\eta) j_l[k(\eta_0 - \eta)] , \qquad (4.8)$$

where j_l is the spherical Bessel function, whose properties are described in appendix A.5. The source function is now recast as

$$S(k,\eta) \equiv e^{-\tau}\left[-\Phi' - \tau'\left(\Theta_0 + \frac{1}{4}\Theta_2\right)\right] + \frac{d}{d\eta}\left[e^{-\tau}\left(\Psi - \frac{iv_B\tau'}{k}\right)\right] - \frac{3}{4k^2}\frac{d^2}{d\eta^2}\left(e^{-\tau}\tau'\Theta_2\right) . \tag{4.9}$$

If one introduces the visibility function, $g(\eta) \equiv -\tau' e^{-\tau}$, which corresponds to a probability distribution since $\int_0^{\eta_0} d\eta g(\eta) = 1$, the source term can be expressed as

$$\begin{aligned} S(k,\eta) &\simeq g(\eta)\left[\Theta_0(k,\eta) + \Psi(k,\eta)\right] + e^{-\tau}\left[\Psi_0'(k,\eta) - \Phi'(k,\eta)\right] \\ &+ \frac{d}{d\eta}\left(\frac{ig(\eta)v_B(k,\eta)}{k}\right) . \end{aligned} \tag{4.10}$$

Notice that the first term in (4.10) gives the contribution from the intrinsic perturbation from recombination and the gravitational potential (Sachs-Wolfe effect). The second term, related to the time dependence of the potentials, is the integrated Sachs-Wolfe contribution. The last one is the velocity term that describes the Doppler effect due to the relative velocities of emitter and observer. Equation (4.8), first proposed in [80], is of great importance when computing temperature anisotropies. It divides the computational effort in solving a geometrical part, j_l, independent of the cosmological evolution and a source term, S, that encodes the details of the cosmological model. This equation is the basis of the Boltzmann codes to compute CMB anisotropies, e.g., CMBfast, CAMB [81] and CLASS [82]. It reduces the number of coupled differential equations from thousands to a few dozens.

Since what we observe through telescopes from a given position, $\mathbf{x}$, are directions in the sky, μ, to compute temperature anisotropies, it is convenient to expand them in spherical harmonics

$$\Theta(\mathbf{x},\mu,\eta) = \sum_{l=1}^{\infty}\sum_{m=1}^{l} a_{lm}(\mathbf{x},\mu,\eta)Y_{lm}(\mu) , \tag{4.11}$$

the analogous to the Fourier transform in a spherical surface. Because of the spherical harmonics properties, given in appendix A.6, one can invert eq. (4.11) as

$$a_{lm}(\mathbf{x},\eta) = \frac{1}{(2\pi)^3}\int d^3k e^{i\mathbf{kx}} \int d\Omega Y_{lm}^{\star}(\mu)\Theta(\mathbf{x},\mu,\eta) , \tag{4.12}$$

The mean value of the a_{lm} is zero but the variance does not vanish in general. The latter is defined by

$$< a_{lm} a^{\star}_{l'm'} >= \delta_{ll'}\delta_{mm'} C_l \ , \tag{4.13}$$

and it is what is really computed from the CMB data. There is a fundamental uncertainty related to the C_ls that decreases with l, since there are smaller number of samples with increasing angular size (there are less a_{lm} for every C_l). It is known as cosmic variance, $\Delta Cl/C_l = \sqrt{2/(2l+1)}$ -see Fig. 4.2.

4.3 Baryon Acoustic Oscillations

Pressure waves originated from cosmological perturbations in the primeval baryon-photon plasma produced acoustic oscillations in the baryonic fluid, as has been seen in §4.2.1. These oscillations were frozen at recombination, leaving overdense shells of radius equal to the size of the horizon at the last scattering surface, around 150 Mpc today. Meanwhile, the dark mater overdensities grew in the center of the shell without oscillating, since they did not feel the radiation pressure. So, the center and the shell are correlated and a peak must be expected in the correlation function (defined in §4.4) around 150 Mpc due to the baryonic acoustic oscillations (BAO) (governed by $\Omega_M h^2$ and $\Omega_B h^2$). Once the characteristic scale of the oscillations is determined at $z_\star$ through the first peak in the CMB power spectrum, the acoustic scale can be used as a standard ruler to measure absolute distances[1]. This oscillations have been unveiled by a clear peak in the large scale correlation function measured from the luminous red galaxies sample of the Sloan Digital Sky Survey (SDSS) at $z = 0.35$ [83], as shown in Fig. 4.4, as well as in the Two Degree Field Galaxy Redshift Survey (2dFGRS) at $z = 0.2$ [84]. Further peaks have been observed more recently: at $z = 0.278$ (with the SDSS [85]), at $z = 0.106$ (in the 6dFGRS [86]), and at $z = 0.44$, $z = 0.60$, and $z = 0.73$ (by the WiggleZ team [87]). These peaks are described by a characteristic distance scale, the *dilation* scale,

$$D_v(z_{BAO}) = \left[\frac{z_{BAO}\, d_A(z_{BAO})^2}{H(z_{BAO})} \right]^{\frac{1}{3}} \ . \tag{4.14}$$

[1]This absolute distance is not model independent since we ought to fix the expansion history, from $z_\star$ until today, using some model.

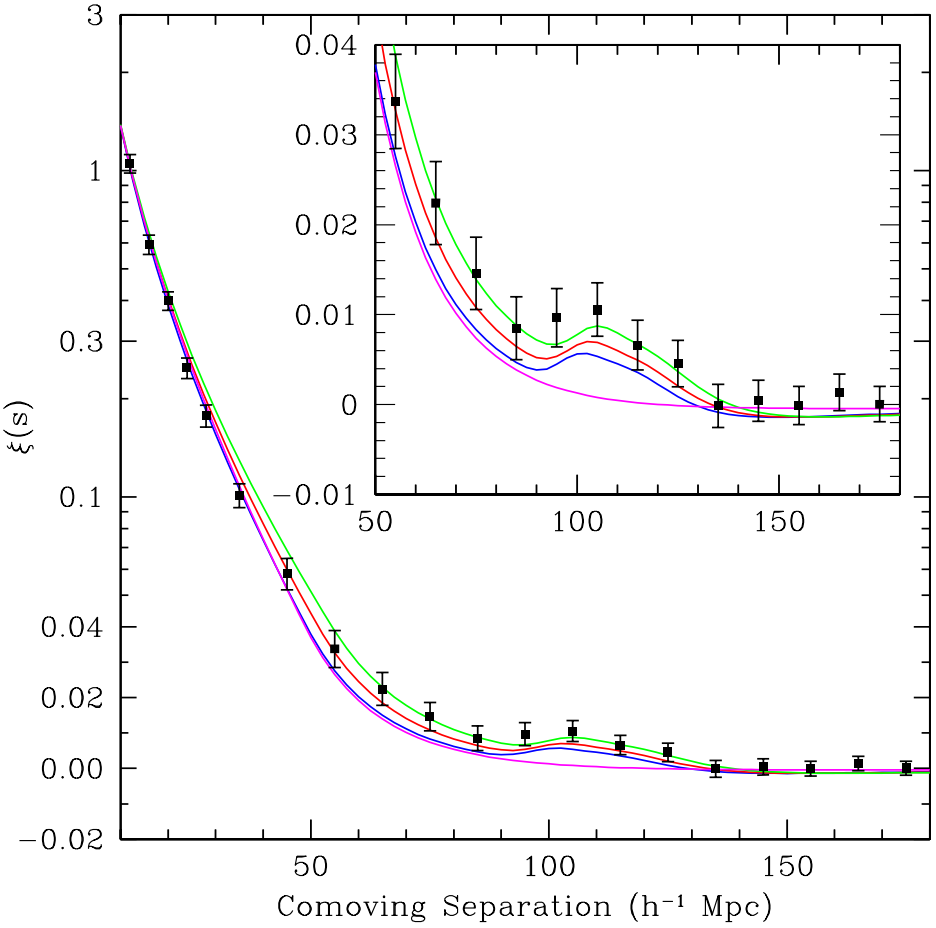

Figure 4.4: Large-scale redshift-space correlation function of the SDSS luminous red galaxies. The BAO peak can be seen around $100h^{-1}$ Mpc. The plot is borrowed from [83].

(see Ref. [88] for a pedagogical derivation of this expression). Data from SDSS and 2dFGRS observations provided a more model independent quantity, $D_v(0.35)/D_v(0.2) = 1.736 \pm 0.065$ [84].

4.4 Matter power spectrum

The autocorrelation function

$$\epsilon(\mathbf{r}) \equiv < \delta(\mathbf{x})\delta(\mathbf{x}+\mathbf{r}) > \tag{4.15}$$

describes the probability of finding, e.g., a galaxy at $\mathbf{x}+\mathbf{r}$ if there is one at $\mathbf{x}$. If $\epsilon(\mathbf{r})$ is zero, the galaxy distribution is said to be uncorrelated. Rather than working in real space, it is more convenient to shift to Fourier space. The density perturbation in k-space, δ_k, is defined by

$$\delta_k(x) = \frac{1}{(2\pi)^{\frac{3}{2}}} \int d^3k e^{i\mathbf{kx}} \tag{4.16}$$

By computing the mean of two k-modes of the density perturbations, we obtain

$$\begin{aligned} < \delta_k^* \delta_{k'} > &= \frac{1}{(2\pi)^3} \int d^3x\, d^3x'\, e^{i\mathbf{k'(x'-x)}}\, e^{-(\mathbf{k-k'})\mathbf{x}} \\ &= \delta^D(k-k')P(k) \end{aligned} \tag{4.17}$$

where δ^D is the delta of Dirac. From equations (4.15), (4.16) and (4.17), it is seen that the Fourier transform of the density perturbation autocorrelation function is the matter power spectrum $P(k)$. There are two characteristic times when studying the evolution of the perturbations, the matter radiation equality, t_{eq} and the time, t_{enter}, when a perturbations becomes smaller than the horizon, η, introduced in eq. (2.52). At the latter, causality begins to apply to the perturbation. Using eq. (2.52), we get

$$\eta \propto \begin{cases} a^{\frac{1}{2}} & \text{radiation dominated} \\ a & \text{matter dominated .} \end{cases} \tag{4.18}$$

It is generally assumed that the perturbations at $t = t_{enter}$, follow the power law

$$P(\mathbf{k}, t_{enter}) = Ak^n \ , \tag{4.19}$$

with n a free parameter that characterizes the scale dependence. Recently, the Planck collaboration found $n = 0.9616 \pm 0.0094$ [7]. In the linear regime, spatial and time dependence can be separated: $\delta_{\mathbf{k}}(t) = \delta_{\mathbf{k}}(t_0)D_+(t)/D_+(t_0)$, where $D_+(t)$ denotes the growing solution. At the radiation dominated epoch, the dark matter density perturbations remain nearly constant once inside the horizon (the Mészáros effect [89]). On the other hand, at the

matter dominated epoch (potentials nearly constant), in the subhorizon limit ($k \gg a/H$), one has $D_+ \propto a$, as follows from eq. (3.13). Thus, the CDM matter power spectrum of density perturbations measured today can be expressed as

$$\delta_{\mathbf{k}}(t_0) = \frac{D_+(t_0)}{D_+(t_{enter})}\delta_{\mathbf{k}}(t_{enter}) \propto \frac{1}{D_+(t_{enter})}\delta_{\mathbf{k}}(t_{enter})k^n \ . \tag{4.20}$$

Therefore,

$$P(\mathbf{k}, t_{enter}) \propto \left(\frac{1}{D_+(t_{enter})}\right)^2 k^n \ . \tag{4.21}$$

Bearing in mind the behavior of perturbations during the radiation and matter dominated epochs, and using eq. (4.18), we get

$$P(\mathbf{k}, t_0) \propto \begin{cases} k^{n-4} & \text{(if } k \text{ enters in the radiation dominated epoch)} \\ k^n & \text{(if } k \text{ enters in the matter dominated epoch)} \end{cases} \tag{4.22}$$

For $n = 1$, the matter power spectrum at horizon crossing is scale independent (a Harrison-Zel'dovich spectrum [90, 91]). Figure 4.5 depicts the matter power spectrum for the concordance ΛCDM model. However, in this case, the effects due to the presence of baryons and the cosmological constant appear while in this Section have been omitted.

4.5 Gas mass fraction

Since the bulk of baryons in galaxy clusters are in the form of hot X-ray emitting gas clouds (other baryon sources lagging far behind in mass) the fraction of baryons in clusters, $f_{gas} := M_{gas}/M_{tot}$, at present is of great interest since it is an indicator of the overall cosmological ratio Ω_B/Ω_M and, up to a fair extent, it is independent of redshift [93] -see §4.5. This quantity can be determined from the X-ray flux originated in hot clouds of baryons and it is related to the cosmological parameters by $f_{gas} \propto (1+z)^2\, d_A^{3/2}$, where $d_A := (1+z)^{-1}\int_0^z \frac{dz'}{H(z')}$ denotes the angular diameter distance to the cluster. Data were obtained by the Chandra satellite from 42 dynamically relaxed galaxy clusters in the redshift interval $0.05 < z < 1.1$ [94]. In model fitting, the empirical formula

$$f_{gas}(z) = \frac{K\, A\, \gamma\, b(z)}{1 + s(z)}\frac{\Omega_{b0}}{\Omega_{M0}}\left(\frac{d_A^{\Lambda CDM}}{d_A}\right)^{3/2} \tag{4.23}$$

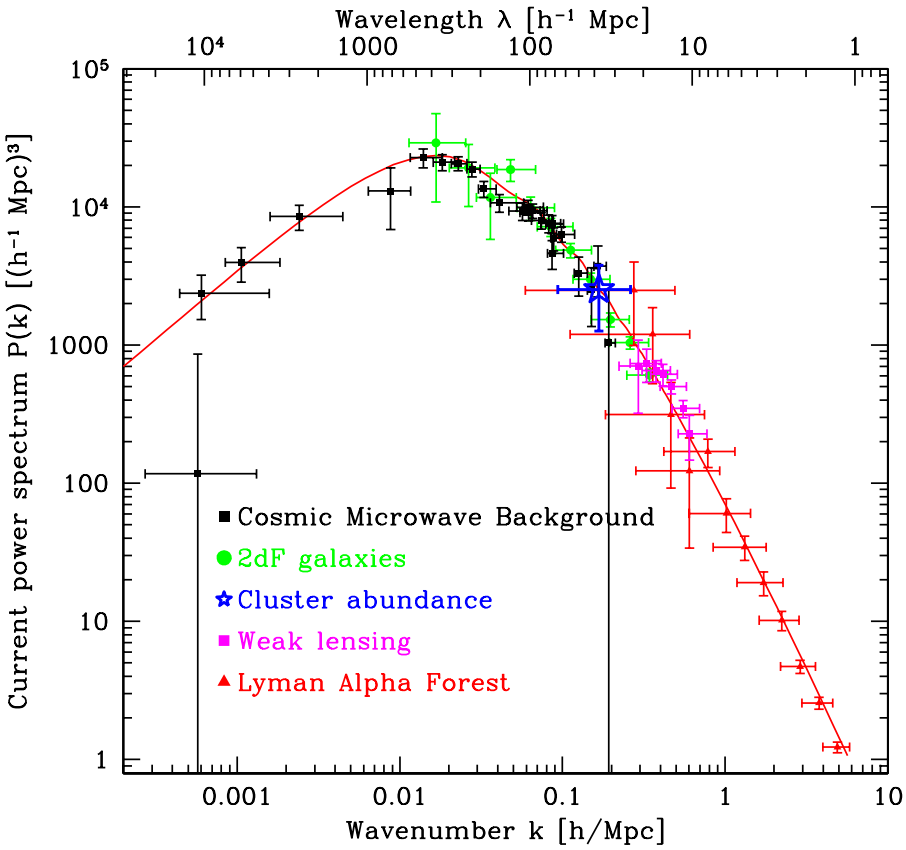

Figure 4.5: Matter power spectrum for the ΛCDM model. The scale of the observed peak is k_{eq}. It is smooth because the transition from radiation to matter domination was gently. Figure borrowed from [92].

(Eq. (3) in Ref. [94]), is conventionally used, in which the ΛCDM model is utilized as reference. Here, the parameters K, A, γ, $b(z)$ and $s(z)$ model the abundance of gas in the clusters.

4.6 History of the Hubble parameter

Recently, high precision measurements by Riess and collaborators at $z = 0$, from the observation of 240 Cepheid variables of rather similar periods and metallicities [95], as well as measurements by Gaztañaga *et al.*, at $z = 0.24,\ 0.34, \text{and}\, 0.43$ [96], who used the BAO peak position as a standard ruler in the radial direction, have somewhat improved our knowledge of $H(z)$. However, at redshifts above, say, 0.5 this function remains largely unrestricted. Yet, in order to constrain the models we employ these four data alongside 11 noisier data in the redshift interval $0.1 \lesssim z \lesssim 1.8$, from Simon *et al.* [97] and Stern *et al.* [98], obtained from the differential ages of passive-evolving galaxies and archival data.

Chapter 5

Interacting dark energy model at the Hubble length[1]

5.1 Basics of the model

The spatially flat FLRW holographic model proposed in [100] rests on two main assumptions: (*i*) The dark energy density is governed by the saturated holographic relationship, Eq. (2.45), with the infrared cutoff fixed by the Hubble radius, i.e., $L = H^{-1}$. (*ii*) Dark matter and dark energy do not evolve independently of each other. They interact according to

$$\dot{\rho}_M + 3H\rho_M = Q \ , \quad \text{and} \quad \dot{\rho}_X + 3H(1+w)\rho_X = -Q \, , \tag{5.1}$$

where w stands for the equation of state parameter of dark energy, and

$$Q = \Gamma \, \rho_X \tag{5.2}$$

is the interaction term where Γ denotes the rate by which ρ_X changes as a result of the interaction. We assume Γ to be semipositive-definite. Note that if Q were negative, the transfer of energy would go from dark matter to dark energy, in contradiction with the second law of thermodynamics [100]. Further, use of the Layzer-Irvine equation on nearly one hundred galaxy clusters strongly supports this view [101].

Interacting models were first proposed by Wetterich to lower down the value of the cosmological term [102]. Later on it was proved efficient at easing the cosmic coincidence problem [103, 104] and it was suggested that the interaction (whatever form it might take) is not only likely but inevitable

[1] This Chapter corresponds to the model of Ref. [99].

[105]. The amount of literature on the subject is comparatively ample - see, e.g., [106] and references therein. Admittedly, the expression (5.2) is nothing but a useful parametrization of the interaction. Given our poor understanding of the nature of dark matter and dark energy, there is no clear guidance to derive an expression for Q from first principles. This is why our approach is just phenomenological.

The model is fully specified by three quantities, e.g., the current value of the Hubble rate, H_0, the dimensionless density parameter Ω_X (or, equivalently, Ω_M), and Γ. Note that c^2 is fixed by $c^2 = \Omega_X$, as it can be readily checked.

The first assumption readily implies that Ω_X does not vary with expansion, and that the ratio of energy densities, $r \equiv \rho_M/\rho_X$, stays fixed in spatially flat FRW universes ($\Omega_M + \Omega_X = 1$) for any interaction. The latter consequence greatly alleviates the coincidence problem albeit, strictly speaking, it does not solve it in full because the model cannot predict that $r \sim \mathcal{O}(1)$ (to the best of our knowledge, no model is able to predict it). This feature of Ω_X and r being strictly constants may seem too strong; however, one should bear in mind that both quantities would slightly vary with the Universe expansion if the parameter c^2 in Eq. (2.45) were allow to weakly depend on time, something not at all unreasonable [33]. Further, r would not be constant if the restriction to spatial flatness were relaxed. At any rate, we shall take the simpler stance that both c^2 and r do not vary; thus, the number of free parameters of the model will be kept to a minimum.

At first sight, the consequence of Ω_X being of order unity also at early times might look worrisome. One may think that a large dark energy component at that period would prevent the formation of gravitationally bound objects. However, this is not the case as

$$w = -\frac{1+r}{r}\,\frac{\Gamma}{3H} \tag{5.3}$$

is not constant, and for suitable choice of the ratio Γ/H it tends to the equation of state of non-relativistic matter at early times. Its evolution is governed by the Hubble rate which, in the simplest case of Γ being a constant, takes the form

$$H = H_0\left[\frac{\Gamma}{3H_0 r} + \left(1 - \frac{\Gamma}{3H_0 r}\right) a^{-3/2}\right], \tag{5.4}$$

which corresponds to a specific generalized Chaplygin gas [43]. Figures 5.1 and 5.2 show the history of the equation of state for the best fit values of the model up to redshifts 8 and 1.2, respectively. Figure 5.1 illustrates that

at high redshifts w approaches zero asymptotically. Figure 5.2 shows that, in accordance with the analysis in [107], $w(z)$ varies little at small redshifts.

The deceleration parameter, q, defined in eq. (2.19), whose evolution is

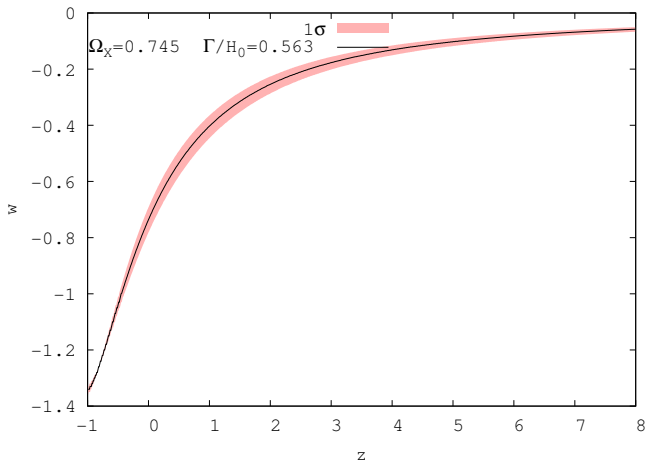

Figure 5.1: Evolution of the equation of state parameter of dark energy, Eq. (5.3), for the best fit model, up to $z = 8$. In this, as well as in subsequent figures, the red swath indicates the region obtained by including the 1σ uncertainties of the constrained parameters used in the calculation (in the present case, Ω_X and Γ/H_0).

illustrated in Fig. 5.3, obeys

$$q = \frac{1}{2}\left(1 - \frac{\Gamma}{Hr}\right) . \tag{5.5}$$

This expression implies that $q \to \frac{1}{2}$ at high redshifts as it should, and that the transition from deceleration to acceleration occurs at

$$z_{tr} = \left(\frac{2\Gamma}{3H_0\, r - \Gamma}\right)^{2/3} - 1\,, \tag{5.6}$$

which yields $z_{tr} \simeq 0.80$ for the best fit values. It should be noted that in [32] the transition deceleration-acceleration required that the c^2 varied, if only very slowly. In the present case, the transition also occurs for $c^2 =$ constant (as, for simplicity, we are considering). The difference stems from the fact that in [32] the ratio Γ/H was kept constant, while the present model has $\Gamma =$ constant, instead.

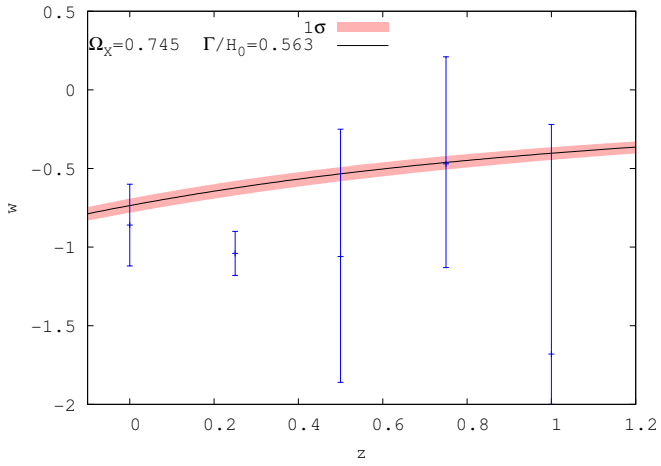

Figure 5.2: Evolution of the equation of state of dark energy for the best fit model up to $z = 1.2$. The observational data with their 2σ error bars are borrowed from [107]. In plotting the curve no fit to these data was made.

The age of old luminous objects at high redshifts can constrain cosmological models by simply requiring that their age at the redshift they are observed do not exceed the age of the Universe at that redshift. Figure 5.4 depicts the dependence of the age of the Universe on redshift for the best fit values of both the holographic model and the ΛCDM model alongside the age and redshift of three luminous old objects, namely: galaxies LBDS 53W069 ($z = 1.43$, $t = 4.0$ Gyr) [109] and LBDS 53W091 ($z = 1.55$, $t = 3.5$ Gyr) [110, 111], as well as the quasar APM 08279+5255 ($z = 3.91$, $t = 2.1$ Gyr) [112, 113]. While the ages of the two first objects are lower than the ages of the holographic model and the ΛCDM model at the corresponding redshifts, the age of the quasar APM 08279+5255 lies slightly further than 1σ beyond the age of the ΛCDM model at $z = 3.91$. By contrast, the holographic model is compatible at 1σ level with the age of the said quasar. The tension between the APM quasar and the ΛCDM model has been known for some time now (see [113] and references therein) and it has been revisited recently [114, 115].

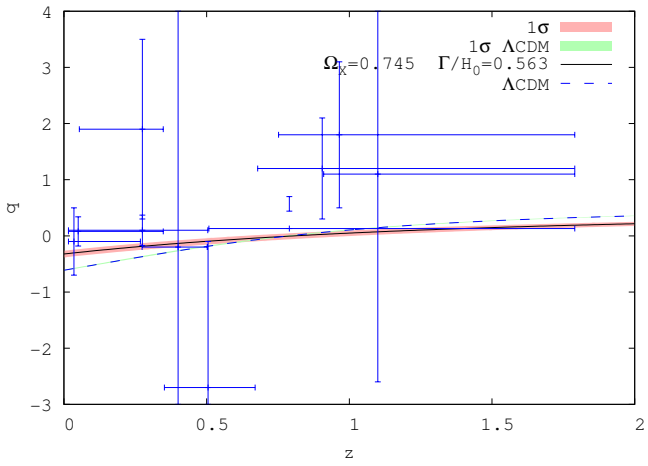

Figure 5.3: History of the deceleration parameter, according to Eq. (5.5) in terms of redshift for the best fit holographic model (solid line). The redshift at which the transition deceleration-acceleration occurs is approximately 0.80. Also shown is the prediction of the ΛCDM model (dashed line). In this, as well as in subsequent figures, the green swath indicates the region obtained by including the 1σ uncertainties of the constrained parameters used in the calculation (in the present case just Ω_{M0}). The data are borrowed from [108]. In drawing the curves no fit to these data was made.

5.2 Observational constraints

In this section we constrain the three free parameters (Ω_X, Γ/H_0, and H_0) of the holographic model presented above with observational data from SN Ia (557 data points), the CMB-shift, BAO, and gas mass fractions in galaxy clusters as inferred from X-ray data (42 data points), and the Hubble rate (15 data points) to obtain the best fit values.

5.2.1 SN Ia

We contrast the theoretical distance modulus defined in eq. (4.1) with the observed distance modulus $\mu_{obs}(z_i)$ of the 557 supernovae type Ia assembled

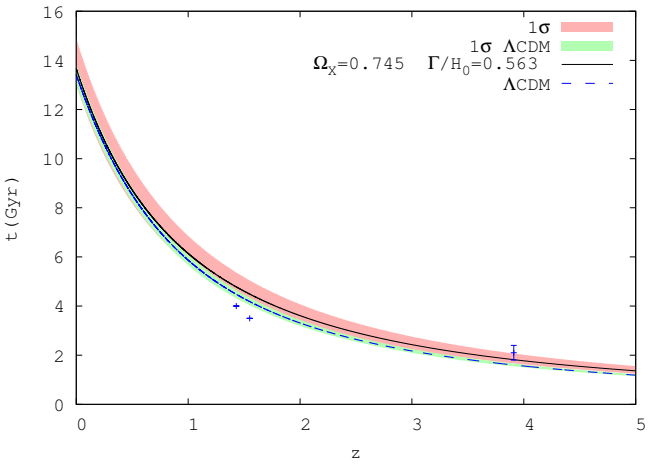

Figure 5.4: Dependence of the age of the Universe on redshift for the holographic model (solid line) and the ΛCDM model (dashed line). Also shown are the ages and redshifts of three old luminous objects, namely: galaxies LBDS 53W069, and LBDS 53091, and the quasar APM 08279+5255 - the latter with its 1σ error bar. In plotting the curves we have used the best fit value $H_0 = 68.1 \pm 2.1\,\mathrm{km/s/Mpc}$ for the holographic model and $H_0 = 72.1^{+1.8}_{-1.9}\,\mathrm{km/s/Mpc}$ for the ΛCDM model.

in the Union2 compilation [60]. The χ^2 from the 557 SN Ia is given by

$$\chi^2_{sn}(\mathbf{p}) = \sum_{i=1}^{557} \frac{[\mu_{th}(z_i) - \mu_{obs}(z_i)]^2}{\sigma^2(z_i)}\,, \tag{5.7}$$

and proceeding as explained in §4.1, we obtain $\tilde{\chi}^2_{sn} = \chi^{2\,(minimum)}_{sn} = 569.497$.

5.2.2 CMB shift

The CMB shift was introduced in §4.2.1. It is nearly model-independent and given by eq. (4.3) of §4.2.1. The 7-year WMAP data yields $\mathcal{R}(z_{rec}) = 1.725 \pm 0.018$ [70]. The best fit value of the model is $\mathcal{R}(z_{rec}) = 1.753^{+0.033}_{-0.027}$. Minimization of

$$\chi^2_{cmb}(\mathbf{p}) = \frac{(\mathcal{R}_{th} - \mathcal{R}_{obs})^2}{\sigma^2_{\mathcal{R}}} \tag{5.8}$$

produces $\chi^{2\,(minimum)}_{CMB-shift} = 2.385$.

5.2.3 BAO

As mentioned in §4.3, can be traced to pressure waves at the recombination epoch generated by cosmological perturbations in the primeval baryon-photon plasma. Here we use the ratio $D_v(0.35)/D_v(0.2) = 1.736 \pm 0.065$ [84] to fit the model. The best fit value for the holographic model is $D_v(0.35)/D_v(0.2) = 1.642 \pm 0.003$, and minimization of

$$\chi^2_{bao}(\mathbf{p}) = \frac{([D_v(0.35)/D_v(0.2)]_{th} - [D_v(0.35)/D_v(0.2)]_{obs})^2}{\sigma^2_{D_v(0.35)/D_v(0.2)}} \tag{5.9}$$

gives $\chi^{2\,(minimum)}_{bao} = 2.089$.

5.2.4 Gas mass fraction

As is well known, a very useful indicator of the overall cosmic ratio Ω_B/Ω_M, nearly independent of redshift, is the fraction of baryons in galaxy clusters [93] -see §4.5. We used 42 measurements of dynamically relaxed galaxy clusters in the redshift interval $0.05 < z < 0.1$ [94]. To fit the data we have employed the empirical formula (4.23). We fix the parameters K, A, γ, $b(z)$ and $s(z)$ to their respective best fit values which can be found in Ref. [94]. The χ^2 function from the 42 galaxy clusters reads

$$\chi^2_{X-rays}(\mathbf{p}) = \sum_{i=1}^{42} \frac{([f_{gas}(z_i)]_{th} - [f_{gas}(z_i)]_{obs})^2}{\sigma^2(z_i)}\,, \tag{5.10}$$

and its minimum value results to be $\chi^{2\,(minimum)}_{X-rays} = 44.758$. Figure 5.5 shows the fit to the data.

5.2.5 History of the Hubble parameter

To constrain the model we have used the $H(z)$ data mentioned in §4.6. Minimization of

$$\chi^2_{Hubble}(\mathbf{p}) = \sum_{i=1}^{15} \frac{[H_{th}(z_i) - H_{obs}(z_i)]^2}{\sigma^2(z_i)} \tag{5.11}$$

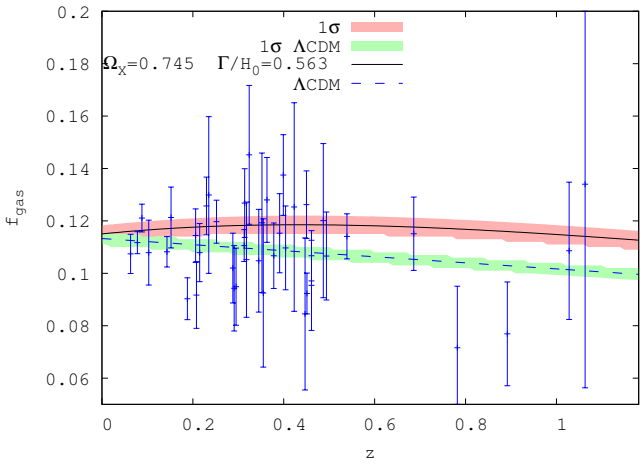

Figure 5.5: Gas mass fraction in 42 relaxed galaxy clusters vs. redshift. The solid and dashed curves correspond to the best fit models: holographic and ΛCDM, respectively. The data points with their error bars are taken from Table III in Ref. [94].

provided us with $\chi^{2\,(minimum)}_{Hubble} = 11.897$ and $H_0 = 68.1 \pm 2.1\,\mathrm{km/s/Mpc}$ as the best fit for the Hubble's constant. Figure 5.6 depicts the Hubble history according to the best fit holographic model alongside the best ΛCDM model.

Figures 5.7 and 5.8 summarize our analysis. The left panel of Fig. 5.7 depicts the 68.3% and 95.4% confidence contours for SN Ia (orange), CMB shift (brown), BAO (blue), X-ray (black), and H(z) (green), in the (Ω_X, Γ/H_0) plane. The joined constraints corresponding to χ^2_{total} are shown as shaded contours. The right panel depicts the 68.3% and 95.4% confidence regions in the (Ω_{X0}, H_0) plane of the holographic model (shaded regions) and the ΛCDM model (blue contours). As it is apparent, the models present a non-small overlap at 2σ level. Figure 5.8 depicts the normalized likelihoods, $\mathcal{L} \propto \exp(-\chi^2_{total}/2)$, of the three free parameters of the holographic model. Altogether, by constraining the holographic model presented in §5.1 with SN Ia, CMB-shift, BAO, X-rays, and H(z) data we obtain $\Omega_X = 0.745 \pm 0.007$, $\Gamma/H_0 = 0.563^{+0.017}_{-0.015}$, and $H_0 = 68.1 \pm 2.1\,\mathrm{km/s/Mpc}$ as best fit parameters, with $\chi^2_{total} = 630.627$. This value lies well inside the 1σ interval ($\chi^2_{total\ dof} \approx 1.03$). It should be noted that the non-interacting case is discarded at a very

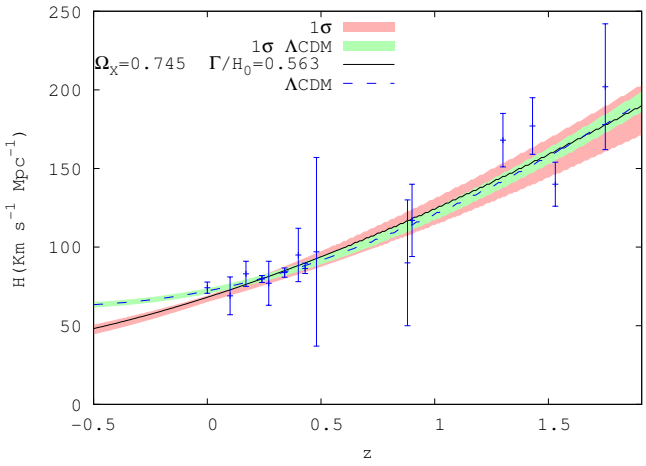

Figure 5.6: Plot of $H(z)$ for the best fit values of the holographic model (solid line) and the ΛCDM model (dashed line). The data points and error bars are borrowed from Refs. [95, 96, 97].

Model	χ^2_{sn}	χ^2_{cmb}	χ^2_{bao}	χ^2_{X-rays}	χ^2_H	χ^2_{total}	$\chi^2_{\text{total } dof}$
Holographic	569.497	2.385	2.089	44.758	11.897	630.627	1.03
ΛCDM	541.833	0.013	1.047	41.527	8.727	593.142	0.97

Table 5.1: χ^2 values for the best fit holographic model ($\Omega_X = 0.745 \pm 0.007$, $\Gamma/H_0 = 0.563^{+0.017}_{-0.015}$, and $H_0 = 68.1 \pm 2.1$ km/s/Mpc), and the best fit ΛCDM model ($\Omega_{M0} = 0.259^{+0.006}_{-0.005}$, and $H_0 = 72.1^{+1.8}_{-1.9}$ km/s/Mpc).

high confidence level. This is not a surprise at all since for $\Gamma = 0$ the model reduces to the Einstein-de Sitter ($\Omega_M = 1$, $\Omega_X = 0$) and accordingly, as Eq. (5.5) tells us, the transition from deceleration to acceleration cannot occur.

Table 5.1 shows the partial, total, and total χ^2 over the number of degrees of freedom of the holographic model along with the corresponding values for the ΛCDM model. In the latter one has just two free parameters, Ω_{M0} and H_0. Their best fit values after constraining the model to the data are $\Omega_{M0} = 0.259^{+0.006}_{-0.005}$, and $H_0 = 72.1^{+1.8}_{-1.9}$ km/s/Mpc, with $\chi^2_{total} = 593.142$. We see that the ΛCDM model fits the data better than the holographic model in spite of having one parameter less. Thus, the former model should be preferred on statistical grounds. Nevertheless, this does not tell the whole story; the ΛCDM cannot address the cosmic coincidence problem and has

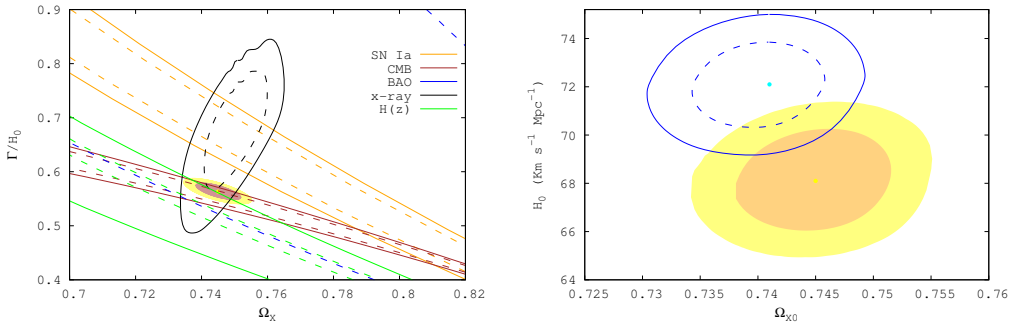

Figure 5.7: Left panel: the 68.3% and 95.4% confidence contours for the pair of free parameters (Ω_X , Γ/H_0) obtained by constraining the holographic model with SN Ia+CMB-shift+ BAO+X-ray+H(z) data. The joined constraints corresponding to χ^2_{total} are rendered as shaded contours. The no interacting case is largely disfavored by the data. Right panel: the 68.3% and 95.4% confidence contours for the pair (Ω_{X0} , H_0) of the holographic model (shaded contours) and the ΛCDM model (blue contours). The solid points signal the location of the best fit values. Notice the overlap at 2σ confidence level between both models.

some tension with the age of the old quasar APM 08279+5255. By contrast, the holographic model answers the said problem and shows compatibility, at 1σ, with the age of the old quasar.

5.3 Evolution of the growth function

It is not unfrequent to find in the literature cosmological models that differ greatly on their basic assumptions but, nevertheless, present a rather similar dynamical behavior. It is, therefore, rather hard to discriminate them at the background level. However, their differences are more readily manifested at the perturbative level (though, admittedly, the uncertainty in the corresponding data are, in general, wider). This justifies our interest in studying the evolution of the matter perturbations of the holographic model inside the horizon. A prime tool in this connection is the growth function, defined as

$$f \equiv d\ln\delta_M/d\ln a\,, \tag{5.12}$$

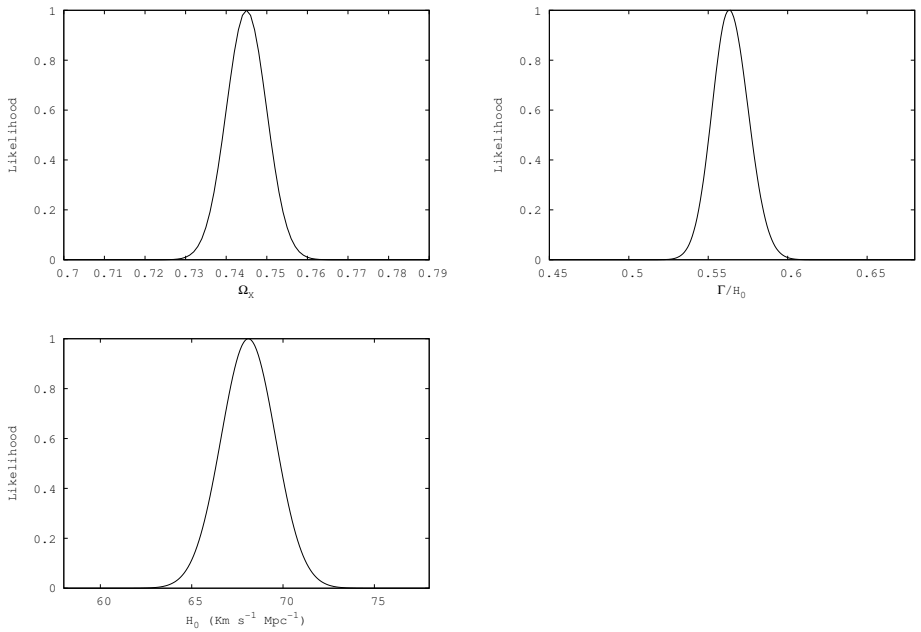

Figure 5.8: The normalized likelihoods of Ω_X, Γ/H_0, and H_0.

where δ_M denotes the density contrast of matter. In order to derive an evolution equation for f, we start from the energy balance for the matter component in the Newtonian approximation

$$\dot{\delta}_M - \frac{k^2}{a^2}\, v_M = -\frac{Q}{\rho_M}\, \delta_M + \frac{\hat{Q}}{\rho_M}\,. \tag{5.13}$$

Here, v_M is the velocity potential, defined by $\hat{u}_{M\alpha} \equiv v_{M,\alpha}$, where $u_{M\alpha}$ is the matter four-velocity, and the hat means perturbation of the corresponding quantity. Recalling Eqs. (5.1) and (5.2) and that Γ and r do not vary, we can write

$$\dot{\delta}_M - \frac{k^2}{a^2} v_M = -\frac{\Gamma}{r}\left(\delta_M - \delta_X\right)\,. \tag{5.14}$$

Usually, the density contrast of dark energy is neglected under the assumption that dark energy does not cluster on small scales. However, as forcefully argued by Park *et al.* [116], the neglecting of the perturbation in the dark energy component can be fully justified in the case of the cosmological constant only. At any rate, in the present case the setting of δ_X to zero wold be

incorrect given the coupling between both energy components at the background level (i.e., Eqs. (5.1)). It seems therefore reasonable to include a coupling, at least approximately, also at the perturbative level. The simplest possibility is to assume a proportionality $\delta_X = \alpha\,\delta_M$ with α a constant. As we shall see, the only consistent choice for this constant (under the conditions that Γ and r are held fixed) is $\alpha = 1$. Thus, Eq. (5.14) becomes

$$\dot{\delta}_M - \frac{k^2}{a^2} v_M = -\frac{\Gamma}{r}\,(1-\alpha)\,\delta_M\,. \tag{5.15}$$

An equation for v_M follows from the momentum conservation of the matter component. Assuming that there is no source term in the matter rest frame, this equation takes the simple form

$$\dot{v}_M + \phi = 0\,, \tag{5.16}$$

where ϕ is the Newtonian potential. Differentiation of (5.15), use of (5.16) and (5.15), and substitution of the scale factor for the time as independent variable, leads to

$$\delta_M'' + \tfrac{3}{2a}\left[1 + \tfrac{\Gamma}{3Hr} + \tfrac{2(1-\alpha)}{3}\tfrac{\Gamma}{Hr}\right]\delta_M' - \tfrac{3}{2a^2}\tfrac{r+\alpha}{r+1}\left[1 - \tfrac{4(1-\alpha)}{3}\tfrac{\Gamma}{Hr}\tfrac{r+1}{r+\alpha}\right]\delta_M = 0 \quad , \tag{5.17}$$

where use of Friedmann's equation, $4\pi G\rho_M = \frac{3}{2}H^2\frac{r}{1+r}$, has been made; the prime means derivative with respect to a. For a vanishing Γ we must recover the conventional perturbation equation $\delta_M'' + \frac{3}{2a}\delta_M' - \frac{3}{2a^2}\delta_M = 0$ with the growing solution $\delta_M \propto a$ for a dust universe. Clearly, this is only feasible for $\alpha = 1$. With this choice the fractional matter perturbation δ_M coincides with the total fractional energy density perturbation, $\delta \equiv \frac{\hat{\rho}_M + \hat{\rho}_X}{\rho_M + \rho_X}$. It follows that the basic matter perturbation equation for the interacting holographic models reduces to

$$\delta_M'' + \frac{3}{2a}\left[1 + \frac{\Gamma}{3Hr}\right]\delta_M' - \frac{3}{2a^2}\delta_M = 0\,. \tag{5.18}$$

Replacing δ_M by the growth function f, last equation becomes

$$f' + f^2 + \frac{1}{2}\left(1 + \frac{\Gamma}{Hr}\right) f - \frac{3}{2} = 0 \tag{5.19}$$

with $f' := df/d\ln a$. This has the advantage of being a first order differential equation. Notice that in the absence of interaction, $\Gamma = 0$, its solution is simply $f = 1$ as it should, i.e., a dust dominated universe.

Figure 5.9 depicts the evolution of the growth function in terms of the redshift for the holographic as well as for the ΛCDM model. The latter appears to fit the data below $z \simeq 0.6$ better than the former. In particular, at $z = 0.15$ the best fit holographic model deviates $\Delta f = 0.3$ (corresponding to 3σ) from the observed value (though it falls within 1σ with the remaining data points) while the best fit ΛCDM model falls within 1σ also at $z = 0.15$.

At any rate, it has been recently pointed out, from the observation of nearby galaxies, that structure formation must have proceeded faster than predicted by the ΛCDM model [118]. Clearly, slightly enhanced values of f at low redshifts helps accelerate the formation of galaxies and clusters thereof.

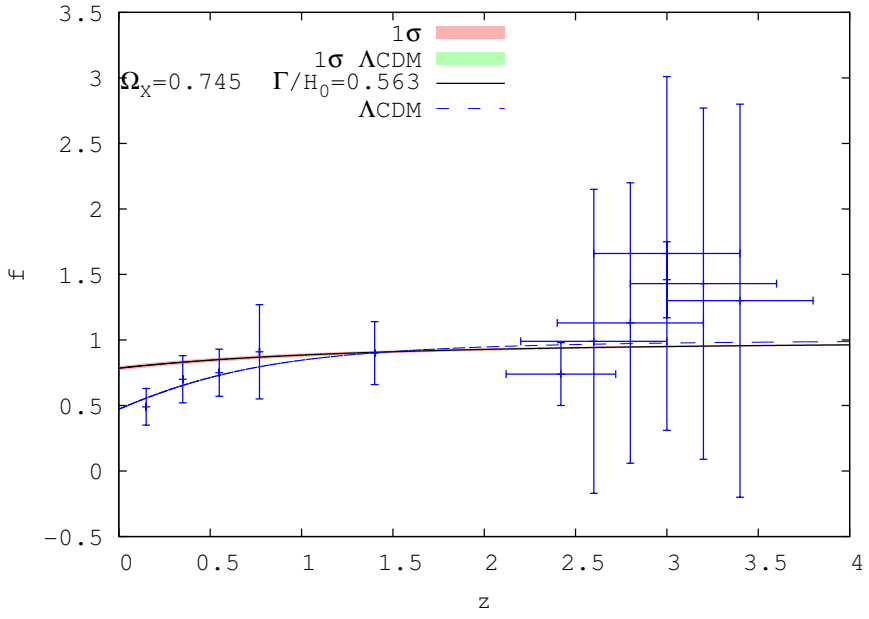

Figure 5.9: Growth function vs. redshift for the best fit holographic model (solid line). Also shown is the prediction of the ΛCDM model (dashed line). The observational data are borrowed from Table II in Ref. [117]. In plotting the curves no fit to these data was made.

5.4 Temperatures anisotropies

Up to here we have neglected radiation and baryons, but if we wish to compute temperature anisotropies we can't do so. We need to introduce photons and also baryons in the energy content of the Universe, in a similar way as we will do in §6.8. We then obtain

$$\left(\frac{H}{H_0}\right)^2 = \left[\frac{\Gamma}{3H_0 r} + \left(1 - \frac{\Gamma}{3H_0 r}\right) a^{-3/2}\right]^2 + \Omega_{R0} a^{-4}\,, \tag{5.20}$$

where baryons are included as a part of the non radiation terms.
To compute the C_ls introduced in §4.2.3 and the $P(k)$ depicted in §4.4 we need to solve the (non) conservation equations for the density and velocity perturbations, for instance in synchronous gauge (we could have done it as well in Newtonian), i.e., eqs. (3.60) and (3.61). If we impose the dark matter particles to follow geodesics (see §3.6.1) for the interaction introduced in §5.1 we obtain for cold dark matter

$$\delta'_{CDM} = -\frac{h'}{2} + \frac{a\Gamma\rho_X}{\rho_{CDM}}\left(\delta_X - \delta_C\right)\,, \tag{5.21}$$

and for dark energy

$$\begin{aligned}\delta'_X &= -3\mathcal{H}(c^2_{s\,X} - w_X)\delta_X - (1+w_X)\left(\theta_X + \tfrac{h'}{2}\right)\\ &-3\mathcal{H}\left[3\mathcal{H}(1+w_X)(c^2_{s\,X} - w_X) + w'_X\right] + a\Gamma\left[+3\mathcal{H}\left(c^2_{s\,X} - w_X\right)\tfrac{\theta_X}{k^2}\right]\,,\end{aligned} \tag{5.22}$$

$$\theta'_X = -\mathcal{H}(1 - 3c^2_{s\,X})\theta_X + \tfrac{c^2_{s\,X}}{(1+w_X)}k^2\delta_X + \tfrac{a\Gamma}{(1+w_X)}\left(1 + c^2_{s\,X}\right)\,. \tag{5.23}$$

All background quantities can be computed from previous sections, but we need to define $c^2_{s\,X} \ll 1$ in order to reproduce a matter like behavior with the dark energy component. Doing so and modifying the CLASS code [82], we obtain the temperature anisotropies, Fig. 5.10. To compute them, we have used the same parameters value obtained in §5.2. Notice that, even when the temperatures anisotropies are not fitted with data, the result shown in Fig. 5.10 is quite close to the concordance ΛCDM, so our model will probably reproduce the CMB data. When computing the matter power spectrum in this particular model, it is not obvious the way one should define the matter density perturbations. The dark energy, both at background and perturbative level, behaves as cold dark matter for $z \gg 1$. For this reason it deserves further development to be done elsewhere.

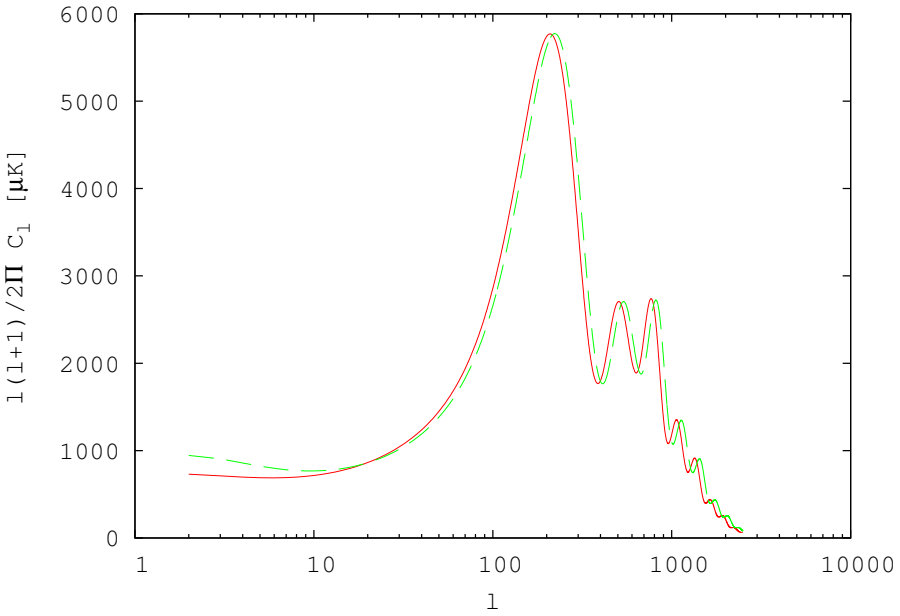

Figure 5.10: Temperature anisotropies. Solid (red) lines are for the holographic model with the parameter obtained in 5.2. Dashed (green) lines are for the ΛCDM model with $\Omega_{\Lambda\,0} = 0.7$, $\Omega_{CDM\,0} = 0.25$ and $H_0 = 70$ km s^{-1} Mpc^{-1}

5.5 Concluding remarks

We constrained the interacting holographic model of §5.1 with data from SN Ia, CMB shift, BAO, the gas mass fraction in galaxy clusters, and $H(z)$. The parameters of the best fit model are: $\Omega_X = 0.745 \pm 0.007$, $\Gamma/H_0 = 0.563^{+0.017}_{-0.015}$, and $H_0 = 68.1 \pm 2.1$ km/s/Mpc. We have not included data of the growth function in the likelihood analysis given the wide uncertainties of the current data. However, we have derived the differential equation for f, Eq. (5.19), and integrated it numerically for the best fit model.

It conforms reasonably well to the observational data but not so well as the ΛCDM model (best fit values: $\Omega_{M0} = 0.259^{+0.006}_{-0.005}$, $H_0 = 72.1^{+1.8}_{-1.9}$ km/s/Mpc) does notwithstanding the latter has one less free parameter than the former. However, the holographic model greatly alleviates the cosmic coincidence problem and seems compatible at 1σ level with the age of the old quasar APM 08279+5255. Besides, the observational data from the

CMB shift, BAO, X-ray, and some of the $H(z)$ data, are not fully model independent owing to the fact that they are extracted with the help of the conventional ΛCDM. This frequently makes the latter tend to be observationally favored over any other cosmological model. Moreover, the BAO data are conventionally determined under the assumption of purely adiabatic perturbations. However, as recently argued [119], should isocurvature components be present the shape and location of the CMB acoustic peaks would be altered and the data extracted from BAO affected. Clearly, we must wait for more abundant, varied, and model-independent accurate data to decide which of the two models survives. If eventually neither of the two does, we should not be so much disenchanted because, at any rate, this "negative" result would have narrowed the parameter space of dark energy.

Chapter 6

Holographic dark energy described at the Hubble length[1]

6.1 Introduction

In this section, we study some general features of holographic dark energy models where the IR cutoff is defined by the Hubble radius. We will show that, in general, identical cosmological backgrounds can be described by an **interacting** holographic dark energy model with a **constant** holographic parameter c^2 or, alternatively, by a **non-interacting** holographic dark energy model with a parameter **weakly varying on time** (hereafter denoted by $\tilde{c}^2$). In spite of the global evolution in both scenarios being the same, the energy densities and the EoS parameters, etc, can behave rather differently. In what follows, quantities referring to holographic models with variable c^2 will be noted by a tilde. They obey

$$\tilde{\rho}_M = 3M_P^2(1-\tilde{c}^2)H^2 \qquad \text{and} \qquad \tilde{\rho}_X = 3M_P^2\tilde{c}^2H^2\,. \tag{6.1}$$

as well as

$$\dot{\tilde{\rho}}_M = -3H\tilde{\rho}_M \qquad \text{and} \qquad \dot{\tilde{\rho}}_X = -3H(1+\tilde{w})\tilde{\rho}_X\,, \tag{6.2}$$

i.e., we assume that their energy densities conserve separately.
In the interacting scenario, the (non) conservation equations read

$$\dot{\rho}_M + 3H\rho_M = Q \qquad \text{and} \qquad \dot{\rho}_X + 3H(1+w)\rho_X = -Q\,. \tag{6.3}$$

[1]This Chapter corresponds to Ref. [120].

and the EoS parameter

$$w = -\frac{Q}{3(1-c^2)\rho_X H} \tag{6.4}$$

We remark that in any holographic interacting model defined at the Hubble scale, independently of the nature of the interaction, dark energy and cold dark matter share the same dependence on H, and thus present the same background evolution. By rewriting Eqs. (6.3) as

$$\begin{aligned} \dot{\rho}_M + 3H\left(1 - \frac{Q}{3H\rho_M}\right)\rho_M &= 0\,, \\ \dot{\rho}_X + 3H\left(1 + w + \frac{Q}{3H\rho_X}\right)\rho_X &= 0 \end{aligned} \tag{6.5}$$

and using Eq.(6.4) both components share the same effective EoS parameter, $w_{eff} \equiv -\frac{Q}{3H\rho_M}$. We will return to this later on. We shall also re-consider the coincidence problem from the point of view of non-interacting models where the energy densities ratio, $\tilde{r} \equiv \tilde{\rho}_M/\tilde{\rho}_X$, is not a constant.

6.2 Background equivalence between interacting and $\tilde{c}^2$ models

In order to show that every interacting model can be considered as a non-interacting one (with a $\tilde{c}^2$ parameter varying in time) at the background level (i.e., both models give rise to the same Hubble function), we must first verify that both energy densities are positive. By Eqs. (6.1), this condition implies $0 \leq \tilde{c}^2 \leq 1$.

From the Friedmann equations (2.17) and (2.18) and (6.3.2) we obtain

$$\dot{H} = -\frac{3}{2}H^2\left(1 + \tilde{c}^2\tilde{w}\right)\,. \tag{6.6}$$

For the non-interacting model, from Eq. (6.3.1) we have that $\tilde{\rho}_M = \tilde{\rho}_{M\,0}a^{-3}$ remains always positive.

We must also verify that $\tilde{\rho}_X$ is positive, i.e., that $\tilde{c}^2 \geq 0$. Since by hypothesis interacting and $\tilde{c}^2$ models share the same $H(z)$, Eq. (2.18) implies

$$\frac{\tilde{c}^2(z)}{c^2} = \frac{w(z)}{\tilde{w}_(z)}\,, \tag{6.7}$$

where z is the redshift. Thus, if the non-interacting dark energy has a negative EoS parameter $\tilde{w}(z)$, since $w(z) \leq 0$ and $c^2 \geq 0$, then $\tilde{\rho}_X$ and $\tilde{c}^2(z)$,

cannot be negative.

Since $\rho_M \geq 0$ and $\tilde{c}^2 \leq 1$, by differentiating Eq. (6.3.2), using Eqs. (6.4), (6.6) and (6.7), and recalling that $Q > 0$, we obtain

$$\frac{d\tilde{c}^2}{dt} = \frac{1-\tilde{c}^2}{\rho_M} Q \geq 0\,. \tag{6.8}$$

As shown in [33], the condition $\frac{d\tilde{c}^2}{dt} \geq 0$ must be fulfilled for thermodynamical reasons. Thus, we conclude that the Hubble function of any holographic interacting model with $Q \geq 0$ and c^2 constant, also corresponds to an holographic non-interacting model ($Q = 0$) of dark energy ($\tilde{w} \leq 0$), with $\tilde{c}^2$ obeying $0 \leq \tilde{c}^2(t) \leq 1$ and $\frac{d\tilde{c}^2}{dt} \geq 0$, and vice versa. It is also note-worthy that despite both models being equivalent at the background level, they share the same $H(z)$, their energy components evolve diversely. In the interacting case, the Hubble function will never have c^2 as a free parameter, but it will be multiplied by the constants in the interacting term Q, as can be seen by using Eq. (6.6) in Eq. (6.4). This means that, as long as $\Omega_X = c^2$, the $\Omega_{X\,0}$ parameter can not be fitted, because we have neither observational nor theoretical constraints on the interaction and so, the dependence on them is degenerated. On the other hand, in the $\tilde{c}^2$ model it has the fixed value, $\tilde{\Omega}_{X\,0} = \tilde{c}^2(z=0)$. Consequently, at background level is not possible, in principle, to discriminate interacting models from $\tilde{c}^2$ ones. Nevertheless, as we shall see in section 6.6, they are distinguishable at the perturbative level.

6.3 Observational constraints

To constrain the free parameters of the Hubble holographic models presented below (sections 6.4 and 6.5) we shall use observational data from SN Ia Union2 set (557 data points) [60], BAO [84], the acoustic scale l_A [70], gas mass fractions in galaxy clusters as inferred from X-ray data (42 data points) [94] and the Hubble rate (15 data points) [95, 96, 97, 98]. For details see §4 and §5.2.

6.4 Model 1

Let us now consider the holographic interacting model studied in §5 to construct its equivalent $\tilde{c}^2(t)$ model. In the former the IR cutoff is also set by

the Hubble length and the interaction term was taken as $Q \equiv 3AH_0\rho_M$, with A a semipositive definite constant, related to the constant decay rate, Γ, of dark energy into cold dark matter by $A \equiv \frac{\Gamma}{3H_0 r}$. The corresponding Hubble function is

$$H = H_0 \left(A + (1-A)(1+z)^{\frac{3}{2}} \right) , \tag{6.9}$$

and the equation of state parameter

$$w = -\frac{A}{\Omega_X}\frac{H_0}{H}, \tag{6.10}$$

follows from Eq. (6.4) and the fact that $\Omega_X = c^2$ and $\Omega_M = 1 - c^2$. Notice that here the density parameters, $\Omega_i \equiv \frac{\rho_i}{3M_P^2 H^2}$ $(i = M, X)$ are constant. The model fits reasonably well the observational data and is consistent with the age of the old quasar APM 08279+5255 [112, 113], something that ΛCDM is not at 1σ confidence level.

This model presents an unexpected similarity to the Chaplygin gas model [43]. To see this, bear in mind that in any Hubble holographic interacting model cold dark matter and dark energy share the same effective EoS parameter, $w_{eff} = -Q/(3H\rho_M)$. Multiplying it by the total energy density we get the total pressure

$$P = w_{eff}\,\rho = -3^{\frac{1}{2}} A\, M_P\, H_0\, \rho^{\frac{1}{2}} . \tag{6.11}$$

This expression is formally identical to the pressure of the generalized Chaplygin gas, $P = -\beta\rho^{-\alpha}$ [43]. As is well known, for $\alpha < 0$ and $\beta > 0$, it may imply instabilities since the squared adiabatic sound speed ($c_{s\,a}^2 \equiv \frac{\dot{P}}{\dot{\rho}}$) is negative. Due to the interaction, we can take account of non adiabatic processes, and so consider an effective speed of sound. In §6.9 we find a Lagrangian formulation with a standard scalar field ϕ_Q for both models (the interacting and the $\tilde{c}^2$) with an effective speed of sound given by $c_s^2 = 1$.

Notice that while in the interacting case $r = \rho_M/\rho_X$ is a constant, in the non-interacting one, $\tilde{r}$ may vary with time. We expand $H^2(z)$ and assume that the term proportional to $(1+z)^3$, corresponds to the usual matter term in Friedmann's equation, and identify the remainder as the dark energy density. Thus,

$$\frac{M_P^{-2}}{3H_0^2}\tilde{\rho}_M = (1-A)^2(1+z)^3 \tag{6.12}$$

and

$$\frac{M_P^{-2}}{3H_0^2}\tilde{\rho}_X = A^2 + 2\,A(1-A)(1+z)^{\frac{3}{2}} , \tag{6.13}$$

and from Eqs. (6.1.2), (6.9) and (6.13) it follows that

$$\tilde{c}^2 = \frac{2A(1-A)(1+z)^{\frac{3}{2}} + A^2}{\left(A + (1-A)(1+z)^{\frac{3}{2}}\right)^2}\,. \tag{6.14}$$

In consistency with the findings of [33], $\tilde{c}^2$ never decreases and tends from below to a constant value in the far future,

$$\tilde{c}^2_{z\to\infty} = 0\,, \qquad \tilde{c}^2_{z\to 0} = 1-(1-A)^2\,, \qquad \tilde{c}^2_{z\to -1} = 1\,, \tag{6.15}$$

where $0 \leq A \leq 1$ from observations. Table 6.1 shows the best fit values of the parameters and their 1σ errors. Table 6.2 presents the χ^2 of model 1 and ΛCDM, obtained by fitting each data set independently, and the total χ^2. The obtained χ^2 per degree of freedom (dof) is $\chi^2_{dof} = 1.00$. Notice that $(1-A)^2 = \tilde{\Omega}_{M0}$ and its value (≈ 0.17) is about 6σ lower than the one reported by Komatsu *et al.* [70]. However, this value is reached by using the last scattering sound horizon as a standard ruler; i.e., it is not observed directly but by integrating the background evolution. So truly, just a global background evolution is obtained, that in the case of ΛCDM, gives the value of Ω_{M0} mentioned above, but in other models, as in this one, it can vary. Figure 6.1 shows the 1σ and 2σ confidence regions and the best fit value of the free parameters of the models.

Model	$\Omega_{X\,0}$	H_0	A
Interacting holographic	0.73	69.4 ± 1.7	0.588 ± 0.004
$\tilde{c}^2$ holographic	0.830 ± 0.003	69.4 ± 1.7	0.588 ± 0.004
ΛCDM	0.720 ± 0.003	$71.5^{+1.3}_{-1.5}$	—

Table 6.1: Values of the parameters of the models obtained by constraining them with the observational data described in Section 6.3. $\Omega_{X\,0}$ is not a free parameter in any of the two holographic scenarios, but it is included for the sake of comparison with the conventional ΛCDM model. Notice that despite the holographic models being described by the same Hubble function they have different values of $\Omega_{X\,0}$. This point does not discard any model, since the value from WMAP7 [70] is obtained using the last scattering surface as a standard ruler, i.e., integrating the ΛCDM background evolution from the last scattering surface to the present time. Thus, if the Hubble function is the same for different models, geometric data alone can not distinguish between them. The H_0 values are given in km s^{-1} Mpc^{-1}.

Although H(z) coincides with the corresponding expression in [99], neither ρ_M nor ρ_X, nor $w(z)$ do. The functional form of $\tilde{w}$ coincides with that of the EoS parameter for the interacting case - cfr. Eq. (6.10)-,

$$\tilde{w} = -\frac{A}{\tilde{\Omega}_X}\frac{H_0}{H} \tag{6.16}$$

Model	χ^2_{SN}	χ^2_{BAO}	$\chi^2_{l_A}$	χ^2_{X-ray}	χ^2_H	$\chi^2_{\rm tot}$	$\chi^2_{\rm tot\ dof}$
Model 1	554.8	1.7	0.3	44.9	11.3	613.0	1.00
ΛCDM	542.7	1.2	0.7	42.3	8.8	595.7	0.97

Table 6.2: χ^2 values for the holographic model of sec. 6.4 and ΛCDM model. Each of them has two free parameters (A and H_0 the holographic, and $\Omega_{X\,0}$ and H_0 the ΛCDM).

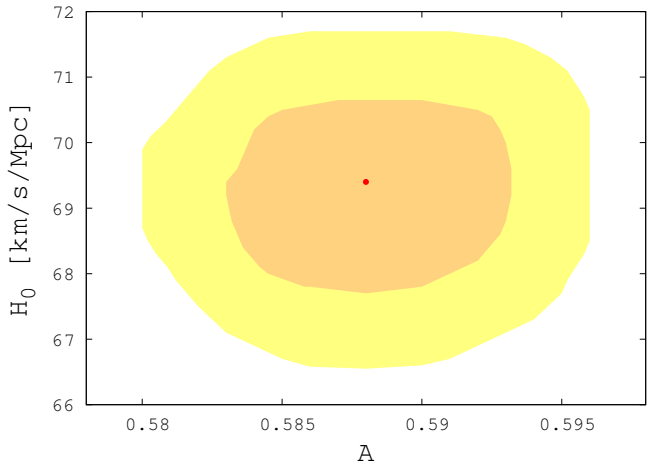

Figure 6.1: 1σ and 2σ confidence regions for the parameters A and H_0 of model 1. The plot holds for both scenarios, the interacting and the $\tilde{c}^2(t)$ (non-interacting). The dot indicates the best fit values.

but has a different time dependence since $\Omega_X \neq \tilde{\Omega}_X$, as the left panel of Fig. 6.2 shows. Notice that in the interacting case, w crosses the phantom divide line ($w = -1$). However, the w_{eff} defined in the line below Eq. (6.5), does not cross the said line. The pressure, obtained by multiplying Eq. (6.16) by Eq. (6.1.2) and using Eq. (6.9), described here for later purposes, reads

$$\tilde{P} = \tilde{w}\tilde{\rho}_X = -3AM_P^2H_0^2\left[A + (1-A)(1+z)^{\frac{3}{2}}\right] . \qquad (6.17)$$

As shown in the right panel of Fig. 6.2, the coincidence problem is solved (i.e., r is constant) in the interacting case (solid green line). By contrast, in the $\tilde{c}^2$ model (thin dot dashed red lines), it is not solved but is much less severe than in the ΛCDM model (thick short dashed blue line).

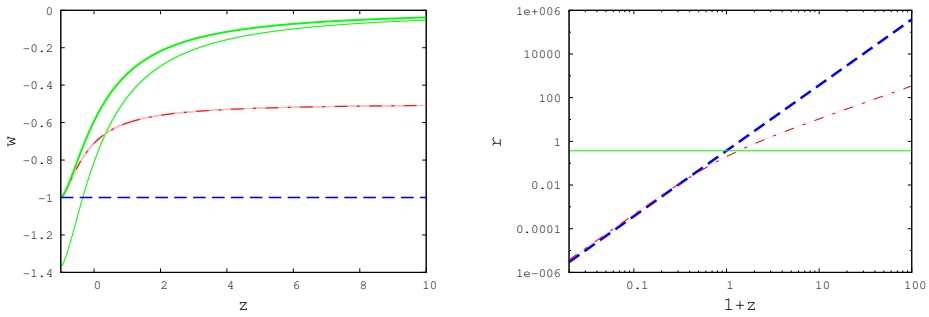

Figure 6.2: Left panel: EoS parameter for the interacting (w thin line, and w_{eff} thick line), the $\tilde{c}^2$ and ΛCDM models. Right panel: energy densities ratios, $r = \rho_M/\rho_X$, versus $1+z$ for the ΛCDM, the interacting and the $\tilde{c}^2$ models. All the graphs were plotted using the best fit values of the parameters, shown in table 6.1. Solid (green) lines are used for the interacting case, thin dot dashed (red) lines for the $\tilde{c}^2$ model, and thick short dashed (blue) for ΛCDM. The 1σ region of the parameters is also plotted, but due to the very small errors, it results nearly inappreciable.

6.5 Model 2

In this model, cold dark matter and dark energy evolve separately (i.e., $Q = 0$) but the holographic parameter $\tilde{c}^2$ varies slowly with time. In order to have $0 \leq \tilde{c}^2 \leq 1$, and $\frac{d\tilde{c}^2}{dt} \geq 0$ we use the parametrization

$$\tilde{c}^2 = \frac{1}{1 + \tilde{r}_0(1+z)^\epsilon} \tag{6.18}$$

where $\tilde{r}_0 \equiv \frac{\tilde{\Omega}_{M0}}{\tilde{\Omega}_{X0}}$ and ϵ a semipositive definite constant (notice that $\tilde{c}^2(z = 0) = \tilde{\Omega}_{X0}$). In this case, the Hubble function

$$H = H_0\sqrt{\tilde{\Omega}_{M0}(1+z)^3 + \tilde{\Omega}_{X0}(1+z)^{3-\epsilon}} \tag{6.19}$$

coincides with the Hubble function of the spatially flat wCDM model with $\tilde{w} = -\frac{\epsilon}{3}$. It obviously reduces to the ΛCDM model for $\epsilon = 3$. If we consider the Hubble function in Eq.(6.19) as coming from an interaction between dark energy and dark matter, by Eq. (6.4) the interacting term would be

$$Q = -3\,c^2\,w\rho_M H\,, \tag{6.20}$$

where the EoS parameter of the interacting case is $w = -\frac{\epsilon}{3c^2(1+\tilde{r}_0(1+z)^\epsilon)}$. The variation of $\tilde{c}^2$, breaks the holographic dependence of dark energy density. But as for the rate of variation of $\tilde{c}^2$ we must have $\frac{d\tilde{c}^2}{dt}/c^2 =$

$\epsilon\tilde{r}_0(1+z)^\epsilon H/(1+\tilde{r}_0(1+z)^\epsilon) \lesssim H$, it may be considered as a small variation at the level of saturation. For the last inequality to be fulfilled, $f(z) \equiv \epsilon\Omega_{M0}(1+z)^\epsilon/(\Omega_{X0}+\Omega_{M0}(1+z)^\epsilon) \leq 1$. This is not always true in the past, but the maximum value of $f(z)$, that is monotonously decreasing, is $f(z \to \infty) = \epsilon$. Using the best fit value for ϵ, shown in table 6.3, its maximum variation rate is of the order of the expansion rate, and the model can still be considered holographic. The χ^2 values obtained by fitting the model with the different data sets, are shown in table 6.3. The χ^2 per degree of freedom obtained with the fit of all the data sets together is $\chi^2_{dof} = 0.97$. The left panel of Fig. 6.3 shows that the EoS parameter w (thin solid green line) cross the phantom divide line but the effective one w_{eff} (thick solid green line) of the interacting case does not. The non-interacting case, as we have mentioned before, is just a wCDM model with $w = -\frac{\epsilon}{3}$ (thin dot dashed red line). The right panel of Fig. 6.3 shows that the interacting model (solid green line) solves the coincidence problem, and in the case of the $\tilde{c}^2$ one (thin dot dashed red line), it overlaps the ΛCDM line (thick short dashed blue line), since $w \gtrsim -1$. Fig. 6.4 depicts the 1σ and 2σ regions for the parameters $\tilde{r}_0$ and H_0 (left panel) and $\tilde{r}_0$ and w_0 (right panel). Both panels are the same for both scenarios, the interacting and the $\tilde{c}^2$, however, $\tilde{r}_0$ is only related to the dark energy and cold dark matter densities in the $\tilde{c}^2$ description; in the interacting case it has no physical meaning. In both cases today's value of the EoS is the same $w_0 = \tilde{w}_0 = -\frac{\epsilon}{3}$, as the left panel of Fig. 6.3 shows.

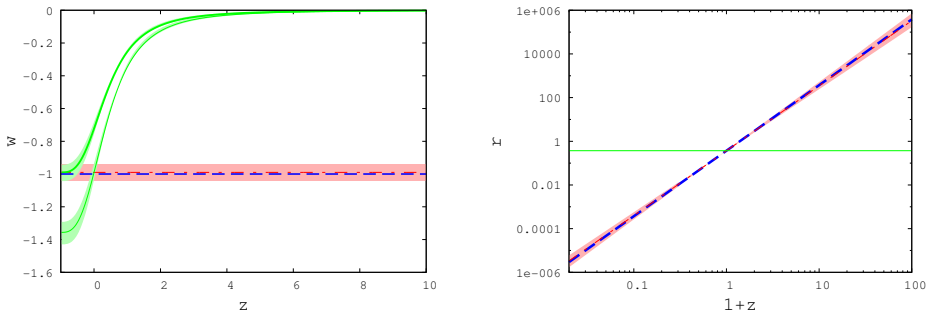

Figure 6.3: Left panel: EoS parameter for the the interacting (w with thin line, and w_{eff} with thick line), the $\tilde{c}^2$ and ΛCDM models. Right panel: energy densities ratios, $r \equiv \rho_M/\rho_X$, versus $1+z$ for the ΛCDM, the interacting and the $\tilde{c}^2$ models. Notice that the energy densities ratio of the $\tilde{c}^2$ and ΛCDM models practically overlap. All graphs were drawn using the best fit values of the respective parameters, shown in table 6.3. Solid (green) lines are used for the interacting case, thin dot dashed (red) lines for the $\tilde{c}^2$, and thick short dashed blue for ΛCDM. The 1σ region of the parameters is also plotted.

Model	$\Omega_{X\,0}$	H_0	$\tilde{r}_0$	ϵ
Interacting holographic	0.73	71.5 ± 2.6	0.370 ± 0.013	$2.97^{+0.16}_{-0.14}$
$\tilde{c}^2$ holographic	0.730 ± 0.007	71.5 ± 2.6	0.370 ± 0.013	$2.97^{+0.16}_{-0.14}$
ΛCDM	0.720 ± 0.003	$71.5^{+1.3}_{-1.5}$	—	—

Table 6.3: Best fit values of the free parameters of the models. In the $\tilde{c}^2$ holographic scenario, $\Omega_{X\,0}$ is obtained from the free parameter $\tilde{r}_0$, so the model has only three free parameters. In the interacting one, for $\Omega_{X\,0}$ we use the value obtained in [70]. The H_0 values are given in $km/s/Mpc$.

Model	χ^2_{SN}	χ^2_{BAO}	$\chi^2_{l_A}$	χ^2_{X-ray}	χ^2_H	$\chi^2_{\rm tot}$	$\chi^2_{\rm tot\ dof}$
Model 2	542.7	1.2	0.0	41.5	8.8	594.2	0.97
ΛCDM	542.7	1.2	0.7	42.3	8.8	595.7	0.97

Table 6.4: χ^2 values for the holographic model studied in Sec. 6.5 and for ΛCDM model. In the former, the free parameters are $\tilde{r}_0$, ϵ and H_0. In the latter the free parameters are two, $\Omega_{X\,0}$ and H_0.

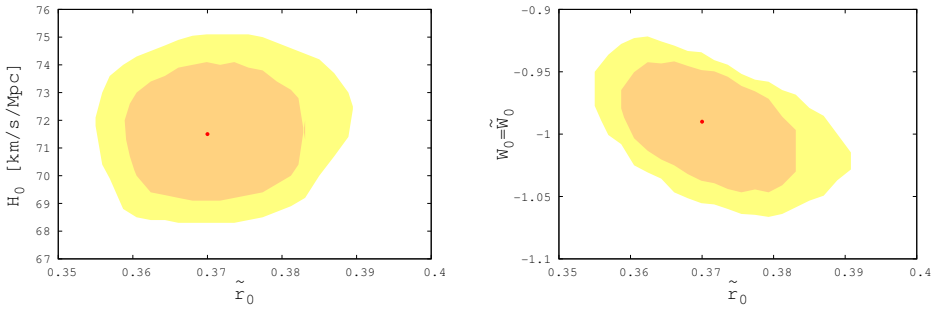

Figure 6.4: Left panel: the 1σ and 2σ confidence regions for the parameters $\tilde{r}_0$ and H_0 of model 2. Right panel: the same regions for the parameters w_0 (equivalent to $\tilde{w}_0$ and derived from $\epsilon = -3w_0$) and $\tilde{r}_0$. Notice that $\tilde{r}_0$ is the ratio of the energy densities just for the $\tilde{c}^2(t)$ (non-interacting) case; for the interacting case it has no staightforward physical meaning. Central dots indicates the best fit values.

6.6 Evolution of the subhorizon perturbations

We have seen that in model 1 (section 6.4), the interacting version is preferred over the non-interacting one because $\tilde{\Omega}_{M0} \approx 0.17$, too small as compared with results of Komatsu et *al.* [70]. In model 2 (section 6.5), both seem to be compatible with observations at the background level. A further

study should be done, in general, to establish which scenario is observationally favored. Here, we make a simple perturbation study, just considering matter perturbations inside the horizon. This study just intends to illustrate that a perturbative analysis can permit us tell apart the interacting from the non-interacting scenario, despite they share the same $H(z)$.

Once the Universe becomes matter dominated, the anisotropic stress due to neutrinos will be negligible and, in the Newtonian gauge, it will suffice just one single gravitational potential -say ϕ- to determine the flat metric element

$$ds^2 = -(1+2\phi)dt^2 + a^2(1-2\phi)dx^i dx_i. \tag{6.21}$$

In the interacting case, the energy-momentum tensors of dark matter and dark energy are not independently conserved. For the first component, by perturbing the conservation equation $T^{\mu\,\nu}_{M\ \ ;\mu} = Q^{\mu}_{M}$, where $Q^{\mu}_{M} \equiv Q u^{\mu}_{M}$ (with u^{μ}_{M} the four velocity of matter, and no momentum transfer in the cold dark matter reference rest frame is assumed) [50, 56], the equations of motion for the energy density and the velocity divergence ($\theta = ik^j v_j$) perturbations, with the speed of sound, $c^2_{s\,M} = 0$, and the EoS parameter, $w_M = 0$, are

$$\dot{\delta}_M = -\frac{\theta_M}{a} + 3\dot{\phi} + \frac{\delta Q}{\rho_M} + \frac{Q}{\rho_M}\left(\phi - \delta_M\right) , \tag{6.22}$$

$$\dot{\theta}_M = -H\theta_M + \frac{k^2}{a}\phi , \tag{6.23}$$

and for the dark energy component $T^{\mu\,\nu}_{X\ \ ;\mu} = Q^{\mu}_{X}$, where $Q^{\mu}_{X} \equiv -Q u^{\mu}_{M}$, and since dark energy can be considered a scalar field, the effective speed of sound $c^2_{s\,X} = 1$, the dynamical equations for perturbations become

$$\begin{aligned}\dot{\delta}_X = &-(1+w)\frac{\theta_X}{a} - 3H(1-w)\delta_X - 3aH\left[3H\left(1-w^2\right) + \dot{w}_X\right]\frac{\theta_X}{k^2} \\ &+3(1+w)\dot{\phi} - \frac{Q}{\rho_X}\left[\phi - \delta_X + 3aH(1-w)\frac{\theta_X}{k^2}\right] - \frac{\delta Q}{\rho_X} ,\end{aligned} \tag{6.24}$$

$$\dot{\theta}_X = 2H\theta_X + \frac{1}{(1+w)}\frac{k^2}{a}\delta_X - \frac{k^2}{a}\phi - \frac{Q}{(1+w)\rho_X}\left(\theta_M - 2\theta_X\right) , \tag{6.25}$$

while the Fourier transformed $0-0$ and $0-i$ components of the Einstein equations are

$$\frac{k^2}{a^2}\phi + 3H(\dot{\phi} + H\phi) = -4\pi G\sum_i \rho_i\,\delta_i , \tag{6.26}$$

$$\frac{k^2}{a}\left(\dot{\phi} + H\phi\right) = 4\pi G\sum_i (\rho_i + P_i)\,\theta_i . \tag{6.27}$$

A more detailed derivation of the perturbation equations can be found in [56]. As we are concerned with subhorizon scales we just consider the case in which $k \gg aH$, and so, the Newtonian limit of Poisson's equation (6.26) is just

$$\frac{k^2}{a^2}\phi = -4\pi G\left(\rho_M \delta_M + \rho_X \delta_X\right) \ . \tag{6.28}$$

From Eq.(6.28) and bearing in mind that every single energy component obeys $\frac{8\pi G}{3}\rho_i \leq H^2$, one sees that the gravitational potential (and its derivatives) can be neglected when compared with the density perturbations. After all this, Eqs. (6.22)-(6.25) simplify to

$$\dot{\delta}_M = -\frac{\theta_M}{a} \ , \tag{6.29}$$

$$\dot{\theta}_M = -H\theta_M + \frac{k^2}{a}\phi \ , \tag{6.30}$$

$$\dot{\delta}_X = -\left(1+w\right)\frac{\theta_X}{a} - 3H\left(1-w\right)\delta_X + \frac{1}{\rho_X}\left(Q\delta_X - \delta Q\right) \ , \tag{6.31}$$

$$\dot{\theta}_X = \frac{1}{\left(1+w\right)}\frac{k^2}{a}\delta_X - \frac{Q}{\left(1+w\right)\rho_X}\left(\theta_M - 2\theta_X\right) \ . \tag{6.32}$$

Notice that in the interacting version of model 1, $\delta Q = 3AH_0\rho_M\delta_M$, but in model 2, since Q includes a dependence in w and H, the analysis is more involved. However, we assume, as in [56], that the product $3c^2wH$ is just an approximation to a time (but not position) dependent interaction rate, so there are no perturbations there, and $\delta Q = -3c^2wH\rho_M\delta_M$. In the $\tilde{c}^2$ scenarios of both models, $Q = 0$ and $\delta Q = 0$.

6.6.1 Initial conditions

To solve numerically these four coupled differential equations, we must choose some initial conditions to the density and velocity perturbations. We set them at $z_i = 1000$. We impose the potential to be a constant (we have seen that it and its time derivative are much smaller than density perturbations), and using the perturbed Einstein equations (6.27) and (6.28), we find the density and velocity initial conditions

$$k^2\phi = -\frac{3}{2(1+z_i)^2}\left(\rho_{M\,i}\,\delta_M(z_i,k) + \rho_{X\,i}\,\delta_X(z_i,k)\right) \ , \tag{6.33}$$

$$k^2\phi = \frac{3}{2(1+z_i)H}\left(\rho_{M\,i}\,\theta_M(z_i,k) + \rho_{X\,i}\,\theta_X(z_i,k)\right) \ . \tag{6.34}$$

for each model. Since we obtain, numerically, that the evolution of perturbations is nearly independent of the wavenumber k in the range $0.001\ h\,Mpc^{-1} \leq k \leq 0.1\ h\,Mpc^{-1}$, that includes all the interesting scales under consideration, we shall assume that initially dark energy perturbations are proportional to the dark matter perturbations, i.e., $\delta_X(z_i,k) = \alpha\,\delta_M(z_i,k)$ and $\theta_X(z_i,k) = \beta\,\theta_M(z_i,k)$, with α a nonnegative constant.

Interacting version of model 1

We have the freedom to normalize the matter density contrast as $\delta_M(z_i) = \frac{1}{1+z_i}$, then by equations (6.27) and (6.28), we find $\theta_M(z_i) = -\left(\frac{1+\alpha\,\Omega_{X0}}{\Omega_{M0}+\beta\,\Omega_{X0}}\right)\frac{H}{(1+z_i)^2}$. For the dark energy component we take different choices for α and β. The dashed (green) lines of the left panel of figure 6.5 correspond to the non-interacting scenarios . Solid (blue) line is for the ΛCDM model, shown for illustration. Each different dashed (green) line depicts various initial conditions, from top to bottom, $\alpha = 0$ and $\beta = 0$, $\alpha = 1$ and $\beta = 1$, and $\alpha = 1$ and $\beta = 10$. Notice that the interacting scenarios exhibit a dependence on the initial conditions chosen for the dark energy component. The evolution of perturbations depend on the initial conditions on θ_X but not so much on δ_X.

$\tilde{c}^2$ version of model 1

For the matter component we impose as in the previous case $\delta_M(z_i) = \frac{1}{1+z_i}$ and find $\theta_M(z_i) = -\left(\frac{1+2\alpha\,A\,(1-A)\,(1+z)^{-\frac{3}{2}}}{1+2\beta\,A\,(1-A)\,(1+z)^{-\frac{3}{2}}}\right)\frac{H}{(1+z_i)^2}$. Left panel of figure 6.5 shows the evolution of δ_M, dot-dashed (red) lines, for different options for both $\delta_X(z_i)$ and $\theta_X(z_i)$. Each different dot-dashed (red) line depicts two initial conditions, $\alpha = 0$ and $\beta = 0$ and $\alpha = 1$ and $\beta = 10$ (they practically overlap). In this scenario, the final result does not depend on the chosen initial conditions.

Interacting version of model 2

For the matter component we obtain as in the previous section 6.6.1 $\delta_M(z_i) = \frac{1}{1+z_i}$ and $\theta_M(z_i) = -\left(\frac{1+\alpha\,\Omega_{X0}}{\Omega_{M0}+\beta\,\Omega_{X0}}\right)\frac{H}{(1+z_i)^2}$. For the dark energy component we take different options for both $\delta_X(z_i)$ and $\theta_X(z_i)$. The dashed (green) lines of the right panel of figure 6.5 correspond to the non-interacting scenario. Solid (blue) line is for the ΛCDM model, shown for comparison purposes. Each different dashed (green) line depicts, from top to bottom on

the right, $\alpha = 0$ and $\beta = 0$, $\alpha = 1$ and $\beta = 1$ and $\alpha = 1$ and $\beta = 10$. Notice that the interacting scenarios exhibit a dependence on the initial conditions chosen for the dark energy component.

$\tilde{c}^2$ version of model 2

For the matter component we find $\delta_M(z_i) = \frac{1}{1+z_i}$ and $\theta_M(z_i) = -\frac{H}{(1+z_i)^2}$. The right panel of figure 6.5, shows the evolution of δ_M, with dot-dashed (red) lines, for various options for both $\delta_X(z_i)$ and $\theta_X(z_i)$. Each different dot-dashed (red) line depicts the initial conditions, $\alpha = 0$ and $\beta = 0$, and $\alpha = 1$ and $\beta = 10$, though they practically overlap. Again, the final result does not depend on the initial conditions.

6.6.2 Results

Figure 6.5 shows the numerical solution for δ_M for model 1 (left panel), and for model 2 (right panel), in both cases for $k = 0.01\ h\,Mpc^{-1}$. However, the outcome is quite independent of the wavenumber k in the range $0.001\ h\,Mpc^{-1} \leq k \leq 0.1\ h\,Mpc^{-1}$ that includes all the interesting scales under consideration. In the interacting case, the matter density perturbations do not depend much on initial conditions imposed on the δ_X but they do on the initials conditions on θ_X. Notice that in any case, the matter density perturbations clearly differ in both scenarios, the interacting and the $\tilde{c}^2$ one. The most favored (the closer to ΛCDM), at least in the two models studied here, are the $\tilde{c}^2$ scenarios, since low density perturbations at $z \approx 10$ can be problematic for the large scale structure formation. To confront it with observations, we resort to the growth function, $f \equiv d\ln\delta_M/d\ln a$ [121], and the observational data borrowed from [117]. In figure 6.6, we can see that for both models (left panel model 1, right panel model 2) the non-interacting version fits better the data, as said before, especially at the present epoch. This approach was just done to show that interacting versions and $\tilde{c}^2$ sharing the same $H(z)$, and so indistinguishable at the background level, can evolve differently at the perturbative level. However, to definitively discard, or validate, the interacting model, an exact first order perturbation together with the study of matter and radiation power spectrum seems necessary.

6.7 Conclusions

As we have seen, at background level, holographic interacting models whose IR cutoff is set by the Hubble's length can be viewed as non-interacting ones

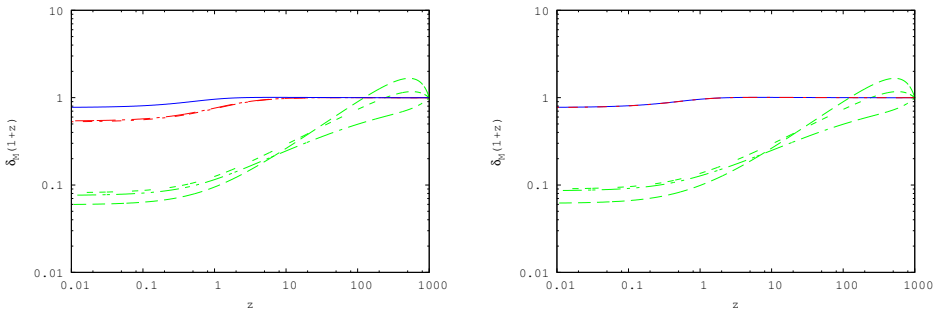

Figure 6.5: Left panel: the evolution of cold dark matter density perturbations versus redshift in model 1. Right panel: the same for model 2. In plotting the graphs the dashed (green) lines describe the matter density perturbations of the interacting scenario, the dot-dashed (red) lines the $\tilde{c}^2$, and the solid (blue) line ΛCDM for comparison purposes. Different initial conditions are used for the interacting versions; from top to bottom at the right, $\alpha = 0$ and $\beta = 0$, $\alpha = 1$ and $\beta = 1$ and $\alpha = 1$ and $\beta = 10$. For the $\tilde{c}^2$, two different sets of initial conditions are used, but the corresponding graphs practically overlap each other ($\alpha = 0$ and $\beta = 0$, and $\alpha = 1$ and $\beta = 10$). Notice that in the right panel, the $\tilde{c}^2$ scenario overlaps ΛCDM, as it behaves as a wCDM model with $w = 0.99$.

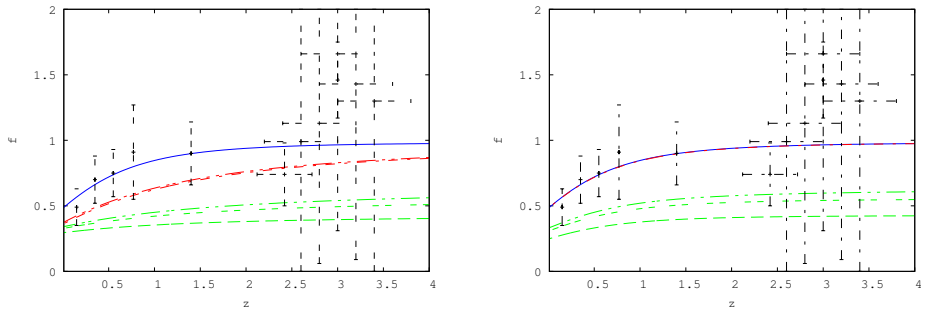

Figure 6.6: Left panel: the evolution of the growth function, $f \equiv \frac{d \ln \delta_M}{d \ln a}$, versus redshift for model 1. Right panel: the same for model 2. In plotting the graphs the dashed (green) lines describe the growth function of the interacting scenario, the dot-dashed (red) lines the $\tilde{c}^2$, and the solid (blue) line ΛCDM for comparison purposes. Different initial conditions are used for the interacting versions; from top to bottom $\alpha = 0$ and $\beta = 0$, $\alpha = 1$ and $\beta = 1$ and $\alpha = 1$ and $\beta = 10$. For the $\tilde{c}^2$, two different sets of initial conditions are used, but they practically overlap each other ($\alpha = 0$ and $\beta = 0$, and $\alpha = 1$ and $\beta = 10$). Notice that in the right panel, the $\tilde{c}^2$ scenario overlaps ΛCDM, as it behaves as a wCDM model with $w = -0.99$. Observational data is borrowed from [117].

whose holographic parameter $\tilde{c}^2$ is not constant but varies slowly. Because they share an identical Hubble function, they are not distinguishable at the background level. However, this degeneracy can be broken at the pertur-

bative level, since both energy components, i.e., cold dark matter and dark energy, evolve differently in each scenario. The interacting model and the non-interacting one (section 6.4) fit the geometrical data rather well. At the perturbative level, the non-interacting scenario is favored by large scale structure formation. In the second model (section 6.5), which behaves as a spatially flat wCDM model, both interpretations, interacting and $\tilde{c}^2(t)$, fit the data well and the values of the parameters seem reasonable. It contains the ΛCDM as a limiting case but with the coincidence problem alleviated in the interacting scenario. To discriminate between both interpretations, at the perturbative level, the non-interacting scenario appears favored. This should not be surprising, since it mimics rather well the ΛCDM model.
In general, the non-interacting versions seem to be favored by the structure formation, however, the interacting can not be ruled out just at this point. To go deeper in the matter, a full-fledged perturbative analysis seems necessary.

6.8 Hubble functions considering the radiation component

To constrain the model with CMB data, it is necessary to take into account the radiation component, since we need to describe the Universe at the last scattering surface, $z_\star \approx 1090$, where the said component is no longer negligible. So, expressions like (6.9) and (6.19) are not appropriate at the last scattering epoch, much less so at earlier times. The presence of radiation invalidates the expression $\rho_M = 3M_P^2(1-c^2)H^2$, so to obtain the Hubble function we rewrite the second Friedmann equation as

$$\frac{\dot{H}}{H^2} = -\frac{3}{2}\left(1 + w_X\Omega_X + w_R\Omega_R\right) , \tag{6.35}$$

where the subscript R stands for radiation, and the EoS parameter w_X does not coincide with the w of sections 6.4 and 6.5. Differentiating Eq.(2.45) and using Eqs. (6.3.2) and (6.35), we obtain

$$w_X = -\frac{Q}{(1-c^2)\rho_X H} + \frac{w_R}{c^2}\left(\frac{H_0}{H}\right)^2 \Omega_{R0}(1+z)^4 . \tag{6.36}$$

Because of this expression, Eq. (6.35) has no analytical solution. However, we can consider two different integration regions. One for $z \leq 50$ and another for $z \geq 50$. In the former, the universe is cold dark matter and dark

energy dominated; in the latter only the higher z terms contribute.

In the example considered in section 6.4, $Q \equiv \Gamma\rho_X$ and in the first integration region, $z \leq 50$, the second term in Eq. (6.36) contributes less than 1%, so the Hubble parameter is just like in Eq. (6.9), and the first Friedmann equation come very close to

$$\left(\frac{H}{H_0}\right)^2_{z\leq 50} \simeq A^2 + 2A(1-A)(1+z)^{\frac{3}{2}} + (1-A)^2(1+z)^3\,. \tag{6.37}$$

For the second region, $z \geq 50$, the first term in Eq. (6.36) contributes no more than 1%, so the first Friedman equation can be approximated by

$$\left(\frac{H}{H_0}\right)^2_{z\geq 50} \simeq (1-A)^2(1+z)^3 + 2\Omega_{R0}(1+z)^4\,. \tag{6.38}$$

As the two first terms in Eq. (6.37) are negligible in the region $z \geq 50$, and the second term in Eq. (6.38) is trifling when $z \geq 50$, we can just consider the Hubble function, after redefining $2\Omega_{R0} \to \Omega_{R0}$ (notice that with this we assume that what is holographic is the total energy density, and not only dark energy), as

$$\left(\frac{H}{H_0}\right)^2 \simeq \left(A + (1-A)^2(1+z)^{\frac{3}{2}}\right)^2 + \Omega_{R0}(1+z)^4\,. \tag{6.39}$$

This Hubble function is the same in both scenarios, the interacting and the $\tilde{c}^2$, as when we ignored the radiation component.
Proceeding as before, in the case of the model 2 (§6.5) we obtain

$$\left(\frac{H}{H_0}\right)^2 \simeq \tilde{\Omega}_{M0}(1+z)^3 + \tilde{\Omega}_{X0}(1+z)^{3-\gamma} + \Omega_{R0}(1+z)^4\,. \tag{6.40}$$

In both cases, $\Omega_{R0} \approx \Omega_{\gamma 0}(1+0.0227N_{eff})$ as described in [70], where $N_{eff} = 3.04$ is the effective number of neutrino families.

6.9 Lagrangian formulation of the models of sec. 6.4

6.9.1 Interacting model with 1 scalar field

In §6.1, we have seen that this kind of interacting models, can be described as a single fluid (as long as the evolution of the densities of dark energy and

cold dark matter are identical), whose effective EoS parameter is

$$w_{eff} = -A\frac{H_0}{H} \quad , \tag{6.41}$$

with A a positive constant. The total effective pressure $P = w_{eff}\rho$ is

$$P \;\; = \;\; -3^{\frac{1}{2}} A\, M_P\, H_0\, \rho^{\frac{1}{2}} \, , \tag{6.42}$$

where P and $\rho \equiv \rho_M + \rho_X$ are the dark sector pressure and energy density from Eqs. (2.17) and (6.41). For a standard scalar field ϕ_Q minimally coupled to gravity, the action is defined by

$$S = \int d^4x\sqrt{-g}\left(\frac{R}{2} + L_Q(\phi_Q, \chi_Q)\right) \tag{6.43}$$

where $\chi_Q = \frac{1}{2}g_{\mu\nu}\partial^\mu\phi_Q\partial^\nu\phi_Q$ is the kinetic term. Assuming homogeneity and isotropy, the energy (Hamiltonian) density and the pressure (Lagrangian density) are

$$\rho = \frac{1}{2}\dot{\phi}_Q^2 + V(\phi_Q) \qquad \text{and} \qquad P = \frac{1}{2}\dot{\phi}_Q^2 - V(\phi_Q)\,. \tag{6.44}$$

From the last two equations the potential and the kinetic term are

$$\dot{\phi}_Q^2 = \rho + P \qquad \text{and} \qquad V(\phi_Q) = \frac{1}{2}\left(\rho - P\right) , \tag{6.45}$$

respectively. Using again Eqs.(2.17), (6.9) and (6.42) we obtain $P(z)$ and with (6.45) we obtain

$$d\phi_Q = \frac{2}{3AH_0}\left(\frac{P^2}{3A^2M_P^2H_0^2} + P\right)^{-\frac{1}{2}} dP\,. \tag{6.46}$$

After integration we get

$$L = P = -\frac{3A^2M_P^2H_0^2}{16}\left(4e^{-\frac{1}{4}\sqrt{\frac{3}{M_P^2}}\left(\phi_Q - \phi_{Q\,0}\right)} + e^{\frac{1}{4}\sqrt{\frac{3}{M_P^2}}\left(\phi_Q - \phi_{Q\,0}\right)}\right)^2 , \tag{6.47}$$

where we have defined $\phi_{Q\,0}$ as the value of the scalar field at the maximum pressure, i.e., when $z \to -1$. It is interesting to notice that in the absence

of interaction, $A = 0$, the pressure of the dark sector is that of cold matter. From (6.47) and (6.45) we find the potential

$$V(\phi_Q) = \frac{3A^2 M_P^2 H_0^2}{512}\left(4 + e^{\frac{1}{2}\sqrt{\frac{3}{M_P^2}}(\phi_Q - \phi_{Q\,0})}\right)^2 \times \left(16e^{-\sqrt{\frac{3}{M_P^2}}(\phi_Q - \phi_{Q\,0})} + 24e^{-\frac{1}{2}\sqrt{\frac{3}{M_P^2}}(\phi_Q - \phi_{Q\,0})} + 1\right). \quad (6.48)$$

So we can describe the whole dark sector by a standard scalar field, with an effective sound speed $c_s^2 = \frac{\delta P}{\delta \rho} = 1$, even if its adiabatic sound speed $c_a^2 = \frac{\dot{P}}{\dot{\rho}}$ is negative due to the interaction. Had we considered a general k-essence Lagrangian density [122], the squared sound speed would have been negative.

6.9.2 $\tilde{c}^2(t)$ model with 1 scalar field

Here we obtain a Lagrangian density for the dark energy in the case of the holographic $\tilde{c}^2$ model. This is motivated in order to show that the two models of section 6.4, described at the background level by the same $H(z)$, differ not only because the energy densities evolve differently but also because their Lagrangians are diverse.
To begin with, the dark energy density can be expressed as a function of the pressure

$$\tilde{\rho} = -3A^2 H_0^2 M_P^2 - 2\tilde{P}\,. \quad (6.49)$$

Proceeding as before we obtain

$$\tilde{L} = -3A^2 M_P^2 H_0^2 \sec^2\left(\sqrt{\frac{3}{M_P^2}}\frac{\tilde{\phi}_Q - \tilde{\phi}_{Q\,0}}{4}\right) \text{ and} \quad (6.50)$$

$$\tilde{V}(\tilde{\phi}_Q) = \frac{3A^2 M_P^2 H_0^2}{2}\tan^2\left(\sqrt{\frac{3}{M_P^2}}\frac{\tilde{\phi}_Q - \tilde{\phi}_{Q\,0}}{4}\right). \quad (6.51)$$

As in the previous case, for a k-essence Lagrangian we would have obtained $\tilde{c}_s^2 < 0$.

Chapter 7

Model of interacting holographic dark energy at the Ricci scale[1]

7.1 The holographic model

This model assumes a spatially flat homogeneous and isotropic universe dominated by dark matter and dark energy, the latter obeying the holographic relationship (2.45). In virtue of Friedmann equations,

$$H^2 = \frac{1}{3} M_P^{-2} (\rho_M + \rho_X) \,, \tag{7.1}$$

and

$$\dot{H} = -\frac{1}{2} M_P^{-2} (\rho_M + \rho_X + p_X) \,, \tag{7.2}$$

the fractional dark energy density, Ω_X, can be expressed as

$$\Omega_X = \frac{c^2}{3c^2 w + 2} \,, \tag{7.3}$$

where w, in general depends on time. The deceleration parameter (2.19) takes the simple expression,

$$q = 1 - \frac{\Omega_X}{c^2} \,. \tag{7.4}$$

As we shall see, as a consequence of the evolution of Ω_X, q varies monotonically from positive values at early times (in the matter dominated era)

[1] This Chapter corresponds to the model of Ref. [39].

to negative values at later times (in the dark energy dominated era). The evolution of Ω_X follows from the conservation equations of both dark components. In the absence of non-gravitational interactions between them they evolve independently and obey

$$\dot{\Omega}_M - \left(1 - \frac{2\Omega_X}{c^2}\right)(1-\Omega_X)\,H = 0\,, \tag{7.5}$$

$$\dot{\Omega}_X + \left(1 - \frac{2\Omega_X}{c^2}\right)(1-\Omega_X)\,H = 0\,. \tag{7.6}$$

Bearing in mind that in our case $\Omega_M + \Omega_X = 1$, we get the following expressions in terms of the redshift ,

$$\Omega_X = \frac{2\Omega_{X0} - c^2 + c^2(1-\Omega_{X0})(1+z)^{\frac{2}{c^2}-1}}{2\Omega_{X0} - c^2 + 2(1-\Omega_{X0})(1+z)^{\frac{2}{c^2}-1}}\,. \tag{7.7}$$

The coincidence problem gets alleviated if for reasonable values of Ω_{X0} and c^2 we get $r_0 \sim \mathcal{O}(1)$. This is the case here since for Ω_{X0} and c^2 of order unity, r_0 also results of this same order. Here, again, $r = \rho_M/\rho_X$. However, for late times (i.e, when $z \to -1$) one has $r \to 0$. In this sense, the coincidence problem is not properly solved. To obtain a non-vanishing ratio at late times some interaction between DM and DE must be incorporated in the picture [104].

In this case, the evolution equations generalize to

$$\dot{\Omega}_M - \left(1 - \frac{2\Omega_X}{c^2}\right)(1-\Omega_X)\,H = QH\,, \tag{7.8}$$

$$\dot{\Omega}_X + \left(1 - \frac{2\Omega_X}{c^2}\right)(1-\Omega_X)\,H = -QH\,, \tag{7.9}$$

where the Hubble factor on the right hand sides has been introduced to render the interaction term, Q, dimensionless.

Since the nature of both dark components is largely unknown, there is ample latitude in choosing Q. We shall specify it by demanding that r evolves from an unstable fixed point in the far past, $r_\infty \equiv r(z \to \infty)$, to a stable fixed point at the far future, $r_f \equiv r(z \to -1)$ [104]. The pair of equations (7.8) and (7.9) imply

$$\dot{r} = \left[r\left(1 + r - \frac{2}{c^2}\right) + Q(1+r)^2\right]H\,. \tag{7.10}$$

Imposing that r_f be a fixed point, i.e., $\dot{r}|_{r=r_f} = 0$ the interaction term Q is simply a constant given by

$$Q = -\frac{r_f}{(1+r_f)^2}\left(1 + r_f - \frac{2}{c^2}\right). \tag{7.11}$$

As we shall see later, r_f and c^2 take values such that Q is positive-definite, which entails a transfer of energy from dark energy to dark matter. Obviously if Q were negative, the transfer of energy would go in the opposite direction which would conflict with the second law of thermodynamics [123] and the coincidence problem would only worsen. Rewriting Eq. (7.10) as

$$\dot{r} = (Q+1)(r - r_f)(r - r_\infty)H \tag{7.12}$$

and using the condition $\dot{r} = 0$, the other fixed point can be expressed in terms of the previous one, namely,

$$r_\infty = \frac{2 - c^2(1+r_f)}{2r_f + c^2(1+r_f)}. \tag{7.13}$$

To study the stability of the fixed points we first write $r' \equiv dr/d\ln a = \dot{r}/H$ and calculate the derivative of r' with respect to r. In the case of the far future fixed point we get

$$\frac{dr'}{dr}|_{r_f} = 1 + \frac{2(r_f - 1)}{c^2(r_f + 1)}. \tag{7.14}$$

Since r_f must be lower than $r_0 \simeq 0.45$, from Eq. (7.4) with $c^2 < \Omega_{X0} \simeq 0.75$ (otherwise q_0 would not be negative), one follows that $\frac{dr'}{dr}|_{r_f} < 0$, i.e., the fixed point r_f is a stable one. Similarly, we find that

$$\frac{dr'}{dr}|_{r_\infty} = -\frac{2+c^2}{c^2} + \frac{4}{c^2(1+r_f)} > 0\,, \tag{7.15}$$

i.e., the fixed point at the far past is an unstable one. Equation (7.12) can be integrated with the help of (7.11). In terms of the redshift it yields,

$$r = \frac{r_f(r_0 - r_\infty) - r_\infty(r_0 - r_f)(1+z)^{(Q+1)(r_\infty - r_f)}}{(r_0 - r_\infty) - (r_0 - r_f)(1+z)^{(Q+1)(r_\infty - r_f)}}. \tag{7.16}$$

Inspection of (7.12) readily shows that when r lies between both fixed points one has $\dot{r} < 0$, i.e., the ratio between the energy densities diminishes monotonously from one fixed point to the other. This is depicted in Fig. 7.1.

The said ratio smoothly decreases from high z (i.e., from r_∞ -the unstable fixed point is at $z \to \infty$)) to asymptotically approach the fixed stable point, r_f, at $z = -1$. Note that the latter needs not be zero. In this regard the coincidence problem is much alleviated because we are not living in any special era. However, the problem is not solved in full since the model cannot predict that r_0 is of order unity. To the best of our knowledge, no model predicts this value, as well as no model predicts the present value of the temperature of the cosmic background radiation, the Hubble constant, or the age of the Universe. For the time being, we must content ourselves by taking these values as input parameters since, very possibly, we are to wait for a successful theory of quantum gravity to compute them. The expression for the fractional density of dark energy follows from the relationship $r = (1 - \Omega_X)/\Omega_X$ and Eq. (7.16),

$$\Omega_X = \frac{(r_0 - r_\infty) - (r_0 - r_f)(1+z)^{(Q+1)(r_\infty - r_f)}}{(r_f + 1)(r_0 - r_\infty) - (r_\infty + 1)(r_0 - r_f)(1+z)^{(Q+1)(r_\infty - r_f)}} \,. \quad (7.17)$$

From the latter and (7.3) we obtain the equation of state of dark energy in

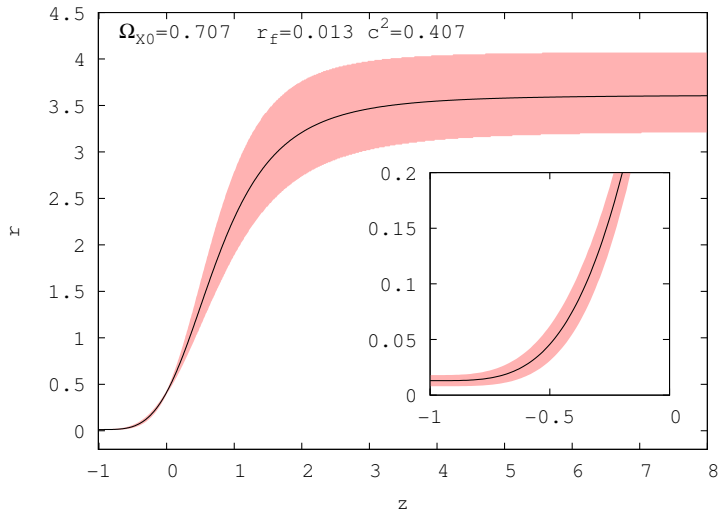

Figure 7.1: The ratio r between the energy densities vs. redshift for the best fit model. As the inset shows $r_f \equiv r(z \to -1)$ does not vanish. In this, as well as in subsequent figures, the red swath indicates the region obtained by including the 1σ uncertainties of the constrained parameters used in the calculation.

terms of the redshift,

$$w = \frac{1}{3}\left(1 - \frac{2}{c^2} + r_\infty + \frac{(r_0 - r_\infty)(r_\infty - r_f)}{r_\infty - r_0 + (r_0 - r_f)(1+z)^{(Q+1)(r_\infty - r_f)}}\right) . \quad (7.18)$$

As shown in the left panel of Fig. 7.2 for the best fit model, w smoothly evolves from a negative value close to zero at high redshifts to a value lower than -1 at the far future. The right panel depicts its evolution near the present time ($z = 0$) showing compatibility with recent observational data which suggest that w does not depart much from -1 at sufficiently low redshifts (see [107]). Integration of the second Friedmann's equation (7.2)

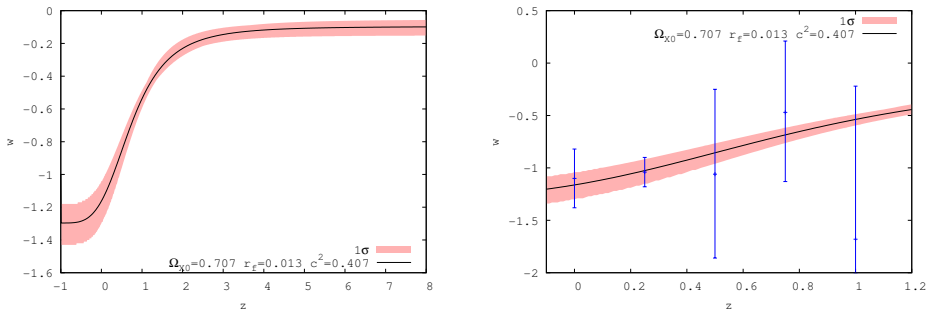

Figure 7.2: The equation of state parameter (as given by Eq. (7.18)) vs. redshift up to $z = 8$ (left panel), and up to $z = 1.2$ only (right panel) for the best fit holographic model. At high redshifts w approaches the equation of state of non-relativistic matter and at low redshifts it does not depart significantly from -1. The observational data are taken from [107]; each error bar signifies a 2σ uncertainty.

provides us with the evolution equation for the Hubble factor which is key to perform the statistical analysis of section 7.3,

$$H = H_0 \left[\frac{A_1 + 2\left(A_2 + (r_f - r_0)(1+z)^{-A_3}\right)}{A_4}\right]^{1/2} (1+z)^{A_5} , \quad (7.19)$$

where

$$A_1 = c^2(1+r_f)(1+r_0) , \quad A_2 = r_0 r_f - 1 , \quad A_3 = 1 + \frac{2(r_f - 1)}{c^2(1+r_f)} ,$$

$$A_4 = [c^2(1+r_f) + 2(r_f - 1)](1+r_0) , \quad A_5 = 2 - \frac{1}{c^2(1+r_f)} .$$

Figure 7.3 depicts the evolution of the deceleration parameter, Eq. (7.4), for the best fit model. The observational data are borrowed from [108]. The redshift at which the universe starts accelerating is $z(q = 0) = 0.56^{+0.12}_{-0.9}$ while for the ΛCDM model $z(q = 0) = 0.79 \pm 0.02$. As mentioned before,

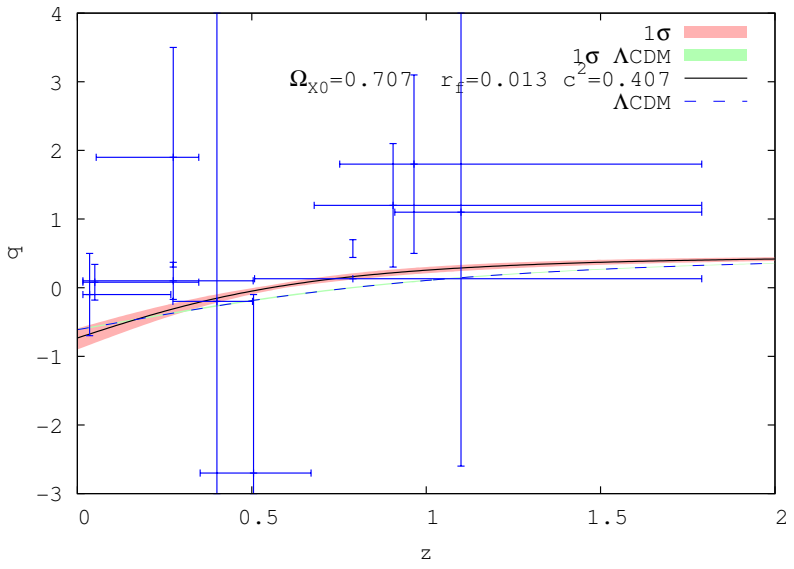

Figure 7.3: The deceleration parameter vs. redshift for the best fit holographic model (solid line) and the ΛCDM model (dashed line). In this, as well as in subsequent figures, the green swath indicates the region obtained by including the 1σ uncertainties of the constrained parameters used in the calculation (in the present case just Ω_{M0}). The observational data are taken from [108]; however, in view of the large error bars we do not use these data to fit the models.

there is ample freedom in the choice of the interaction term Q. In a previous paper [99], on a holographic dark energy model with the Hubble rate as infrared cutoff, we took $Q \propto \Omega_X$ [99]. We do not pursue this possibility here because, as we have checked, it leads to a universe in which dark energy is subdominant at very late times. While this does not contradict observation, it looks a bit odd. In any case, it deserves a separate study which lies beyond the scope of this Memoir.

7.1.1 Age problem

As noted in §5.1, some cosmological models suffer from the so-called "age problem", namely, the existence of high redshifts objects whose age at some redshift seem to exceed the Universe's age predicted at that redshift (as in the ΛCDM model, see e.g. [113]).

The age of the Universe at redshift z is

$$t(z) = t_0 - \int_0^z \frac{dz'}{(1+z')\,H(z')}\,. \tag{7.20}$$

Figure 7.4 shows the latter as a function of redshift for the best fit holographic model and the ΛCDM. Also marked in the figure are the ages and redshifts of the three luminous old objects. As is apparent, the ages of two old objects result compatible with both, the holographic and the ΛCDM model; however, the age of the old quasar falls only within 2σ with the ages predicted by these two models. Thus, some tension exists in this regard. By contrast, the interacting holographic model of Ref. [99], which takes as infrared cutoff the Hubble radius, is free of the problem. At any rate, it remains to be seen in which direction (if any) future observations will "move" the age of the said quasar.

7.2 Discussion of the cosmic coincidence

In holographic models of dark energy that take the Ricci's length as the infrared cutoff one can obtain a finite and approximate constant ratio r for an ample redshift span even if no interaction between the dark components is assumed -see e.g. [36]. Here we analyze how this comes about, and we note that while this approach alleviates the coincidence problem it does so only partially since it would entail somehow that we are living in a special time.

We start by rewriting Friedmann's equation (7.1) with the help of the saturated holographic bound, $\rho_X = 3M_P^2c^2\,(\dot{H}+2H^2)$, as

$$3H^2 = 3c^2(\dot{H}+2H^2) + \frac{\rho_{M0}}{M_P^2}\,(1+z)^3\,, \tag{7.21}$$

and, for convenience, introduce the ancillary variable $y^{-\alpha} = 1+z$. Thus, Eq. (7.21) takes the form

$$3\alpha^2\frac{\dot{y}^2}{y^2} = 3c^2\left\{\alpha\left[\frac{\ddot{y}}{y} - \frac{\dot{y}^2}{y^2}\right] + 2\alpha^2\frac{\dot{y}^2}{y^2}\right\} + \frac{\rho_{M0}}{M_P^2}\,y^{-3\alpha}\,. \tag{7.22}$$

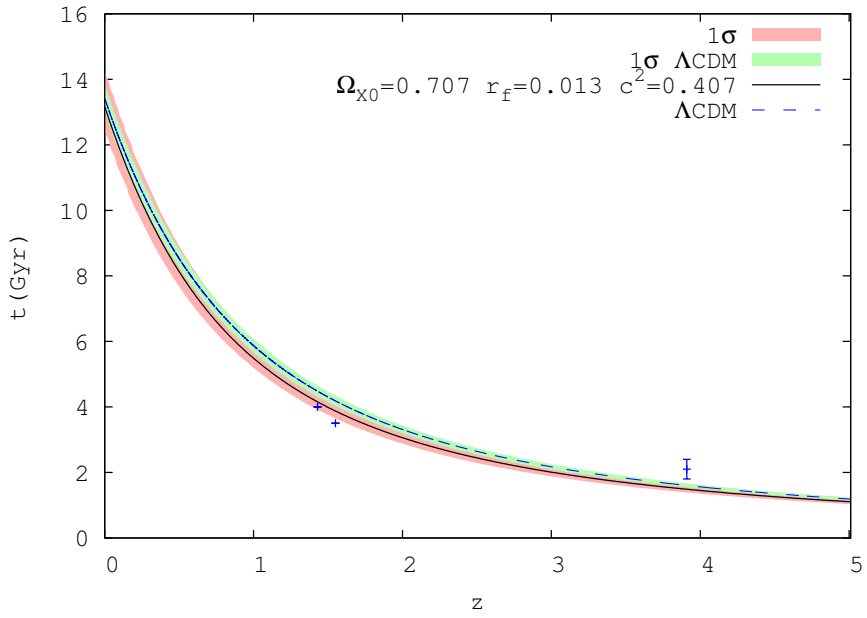

Figure 7.4: Age of the Universe, t vs. redshift. The solid line corresponds to the best fit holographic model and the dashed line to the ΛCDM model. The data points from left to right locate the old objects LBDS 53W069, LBDS 53W091 and APM 08279+5255.

By equating coefficients, we get $\alpha = c^2/(2c^2 - 1)$, and

$$\ddot{y} + \frac{\rho_{M0}}{3c^2 M_P^2\, \alpha} y^{-3\alpha+1} = 0\,. \tag{7.23}$$

Multiplying the latter by $\dot{y}$ the differential equation can be readily solved. Upon reverting to the original variable we obtain

$$3H^2 = \frac{2}{(2-c^2)M_P^2}\rho_{M0}(1+z)^3 + \beta\, M_P^{-2}\rho_{M0}(1+z)^{2\frac{1-2c^2}{c^2}}\,, \tag{7.24}$$

where β is a positive-definite integration constant that can be identified as $\beta = \left(\frac{1}{r_0} - \frac{c^2}{2-c^2}\right)$ and, of the order of unity since r_0 and c^2 lie not far from 0.4.

Recalling Eq. (7.1) we finally get

$$\rho_X = \frac{c^2}{2-c^2}\rho_{M0}(1+z)^3 + \beta\,\rho_{M0}\,(1+z)^{2\frac{1-2c^2}{c^2}}\,. \tag{7.25}$$

The dark energy density is contributed by two terms. The first one redshifts exactly as non-relativistic matter. The second one, in view that c^2 is bounded by $0.36 < c^2 < 0.8$, results subdominant for z of order of unity and larger. Therefore, we can safely conclude that $r = \rho_M/\rho_X \simeq (2 - c^2)/c^2$ for $0 \leq z$. This is why the ratio r results of order unity in an ample redshift interval, also in the absence of interaction, as in Ref. [36]. However, in view of the observational lower bound on c^2, we see that $r \to 0$ as $z \to -1$. So, in the holographic non-interacting model, r results well below unity, close to zero, and approaches this null value asymptotically for an infinite span of time. Altogether, according to this model, we live in a special and transient period in which r results comparable to unity.

7.3 Observational constraints

To constrain the four free parameters (Ω_{X0}, c^2, r_f, and H_0) of the holographic model presented above we use observational data from SN Ia (557 data points), the CMB-shift, BAO, and gas mass fractions in galaxy clusters as inferred from X-ray data (42 data points), the Hubble rate (15 data points), and the growth function (5 data points). Being the likelihood function defined as $\mathcal{L} \propto \exp(-\chi^2/2)$ the best fit follows from minimizing the sum $\chi^2_{\rm total} = \chi^2_{sn} + \chi^2_{cmb} + \chi^2_{bao} + \chi^2_{X-rays} + \chi^2_{Hubble} + \chi^2_{gf}$.

7.3.1 SN Ia

We proceed as in §5.2.1 to obtain $\tilde{\chi}^2_{sn} = \chi^{2\,(minimum)}_{sn} = 543.70$.

7.3.2 CMB-shift

Minimization of the CMB-shift

$$\chi^2_{cmb}(\mathbf{p}) = \frac{(\mathcal{R}_{th} - \mathcal{R}_{obs})^2}{\sigma^2_{\mathcal{R}}} \tag{7.26}$$

produces $\chi^{2\,(minimum)}_{CMB-shift} = 0.013$.

7.3.3 BAO

Using data from SDSS and 2dFGRS as in §5.2.3, the best fit value for the holographic model is $D_v(0.35)/D_v(0.2) = 1.664 \pm 0.003$, and minimization of

$$\chi^2_{bao}(\mathbf{p}) = \frac{([D_v(0.35)/D_v(0.2)]_{th} - [D_v(0.35)/D_v(0.2)]_{obs})^2}{\sigma^2_{D_v(0.35)/D_v(0.2)}} \tag{7.27}$$

gives $\chi^{2\,(minimum)}_{bao} = 1.20$.

7.3.4 Gas mass fraction

To fit the model we go forward as in §5.2.4 to get $\chi^{2\,(minimum)}_{X-rays} = 41.79$. Figure 7.5 shows the fit to the data.

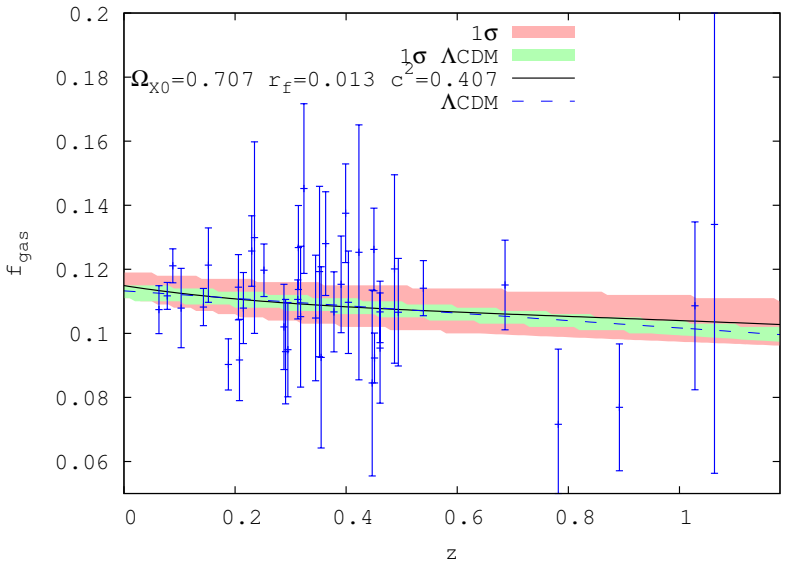

Figure 7.5: Gas mass fraction in 42 relaxed galaxy clusters vs. redshift. The solid and dashed curves correspond to the best fit models: holographic and ΛCDM, respectively. The data points with their error bars are taken from Table III of Ref. [94].

7.3.5 History of the Hubble parameter

By minimizing

$$\chi^2_{Hubble}(\mathbf{p}) = \sum_{i=1}^{15} \frac{[H_{th}(z_i) - H_{obs}(z_i)]^2}{\sigma^2(z_i)} \tag{7.28}$$

we got $\chi^{2\,(minimum)}_{Hubble} = 9.57$ and $H_0 = 71.8 \pm 2.9$ km/s/Mpc as the best fit for the Hubble's constant. Figure 7.6 depicts the Hubble history according to the best fit holographic model and the best ΛCDM model. The data used are explained in §4.6.

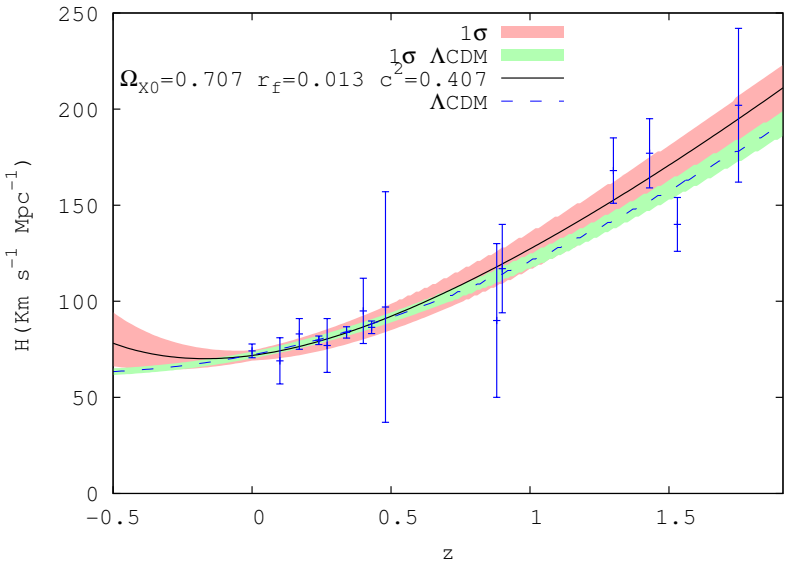

Figure 7.6: History of the Hubble factor in terms of the redshift for the best fit values of the holographic model (solid line) and the ΛCDM model (dashed line). The data points and error bars are borrowed from Refs. [95]-[98].

7.3.6 Growth function

As said above, background quantities that chiefly depend on $H(z)$ are not very useful at discriminating between cosmological models that present a similar Hubble history, independently of how different they might be. One

manner to circumvent this hurdle is to study evolution of the growth function (see §5.3). The evolution of the latter obeys the coupled set of equations

$$\dot{\delta}_M - \frac{k^2}{a^2} v_M = -\frac{1+r}{r} Q\, H\, \delta_M \,, \tag{7.29}$$

$$\dot{v}_M + H v_M + \frac{1}{a}\phi = 0 \,, \tag{7.30}$$

where the Newtonian potential ϕ fulfills Poisson's equation

$$\frac{k^2}{a^2}\phi = -4\pi G \rho_M \delta_M \,. \tag{7.31}$$

Solving the equations, and expressing in terms of r and using $w = [c^2(1+r) - 2]/(3c^2)$ obtained from (7.3), $c^{-2}(1+r)^{-1} = (\dot{H}/H^2) + 2$, and (7.10), from the evolution equations (7.8) and (7.9) one follows

$$f' + f^2 + \left(\frac{1}{c^2(1+r)} + Q\frac{1+r}{r} \right) f - \frac{3r^3 + 2Q^2(1+r)^3 - 2Qr(2+r-r^2)}{2r^2(1+r)} = 0 \,, \tag{7.32}$$

where $f' \equiv df/d\ln a$. Note that in the limit $Q \to 0$, last equation collapses to the corresponding expression of the Einstein-de Sitter scenario ($\Omega_M(z) = 1$ and $\delta_M \propto a \propto t^{2/3}$); that is to say, $f' + f^2 + [2 + (\dot{H}/H^2)]f = 3\Omega_M/2$. (Recall that for the Einstein-de Sitter model $\dot{H}/H^2 = -3/2$ and the solution of the equation for f is simply $f = 1$). In constraining the model we have taken only the five lowest redshift data of the growth function shown in Fig. 7.7 -the other data present very large error bars. The best fit yields $\chi^2 = 1.06$.

Figures 7.8 - 7.10 and table 7.1 summarize our findings. Figure 7.10 depicts the 1σ confidence contours from SN Ia (dashed yellow), CMB-shift (solid black), BAO (dashed blue), X-rays (dashed black), history of the Hubble function (dot-dot dashed green), and grow function (dot-dashed red) in the (Ω_{X0}, c^2) plane (left panel) and the (Ω_{X0}, r_f) plane. The joined constraints corresponding to χ^2_{total} are shown as shaded contours. As is apparent from left panel most of the discriminatory power arises from the near orthogonality between the X-ray and CMB-shift and supernovae contours. However, in the right panel the supernovae contour appears nearly degenerated with respect to the X-ray contour. Altogether, by constraining the holographic model of §7.1 with data from SN Ia, CMB-shif, BAO, X-rays, H(z), and the growth function we obtain $\Omega_{X0} = 0.707 \pm 0.009$, $c^2 = 0.407^{+0.033}_{-0.028}$,

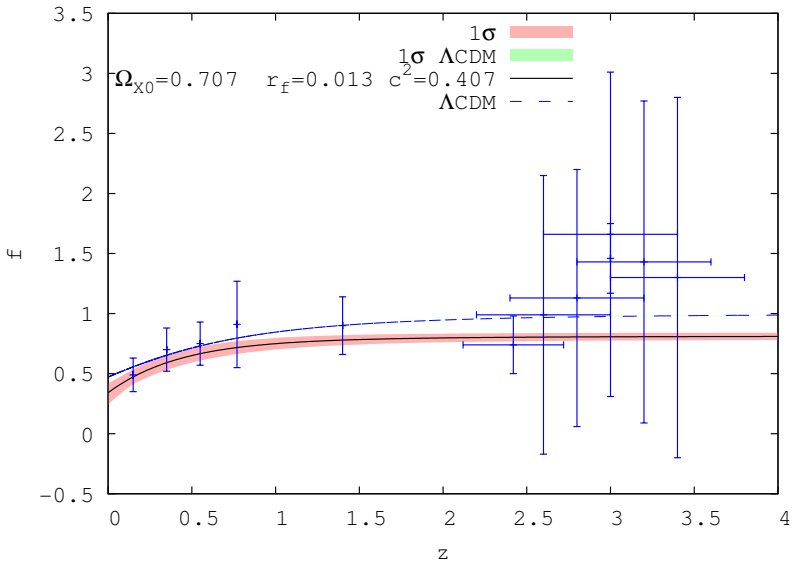

Figure 7.7: Growth function, f, vs. redshift as follows from integrating Eq. (7.32)(solid line). Also shown is the prediction of the ΛCDM model (dashed line). The observational data were taken from Ref. [117]. In constraining both models we have used only the five less noisy data depicted in the figure, (i.e., data corresponding to redshifts below 1.5).

$r_f = 0.013^{+0.006}_{-0.005}$, and $H_0 = 71.8 \pm 2.9$ km/s/Mpc as best fit parameters. It is worth noticing that the non-interacting case, $Q = 0$ (which implies $r_f = 0$ via Eq. (7.11)), lies over 2σ away from the best fit value. This feature seems typical of holographic dark energy models (see e.g. [36, 38, 99]).

Table 7.1 shows the partial, total, and total χ^2 over the number of degrees of freedom of the holographic model along with the corresponding values for the ΛCDM model. In the latter one has just two free parameters, Ω_{M0} and H_0. Their best fit values after constraining the model to the data are $\Omega_{M0} = 0.266 \pm 0.006$, and $H_0 = 71.8 \pm 1.9\,\mathrm{km/s/Mpc}$.

Although the ΛCDM model fits the data somewhat better, $\Delta\chi^2 \simeq 2.5$, than the holographic model, that has two more free parameters, it its uncertain which model should be preferred in view that the former cannot address the cosmic coincidence problem and the latter substantially alleviates it. More abundant and accurate data, especially at redshifts between the supernovae range and the CMB, will help decide the issue. Nonetheless,

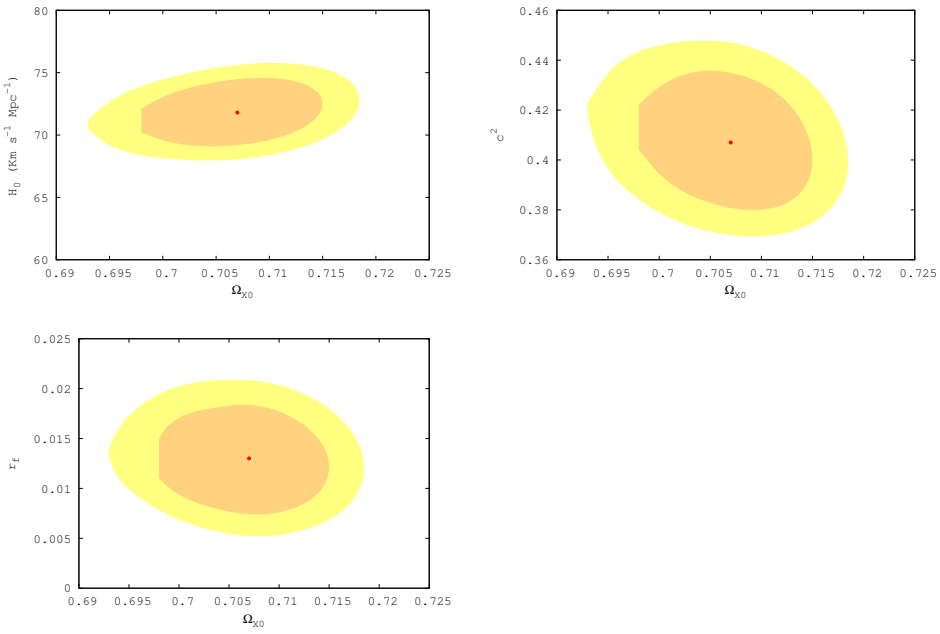

Figure 7.8: Panels from left to right, and top to bottom, show the 68.3% and 95.4% confidence contours for the pair of free parameters (Ω_{X0}, H_0), (Ω_{X0}, c^2), (Ω_{X0}, r_f), respectively, obtained by constraining the holographic model with SN Ia+CMB-shift+ BAO+X-ray+H(z)+growth function data. The solid point in each panel locates the best fit values.

we believe that the uncertainty will likely persists till a breakthrough on the theoretical side allows us to calculate with confidence the true value of the cosmological constant.

7.4 Concluding remarks

We performed a statistical study of the best fit parameters of the holographic model -presented in §7.1- using data from SN Ia, CMB-shift, BAO, X-ray, the Hubble history, and the growth function; 621 data in total. The maximum likelihood (or minimum χ^2) parameters are $\Omega_{X0} = 0.707 \pm 0.009$, $c^2 = 0.407^{+0.033}_{-0.028}$, $r_f = 0.013^{+0.006}_{-0.005}$, and $H_0 = 71.8 \pm 2.9$ km/s/Mpc with $\chi^2_{dof} \approx 0.96$. The Ω_{X0} and H_0 values fall within 1σ of the corresponding values determined by Komatsu *et al.* [124] (0.734 ± 0.029 and 71.0 ± 2.5

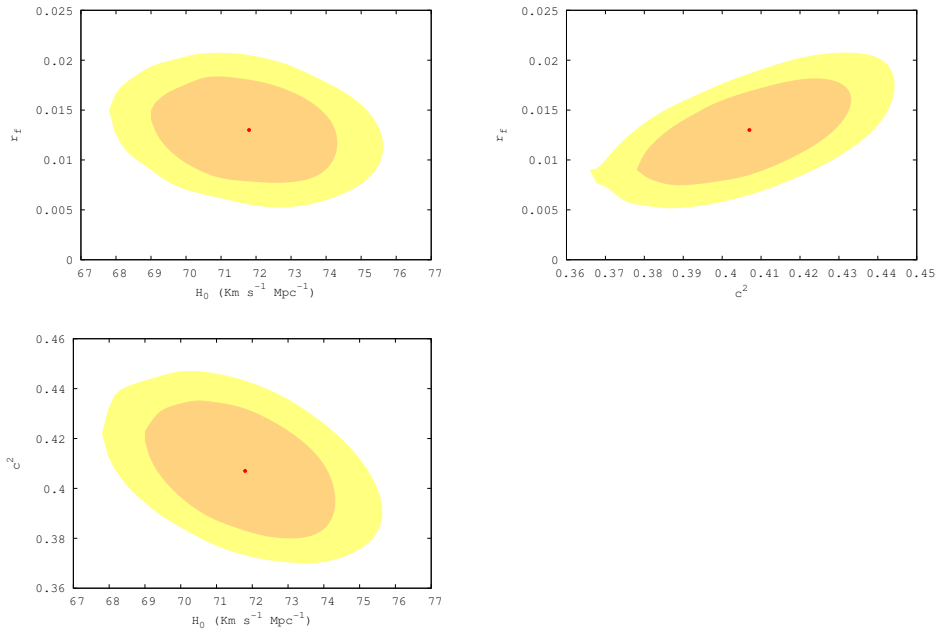

Figure 7.9: Same as Fig. 7.8 for the pairs of free parameters (H_0, r_f), (c^2, r_f), and (H_0, c^2).

km/s/Mpc, respectively). The evolution of the equation of state parameter, w, at redshift below 1.2 (see right panel of Fig. 7.2) is compatible with the observational constraints derived in [107] and, as in other Ricci's holographic models [36, 37, 38, 125], it crosses the phantom divide line at recent times (see right panel of Fig. 7.2). Curiously enough, the Ω_{X0} and c^2 best fit values of this model agree within 1σ with the corresponding values obtained by Suwa *et al.* [38] despite the use of a very different interaction term between the dark components.

As mentioned in §2.5.3 holographic models do not contain the ΛCDM model as a limiting case. It is also noteworthy that, in general, the c^2 term in the holographic expression for the dark energy, Eq. (2.45), should not be considered constant except precisely when the Ricci's length is chosen as the infrared cutoff [33].

A lingering problem, both for this model and the ΛCDM model, refers to the age of the old quasar APM 08279+5255 at redshift $z = 3.91$. In both models the measured quasar age would fall within 1σ only if the Hubble

Model	χ^2_{sn}	χ^2_{cmb}	χ^2_{bao}	χ^2_{X-rays}	χ^2_H	χ^2_{gf}	$\chi^2_{\rm total}$	$\chi^2_{\rm total\ dof}$
Holographic	543.70	0.01	1.20	41.79	9.57	1.06	597.34	0.96
ΛCDM	542.87	0.05	1.13	41.59	8.73	0.43	594.80	0.96

Table 7.1: χ^2 values of the best fit holographic model ($\Omega_X = 0.707 \pm 0.009$, $c^2 = 0.407^{+0.033}_{-0.028}$, $r_f = 0.013^{+0.006}_{-0.005}$, and $H_0 = 71.8 \pm 2.9\,$km/s/Mpc), and the best fit ΛCDM model ($\Omega_{M0} = 0.266 \pm 0.006$, and $H_0 = 71.8 \pm 1.9$ km/s/Mpc).

constant, H_0, would come down substantially -something we do not expect although it cannot be excluded. Accordingly, we must wait for further observational data to see whether the present tension gets exacerbated or disappears.

Before closing, it results interesting to contrast the model explored in this Chapter with the model of §5. The present one shows a better fit to the growth function at low redshifts, as well as to the CMB-shift and BAO data. However, it does not fit so well the age of the old quasar APM 08279+5255.

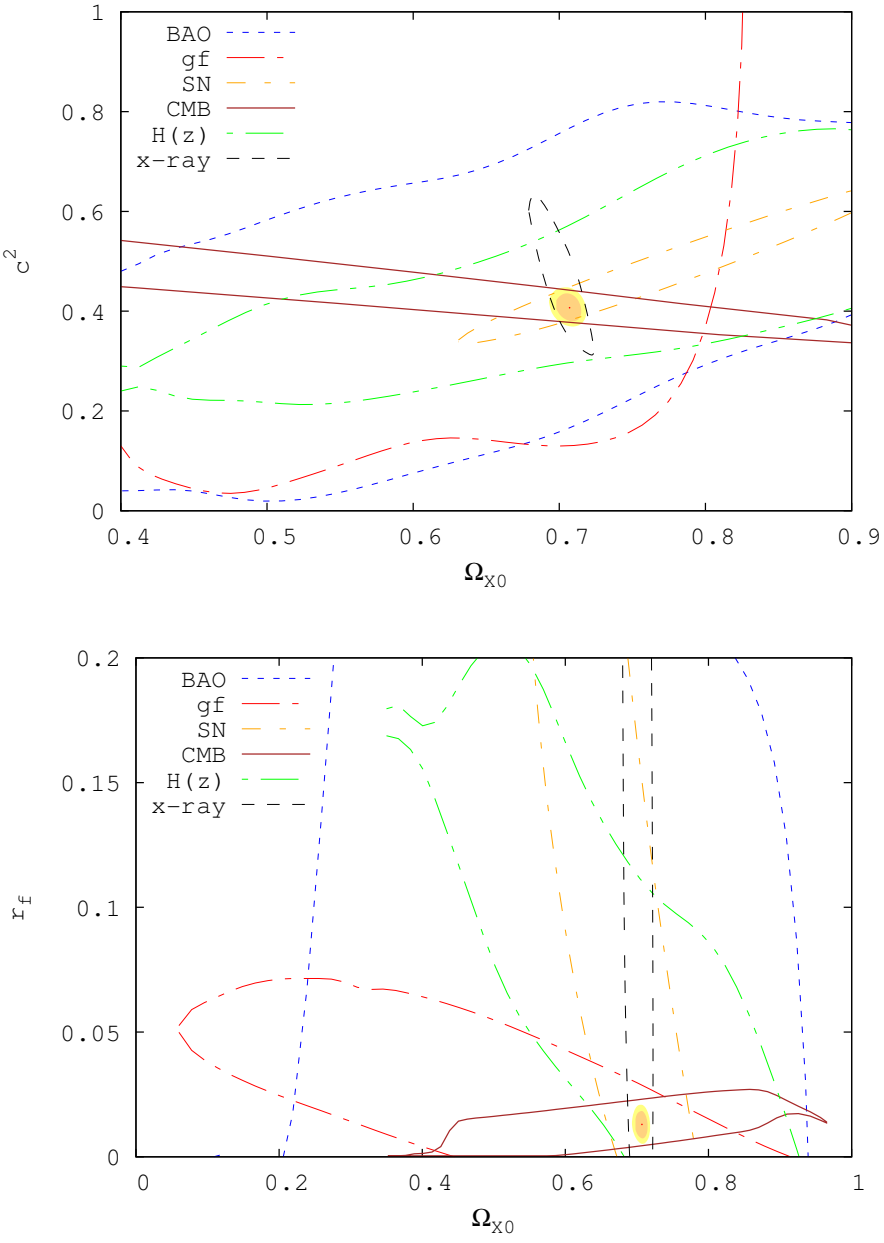

Figure 7.10: Top panel: The probability contours for SN Ia, CMB, BAO, X-ray, $H(z)$, and growth function, in the (Ω_{X0}, c^2) plane. The joined constraint uses $\chi^2_{\rm total} = \chi^2_{sn} + \chi^2_{cmb} + \chi^2_{bao} + \chi^2_{X-rays} + \chi^2_{Hubble} + \chi^2_{gf}$. Bottom panel: Idem for the (Ω_{X0}, r_f) plane.

Chapter 8

Decomposing a unified dark matter model

8.1 Background equations

The unified dark matter model introduced in [45] was described by the equation (2.51). If one wishes to build a model featuring the same background evolution but with an interaction between dark matter and vacuum, the linking equations for the scenarios, interacting and unified, are

$$P_U = P_V = -\rho_V \qquad \text{and} \qquad \rho_U = \rho_C + \rho_V \,, \tag{8.1}$$

where ρ_V and ρ_C denote the vacuum and dark matter energy density respectively, and the vacuum pressure obeys $P_V = -\rho_V$. The evolution equations for the interacting model are

$$\dot{\rho}_C + 3H\rho_C = Q_C \qquad \text{and} \qquad \dot{\rho}_V = Q_V \,, \tag{8.2}$$

where to ensure energy conservation, $Q_C = -Q_V$. Fig. 8.1 shows the evolution of the dark matter (left panel) and vacuum (right panel) energy densities.

In order to derive an expression for the speed of sound of the unified fluid, we differentiate with respect to time the first constraint in (8.1), to obtain, using (8.1) again,

$$3H\rho_C \frac{dP_U}{d\rho_U} = \dot{\rho}_V \tag{8.3}$$

and after using eq.(2.51) we get

$$c_{s\,U}^2 \equiv \frac{dP_U}{d\rho_U} = \frac{\rho_V}{A\rho_s\rho_\Lambda}\left(2A\rho_\Lambda - \rho_V\right) \,, \tag{8.4}$$

where $A = \left(1 - \tanh(\frac{\rho_\Lambda - \rho_t}{\rho_s})\right)^{-1}$. The transition redshift, z_{tr}, was defined in [45] as the redshift at which $c_{s\,U}$ has its maximum value. The change in the sound speed is the cause of the transition from a period of matter domination to the present accelerated expansion.
To get an expression for the energy densities, we use eq. (8.4) in eq.(8.3), and bearing in mind (8.2) we obtain

$$\dot{\rho}_V = \frac{3H\rho_C}{A\rho_s\rho_\Lambda}\rho_V\left(2A\rho_\Lambda - \rho_V\right) , \tag{8.5}$$

$$\dot{\rho}_C = -\frac{3H\rho_C}{A\rho_s\rho_\Lambda}\left[A\rho_s\rho_\Lambda + \rho_V\left(2A\rho_\Lambda - \rho_V\right)\right] , \tag{8.6}$$

where we can identify

$$Q_V = 3\,H\,\rho_V\,\rho_C\,\mathcal{Q}(\rho_V) , \tag{8.7}$$

with $\mathcal{Q}(\rho_V) \equiv \frac{2A\rho_\Lambda - \rho_V}{A\rho_s\rho_\Lambda}$. Introducing the first eq. of (8.2) in eq. (8.5), and integrating, one follow

$$\rho_C - \rho_{C0} = -\rho_V + \rho_{V0} + \frac{\rho_s}{2}\ln\left(\frac{\rho_{V0}(\rho_V - 2A\rho_\Lambda)}{\rho_V(\rho_{V0} - 2A\rho_\Lambda)}\right) . \tag{8.8}$$

Finally, imposing $\rho_V = \rho_\Lambda$ when $\rho_C = 0$ in the integration constants, last expression reduces to

$$\rho_C = -\rho_V + \rho_\Lambda + \frac{\rho_s}{2}\ln\left[\frac{\rho_V - 2A\rho_\Lambda}{\rho_V(1-2A)}\right] . \tag{8.9}$$

Notice that if we look at eq. (8.5) as a one dimensional dynamical system (we can write ρ_C as a function of ρ_V using eq. (8.9) and as we just consider expanding FLRW universes, $H > 0$), we see that it has three fixed points $\rho_V = 0$, $\rho_C = 0$ (equivalent to $\rho_V = \rho_\Lambda$ through eq. (8.9)) and $\rho_V = 2A\rho_\Lambda$. We should point out that in the interval $0 \leq \rho_V \leq \rho_\Lambda$, $\dot{\rho}_V \geq 0$ ($\rho_V \leq 2A\rho_\Lambda$ by the definition of A) and so $\rho_V = 0$ is equivalent to $a = 0$, and $\rho_V = \rho_\Lambda$ to $a \to \infty$. So, the point in $\rho_V = 0$ is unstable and located in the far past and the one in $\rho_C = 0$ is stable and to be reached only in the far future. Notice then, that the integration limits give a definition for the constant ρ_Λ, i.e., it is the value of the interacting vacuum energy in the far future. The other fixed point, $\rho_V = 2A\rho_\Lambda$, is unphysical because $\rho_C \to -\infty$.
From eqs. (8.1) and (8.9) we obtain the EoS parameter of the unified model as

$$w_U \equiv \frac{P_U}{\rho_U} = -\frac{2\rho_V}{2\rho_\Lambda + \rho_s\ln\left[\frac{\rho_V - 2A\rho_\Lambda}{\rho_V(1-2A)}\right]} . \tag{8.10}$$

We could use eqs. (8.5) and (8.9) to obtain numerically ρ_C and ρ_V, but due to the presence of ρ_V^{-1} in the square parethesis of eq. (8.9), and ρ_V being zero for a long time, it seems a better option to solve numerically the unified dark matter conservation equation

$$\dot{\rho}_U + 3H(\rho_U + P_U) = 0\,, \tag{8.11}$$

and then through eqs. (2.51) and (8.1) split it in ρ_C and ρ_V. In this scenario

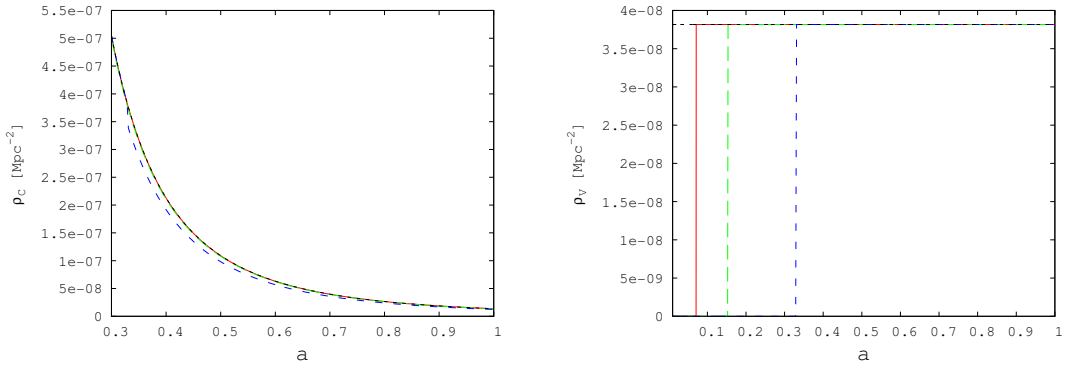

Figure 8.1: Left panel depicts ρ_C and right panel ρ_V for the model described by eq. (2.51), both interacting and unified scenarios and ΛCDM model. Red (solid) line is for $\rho_s = 0.5\rho_\Lambda$ and $\rho_t = 10^3\rho_\Lambda$, green (long dashed) line for $\rho_s = 0.1\rho_\Lambda$ and $\rho_t = 10^2\rho_\Lambda$ and blue (short dashed) line for $\rho_s = 10^{-7}\rho_\Lambda$ and $\rho_t = 10\rho_\Lambda$. Black (dotted) line is for ΛCDM.

the speed of sound of both components, cold dark matter and vacuum is a constant. So the transition redshift, z_{tr}, describes when the interaction takes place. From equation (8.7), we can see that $Q_V = 0$, both when $a \ll 1$ and $a \gg 1$ and the parameter ρ_s determines the time during which dark matter and vacuum interact between each other.

8.2 Vacuum energy momentum tensor

As is well known, the stress-energy tensor of the vacuum can be described by

$$T^V_{\mu\nu} = -\rho_V\, g_{\mu\nu}\ . \tag{8.12}$$

Since $\rho_V + P_V = 0$, the four-velocity of the vacuum, u^μ, is undefined. Because the vacuum stress-energy tensor, $T^{V\,\mu}_{\nu}$ is proportional to the metric

tensor, any four-velocity is an eigenvector, and all observers see the same energy density ρ_V. However, due to the interaction between dark matter and vacuum, the vacuum stress-energy tensor is not conserved

$$T^{V}{}_{\nu}{}^{\mu}{}_{;\mu} = -Q^V_\nu \ . \tag{8.13}$$

From eqs. (8.12) and (8.13), it follows that

$$Q^V_\nu = -\rho^V_{;\nu} \ . \tag{8.14}$$

Therefore so long $Q^V_\nu \neq 0$, the vacuum is spacetime inhomogeneous. Although the vacuum does not have a well defined four-velocity, using the energy flow Q^V_ν, we can define a preferred unit four-vector

$$u^\mu_V = \frac{\rho_V^{;\mu}}{|\rho^V_{;\nu}\rho_V^{;\nu}|^{\frac{1}{2}}} \ . \tag{8.15}$$

Even if the background interaction is determined, there is still freedom to choose the energy transfer direction, $Q^V_\nu = Q^V \breve{u}_\nu$. The simplest case corresponds to the one in which the flux is parallel to the dark matter four-velocity, i.e., $\breve{u}_\nu = u^C_\nu$. Also, as the total stress-energy tensors should be conserved,

$$T^{\mu}_{\nu\, C\, ;\mu} = Q^C_\nu \ . \tag{8.16}$$

and so $Q^C_\nu = -Q^V_\nu$.

8.3 Linear perturbations

Since at background level, both unified and interacting scenarios have an identical behavior, we need to go to the perturbation level to distinguish them.

8.3.1 UDM model

In this case we just have a dark component, UDM, evolving independently from baryons and photons, apart from the constraints on the potentials ψ and ϕ. The evolution equation of the density contrast, δ_U of the UDM fluid is

$$\begin{aligned} \delta'_U \ &+ \ 3\mathcal{H}(c^2_{s\,U} - w_U)\delta_U + (1+w_U)\theta_U + 3\mathcal{H}\left[3\mathcal{H}(1+w_U)(c^2_{s\,U} - w_U) + w'_U\right]\frac{\theta_U}{k^2} \\ &\quad -3(1+w_U)\psi' + (1+w_U)(B-E')k^2 = 0 \ , \end{aligned} \tag{8.17}$$

$$\theta'_U \ + \ \mathcal{H}(1-3c^2_{s\,U})\theta_U - \frac{c^2_{s\,U}}{(1+w_U)}k^2\delta_U - k^2\phi = 0 \ , \tag{8.18}$$

8.3.2 Interacting model

In this case we have dark matter and vacuum interacting also non gravitationally with each other according to eqs. (8.5) and (8.6). Notice that eqs. (3.19) and (8.14) imply a constraint between the gradient $(\delta\rho^V_{,i})$ and the force $([f + Q_V(v_V + B)]_{,i})$, i.e., $-af_V = \delta\rho_V + aQ_V(v_C + B)$ [57]. For the vacuum, eq.(3.37) reduces to $\delta P = -\delta\rho_V$, which could also be inferred from the first equation in (8.1). This means that $c^2_{s\,V} = -1$, but this is not a problem since the vacuum does not have a physical sound speed, as long as it does not propagate. For this reason it seems reasonable to choose $v = v_C$ to set the direction of the energy flow - see eqs. (3.18) and (3.19).
In §3.6 the conservation equations for interacting fluids where given, and as the conservation of momentum implies $f_C = -f_V$, the resulting equations for the interacting dark matter are

$$\delta'_C + \theta_C - 3\psi' + (B - E')k^2 = 3\mathcal{H}\rho_V\mathcal{Q}\,(\delta_C - \phi) - \frac{a}{\rho_C}\delta Q_V, \quad (8.19)$$

$$\theta'_C + \mathcal{H}\theta_C - k^2\phi = -\frac{k^2 a f_C}{\rho_C}\,, \quad (8.20)$$

and

$$\delta'_V = 3\mathcal{H}\rho_C\mathcal{Q}\,(\phi - \delta_V) + \frac{a}{\rho_V}\delta Q_V\,, \quad (8.21)$$

$$\delta_V = 3\mathcal{H}\rho_C\mathcal{Q}\frac{\theta_C}{k^2} - \frac{a}{\rho_V}f_V\,, \quad (8.22)$$

for the inhomogeneous vacuum. Note that the momentum continuity equation (8.22) is just the link derived from the momentum flow.

8.4 Results

To obtain numerical solutions we resort to a modified version of the code CLASS [82]. This code can use the synchronous gauge (§3.9), as well as the Newtonian one (§3.10). Here we will use the synchronous gauge, that is defined by assuming that cosmic time in the background coincides with the proper time for observers at fixed spatial coordinates. In this gauge, there are some gauge degrees of freedom remaining, since the initial hypersurfaces and their coordinates are not fixed. This is usually set by assuming that the dark matter particles are at rest in this frame, i.e., $\theta_C = 0$. We will do so in the dark matter (geodesic) case but not in the UDM case, as it does not

behave like dust. So, in this gauge eqs. (8.18) and (8.17) read

$$\delta'_U = -3\mathcal{H}(c_{s\,U}^2 - w_U)\delta_U - (1+w_U)\left(\theta_U + \frac{h'}{2}\right) , \tag{8.23}$$

$$\theta'_U = -\mathcal{H}(1-3w_U)\theta_U - \frac{w'_U}{1+w_U}\theta_U + \frac{c_{s\,U}^2}{(1+w_U)}k^2\delta_U . \tag{8.24}$$

In the UDM case we cannot fix $\theta_U = 0$, since $w_U \neq 0$, and even imposing the initial condition $\theta_U = 0$, there is an evolution in time. Figure 8.2 shows the matter power spectrum for the unified scenario. One can see in the plots, that only the very slow transition region is compatible with observation. In this regime, the model is nearly indistinguishable from ΛCDM [45].

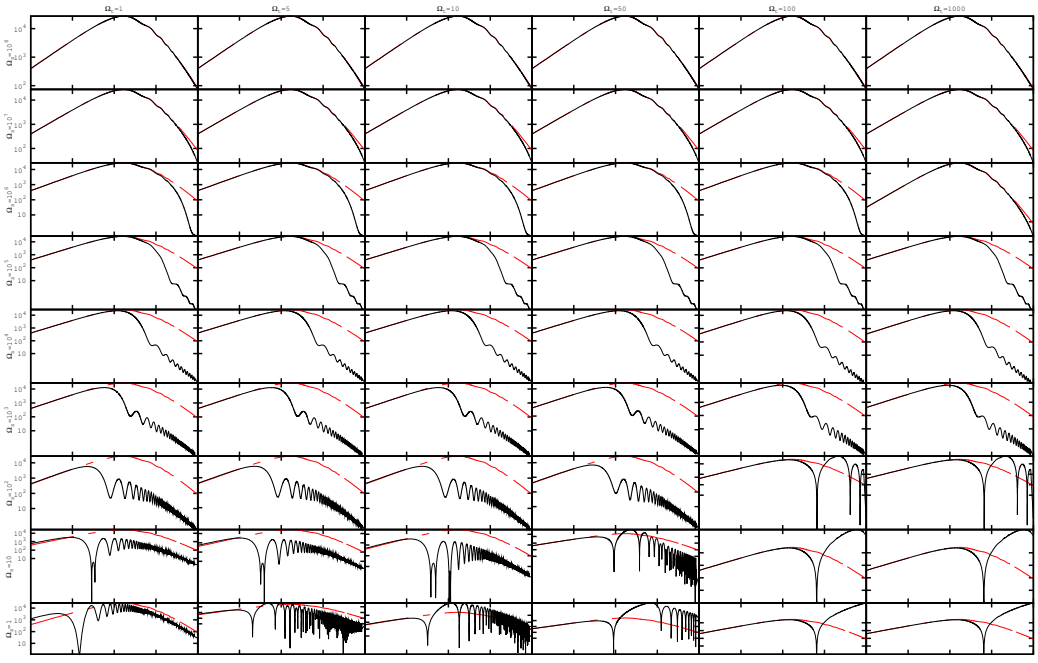

Figure 8.2: Matter power spectrum for the Unified model. In the rightmost column $z_{tr} \simeq 13$ and for the leftmost one $z_{tr} = 0$. The top line is in the very slow transition regime and the bottom one in the fast (but not fastest due to numerical problems in dealing with it).

In the interacting case we can fix the energy flow to be geodesical, to follow

the motion of the dark matter particles, i.e., $Q^\mu_A = Q_A u^\mu_c$, whence there is no momentum transfer, $f_C = -f_V = 0$, or alternatively let the interaction be just $Q^\mu_V = \nabla^\mu \rho_V$ and impose the total energy density to behave barotropically. We will study both, and call the latter case barotropic.

8.4.1 Geodesical case

When the flow obeys $Q^\mu_A = Q_A u^\mu_c$, we fix the gauge degree of freedom as usual by setting $\theta_C = 0$. Then the evolution equation for interacting dark matter density perturbations is

$$\delta'_C = 3\mathcal{H}\rho_V \mathcal{Q}\delta_C - \frac{h'}{2} \,. \tag{8.25}$$

As we can see that in the synchronous gauge, eq. (8.22) gives us $\delta_V = 0$. One can also notice that, except for the different behavior of the background evolution, the perturbation equations for $\delta\rho_C$ and θ_C are exactly those of a non interacting vacuum plus dark matter cosmology. Figures 8.3 and 8.4 show the matter power spectrum and temperature anisotropies for the interacting (geodesic) scenario. It can be seen that the parameter region allowed for the model is much wider than in the unified case, and is compatible with models very different from ΛCDM.

8.4.2 Barotropic case

This case corresponds to $Q_\mu = [-\dot{\rho}_V, \partial_i \rho_V]$. Since eq. (8.9) is a monotonically decreasing function of time, it can be inverted to express ρ_V in terms of ρ_C. We then impose the global adiabaticity condition (3.31). Thus, the velocity and density perturbation conservation equations become

$$\delta'_C = 3\mathcal{H}\rho_V \mathcal{Q}\delta_C - \left(\theta_C + \frac{h'}{2}\right) - \frac{\delta\rho'_V}{\rho_C} \,, \tag{8.26}$$

$$\theta'_C = -\mathcal{H}\theta_C - \frac{k^2\delta\rho_V}{\rho_C} + 3\mathcal{H}\rho_V \mathcal{Q}\theta_C \,. \tag{8.27}$$

Notice that in this last case we cannot set $\theta_C = 0$, as in the UDM one. From figure 8.5 we see that now the matter power spectrum and the CMB power spectrum look identical to the one of the unified model. This fact is derived analytically in the next section.

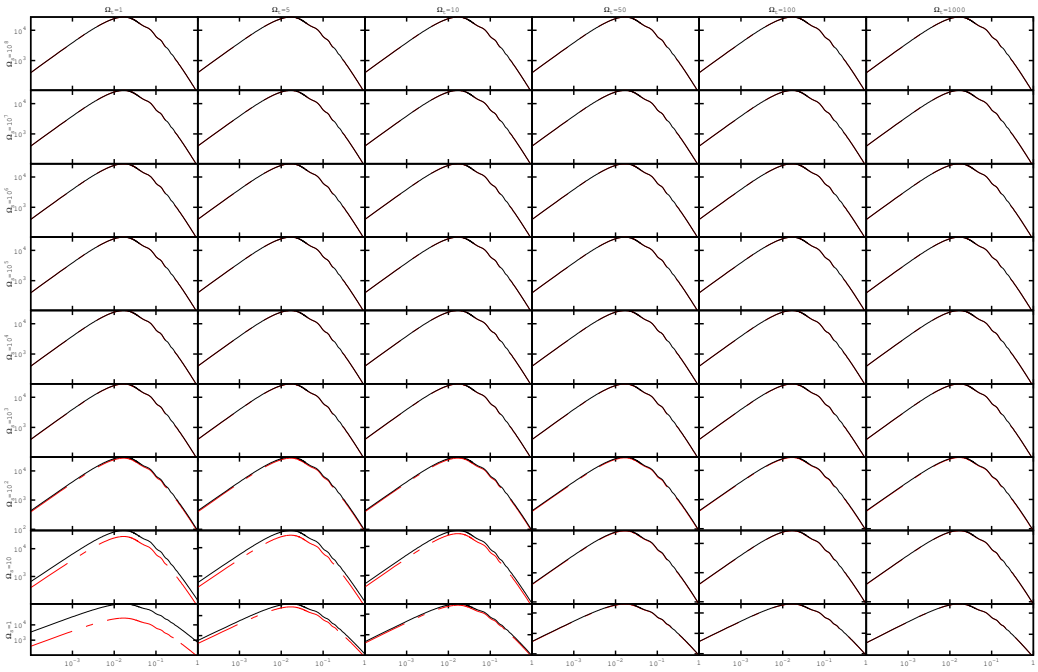

Figure 8.3: Matter power spectrum for the interacting (geodesic) model. In the rightmost column the interaction takes place at $z_{int} \simeq 13$ and for the leftmost one at $z_{int} = 0$. The top row corresponds to models in which the interaction lasts a long time, and the bottom one to models where it lasts very little.

8.5 Relation between the perturbations in the unified fluid and in the interacting (barotropic) cases

From the Einstein equations (3.56) and (3.57) we introduce the total density and velocity perturbations

$$\delta\rho = \delta\rho_C + \delta\rho_V \ , \tag{8.28}$$

$$\theta = \frac{\rho_C}{(\rho_C + \rho_V)(1 + w_T)}\theta_{CDM}. \tag{8.29}$$

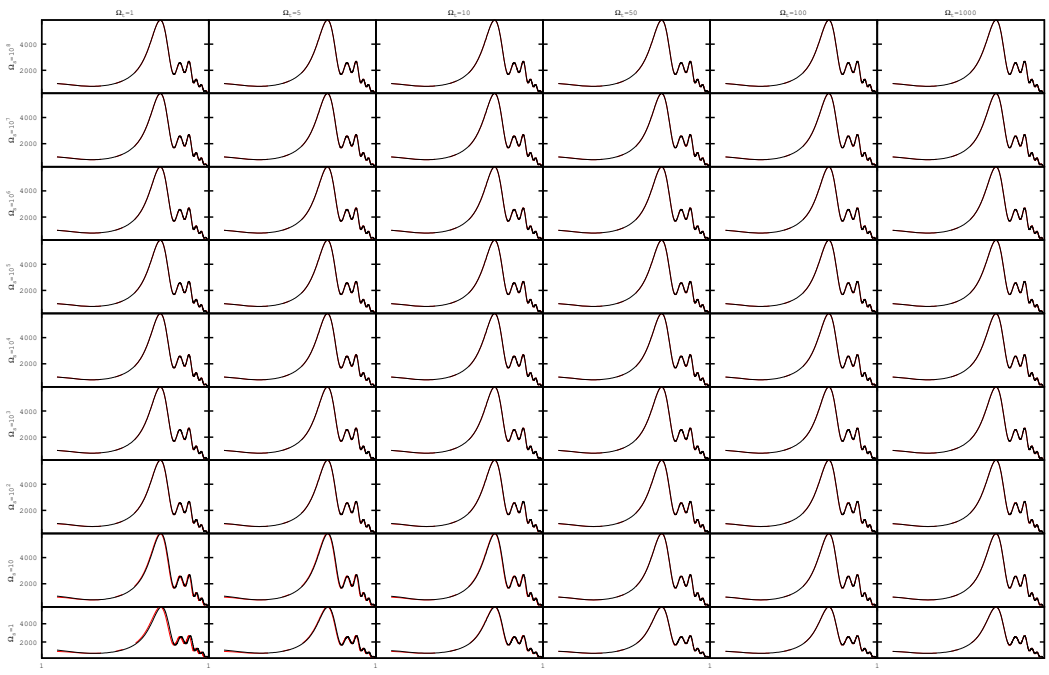

Figure 8.4: Temperature anisotropies for the interacting (geodesic) model. The different plots are explained in Fig. 8.3.

where $\rho = \rho_C + \rho_V$. This total perturbations will follow the same equations as the unified fluid, eqs. (8.23) and (8.24). We rewrite them as

$$\delta\rho' = -3\mathcal{H}(1+c_{sT}^2)\delta\rho - (1+w_T)\rho\left(\theta + \frac{h'}{2}\right) , \tag{8.30}$$

$$\theta' = -\mathcal{H}(1-3c_{sT}^2)\theta + \frac{c_{sT}^2}{(1+w_T)\rho}k^2\delta\rho , \tag{8.31}$$

to simplify the later calculations. Using eq. (8.29), we recast eq.(8.30) as

$$\delta\rho' = -3\mathcal{H}(1+c_{sT}^2)\delta\rho - \rho_C\theta_C - (1+w_T)\rho\frac{h'}{2} . \tag{8.32}$$

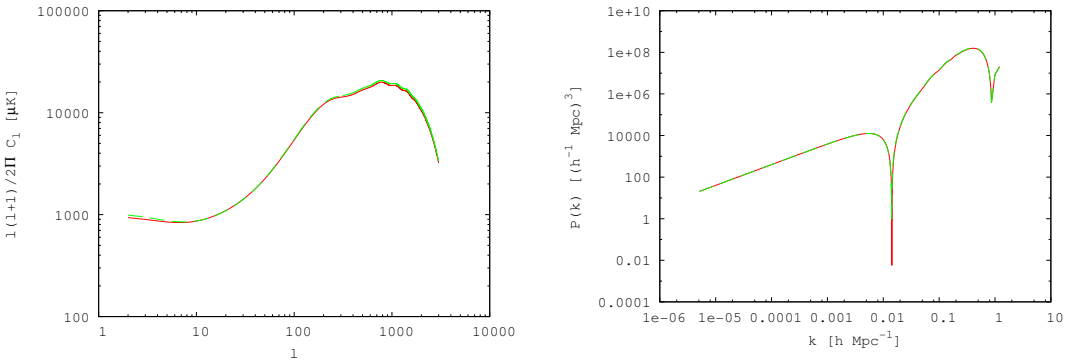

Figure 8.5: Left panel depicts the CMB power spectrum and the right panel the matter power spectrum for the unified, interacting and ΛCDM models. Red lines are for the UDM model and green for the interacting (barotropic) ones. In drawing the graphs we used $\rho_s = 10^{-1}\rho_\Lambda$ and $\rho_t = \rho_\Lambda$.

Then, we use the background relations $c^2_{sT} = \frac{\delta P}{\delta \rho} = -\frac{\delta \rho_V}{\delta \rho}$ and $w_T = \frac{P}{\rho} = -\frac{\rho_V}{\rho}$ to finally obtain

$$\delta'_C = -\left(\theta_C + \frac{h'}{2}\right) - \frac{Q_C + \delta\rho'_V}{\rho_C} \ . \tag{8.33}$$

This expression coincides with eq. (8.26). Now let's see what happens with eq. (8.31). The time derivative of eq.(8.29) can be written as

$$\theta' = 3\mathcal{H}c^2_{sT}\theta_C + \frac{Q_C}{\rho_C}\theta_C + \theta'_C \ , \tag{8.34}$$

after using the adiabaticity condition $w'_T = \frac{\rho'}{\rho}(c^2_{sT} - w_T)$. Inserting eq.(8.34) into eq.(8.31), we get

$$\theta'_C = -\mathcal{H}\theta_C - k^2\frac{\delta\rho_v}{\rho_C} + \frac{Q_V}{\rho_C}\theta_C \ , \tag{8.35}$$

expression identical to eq. (8.27). The matter spectrum and temperature anisotropies for the unified and the interacting (barotropic) scenarios are shown in Fig. 8.5.

8.6 Conclusions

In this Chapter we consider an equation of state for the dark sector from two different points of view. The first one, already studied in [45], it is seen

as a unified dark matter model. Due to the effects of the sudden change in the speed of sound, the parameter regions compatible with observations are very narrow, as shown in Fig. 8.3. Only very slow transitions are allowed, and for those parameters, the model behaves similarly to ΛCDM. It is not seen in Fig. 8.3, but fast transitions are also allowed, provided they happen at $z_{tr} \gg 1$. Those cases are very hard to deal with numerically since $c^2_{s\,U}$ behaves like a Dirac's delta.

It is of theoretical interest that, as was already shown in [57], any unified model can be described as a cold dark matter plus vacuum, with both components interacting with one another. For both scenarios to be completely equivalent at the bakcground and perturbative (first order) levels, the interaction should be of the barotropic kind (§8.4.2). Instead of this, one can define the interaction to be geodesic (§8.4.1), and then the equivalence at the perturbative level is broken. For the interacting (geodesic) scenario, models that behave differently from ΛCDM (see Fig. 8.1) are however allowed by observations.

Chapter 9

The Matter Power Spectrum of Dark Energy Models and the Harrison-Zel'dovich Prescription[1]

9.1 Introduction

In the concordance ΛCDM cosmological model, the current accelerated phase of expansion is driven by a cosmological constant Λ that dominates the present energy density of the Universe, whose equation of state parameter is $w = -1$. The second component in importance is cold dark matter, which drives the growth of large scale structure (LSS). This simple model fits rather well the observational data and requires the minimum set of cosmological parameters [3]. Also, it is the preferred model based on statistical selection criteria [127]. The observational successes of the ΛCDM cosmology is linked to its capacity to reproduce the right sequence of cosmological eras: matter-radiation equality occurs well before recombination and the matter dominated period lasts long enough to allow the growth of LSS. The length of the radiation and matter periods are crucial to determine the shape of the matter and radiation power spectra. Alternative models must also reproduce the correct sequence of cosmological eras to fit the data [128].

While the ΛCDM model fits the observational data very well, it appears rather unsatisfactory from the theoretical point of view. In fact, a cosmo-

[1]This Chapter corresponds to Ref. [126].

logical constant is not very appealing. Its measured value is 120 orders of magnitude smaller than the expected amplitude at the Planck scale and introduces the coincidence problem. This is why a plethora of more flexible models that behave akin to the ΛCDM at the background level have been introduced over the years -see [4, 17] for recent reviews. This complicates enormously the task of judiciously deciding which model should be preferred over all the others in view of their observational and theoretical merits. For instance, the acceleration could be driven by a dark energy component with EoS parameter $w \neq -1$ [129], constant or variable on cosmological timescales. The simplest variants require cosmological parameters to be fine tuned at some initial time, suffering also -though, at a lower extent- from the coincidence problem and more complex models have been introduced, e.g. [102, 130]. Before carrying out a detailed analysis, these alternatives first use probes of the cosmic expansion history such as luminosity distances derived from supernovae type Ia data, angular diameter distances from baryon acoustic oscillations (BAO), the expansion rate, H, at various redshifts, etc. [131, 39, 99]. Data on matter density perturbations and cosmic microwave background (CMB) anisotropies provide stronger constraints but require to solve the time evolution of the density perturbations in all components. In general, the resulting set of equations is far more involved than in the standard ΛCDM model. Furthermore, small differences on the dynamics of the dark sector change the equations governing the evolution of matter perturbations [132], and no generic constraints can be imposed on large classes of models. As a result, many models in the literature have not been constrained by the current data on density inhomogeneities and CMB temperature anisotropies -see e.g. [133].

The aim of this Chapter is to show how to derive the matter power spectrum of a generic dark energy model without the need of solving in full the perturbation equations for the radiation and matter components. Several observables can be computed in terms of the matter power spectrum alone and can be used to constrain the model beyond the expansion rate. The observables include: (a) the fluctuation of the matter density perturbations on a sphere of $8h^{-1}$Mpc, σ_8 [134]; (b) the rms peculiar velocity of matter on spheres of radius R, $\langle v^2(R)\rangle^{1/2}$ [135]; (c) the weak lensing convergence spectrum [136]; (d) the Sachs-Wolfe (SW) and Integrated Sachs-Wolfe (ISW) components of the CMB temperature anisotropies [66]; (e) the cross-correlation of the ISW with templates of projected density of galaxies [137], etc. For example, the SW and ISW effects are the dominant contributions to the CMB anisotropies at low multipoles. If the power spectrum is normalized to the measured value $\sigma_8 = 0.801 \pm 0.030$ [138], the predicted low

order multipoles of the CMB, the peculiar velocity on a given scale [139] or the measured ISW-Large Scale Structure cross-correlation [140] can be compared with observations. Our method provides simple tests of models using a wealth of data beyond luminosity and angular diameter distance measurements.

The idea of how to construct the matter power spectrum is based on the Harrison-Zel'dovich (HZ) [90, 91] prescription. For any two models, the amplitude of density perturbations are specified at horizon crossing instead of at some arbitrary initial hypersurface. The final spectrum will differ only by the subsequent (subhorizon) evolution of each single mode. If we use as a starting model one that is implemented on publicly available numerical codes like CMBFAST [80], for example the concordance ΛCDM model, we will be able to construct the power spectrum of a generic dark energy model (not implemented on numerical codes). The method can be used to derive the power spectrum ranging from galaxy to horizon scales, i.e., at all the scales that can be observed at present.

In developing this method, our aim is not to use it to solve models of dark energy with a constant EoS parameter. In section 9.3, we consider a dark energy model with constant EoS parameter, $w = -0.5$ (though being aware that it is observationally discarded) just to illustrate the accurateness of the method in a model which, on the one hand, it is easy to obtain the exact evolution of the perturbations and, on the other hand, its evolution differs substantially from that of the standard ΛCDM. With this we can see that obtaining the matter power spectrum of a dark energy model from the one of ΛCDM is reasonable also in cases when both models differ greatly at the background level.

This method can be useful in solving the perturbation equations of interacting models [141, 32, 39, 99, 104]. Many of these models aim to describe the Universe at low redshifts, when both dark components dominate the expansion. Following our method, the matter perturbations evolve as in the ΛCDM model before horizon crossing (this avoid the need of explicitly introducing initial conditions for the perturbations). Moreover, because it suffices to compute the evolution of the perturbations of the particular dark energy model considered after they enter the horizon, the set of equations to be solved gets greatly simplified. This is shown in §9.3.

9.2 The Harrison-Zeldovich prescription

In their seminal papers, Harrison and Zel'dovich [90, 91] computed the present matter power spectrum assuming that all perturbations at horizon crossing have the same amplitude. Then, they computed the matter power spectrum $P(k)$ at the present time after accounting for the subhorizon evolution of each mode. To illustrate their argument, let us construct the power spectrum of the standard CDM model, a model that only contains dark matter , baryons and radiation (subscripts CDM, B, and R, respectively), and verifies $\Omega_{CDM} + \Omega_B + \Omega_R = 1$, where Ω_i is the energy density of component i in units of the critical density. Let us define the density contrast by $\delta(k,t) = (\delta\rho/\bar{\rho})(k,t)$. In the linear regime, spatial and time dependence can be separated: $\delta(k,t) = \delta(k)D_+(t)/D_+(t_0)$, where $D_+(t)$ denotes the growing solution and $\delta(k)$ is evaluated at the present time, t_0. The current power spectrum is then defined as: $P(k) = |\delta(k)|^2$.

In the standard cold dark matter (CDM)model, $D_+(t) \approx$ const during the radiation dominated era and $D_+(t) = D_+(t_{in})(t/t_{in})^{2/3}$, during the matter dominated period. The HZ prescription establishes that all mass perturbations, defined as $\Delta(k,t) = \frac{1}{2\pi^2}k^3P(k)(D_+(t)/D_+(t_0))^2$, have the same amplitude at the time t_{in} when they enter the horizon, i.e., $a(t_{in})\lambda_{in} = d_H(t_{in})$ where $a(t)$ is the scale factor, $d_H(t)$ the radius of the horizon, and λ_{in} the comoving wavelength of each particular mode; $k_{in} = 2\pi/\lambda_{in}$ would be the corresponding wavenumber. In particular

$$\Delta(k_{in}, t_{in}) = \text{const} = \Delta(k_{eq}, t_{eq}), \tag{9.1}$$

with t_{eq} the moment of matter-radiation equality.

Once a perturbation enters the horizon, it will evolve as $D_+(t)$ and we can write

$$\begin{aligned} \Delta(k_{eq}, t_0) &= \left(\frac{D_+(t_0)}{D_+(t_{eq})}\right)^2 \Delta(k_{eq}, t_{eq}) = \left(\frac{D_+(t_0)}{D_+(t_{eq})}\right)^2 \Delta(k_{in}, t_{in}) \\ &= \left(\frac{D_+(t_{in})}{D_+(t_{eq})}\right)^2 \Delta(k_{in}, t_0)\,. \end{aligned} \tag{9.2}$$

equation The evolution after horizon crossing depends on whether it occurs before or after matter-radiation equality:

1. If $t_{in} < t_{eq}$, then $D_+(t_{in}) = D_+(t_{eq})$ because perturbations are essentially frozen in the radiation era. Consequently, $P(k_{in}) = P(k_{eq})\,(k_{in}/k_{eq})^{-3}$.

2. If $t_{in} > t_{eq}$, then $D_+(t_{in})/D_+(t_{eq}) = (t_{in}/t_{eq})^{2/3} = (k_{eq}/k_{in})^2$. In the last equality we have used the relation between the comoving wavenumber and the time of horizon crossing $k_{in} \propto t_{in}^{-1/3}$, valid in the matter era. Then $P(k_{in}) = P(k_{eq})\,(k_{in}/k_{eq})$.

As a consequence of the growth of density perturbations in the matter and radiation epochs, the power spectrum has two asymptotic regimes: $P(k) \sim k^1, k^{-3}$ at large and small scales, respectively, with a maximum at the scale of matter-radiation equality. Since the transition from the radiation to the matter dominated period is not instantaneous, $P(k)$ has a smooth maximum about matter-radiation equality, at k_{eq}. The power spectrum is conveniently expressed as $P(k) = A\,k^n\,T^2(k)$, where A is a normalization constant and n the spectral index at large scales. The transfer function $T(k)$ is determined by the growth rate within the horizon. In the specific case of the HZ prediction, $n = 1$.

9.3 The matter power spectrum of generic dark energy models

The spectra of the concordance ΛCDM models differ from the spectra of models with no cosmological constant in two main respects, namely: (i) the scale of matter radiation equality is shifted to larger scales, and (ii) the growth factor of matter density perturbations slows down once the overall expansion accelerates. As mentioned above, in this section we shall show how to compute the present matter power spectrum of a dark energy model, in principle not implemented on a numerical package, from the power spectrum of a model that is implemented. As an example, we shall construct the power spectrum of models with $w = -0.8, -0.5, -0.1$ from the concordance ΛCDM. The evolution of density perturbations of dark energy models with constant EoS is implemented in standard packages like CMBFAST and can be computed numerically but they will be useful to estimate the accuracy of the method. For simplicity, all models will share identical cosmological parameters, namely $\Omega_\Lambda = 0.73, \Omega_{CDM} = 0.23, \Omega_B = 0.04$, $H_0 = 71$ km/s/Mpc and $n = 1$. The models differ only in the EoS parameter, w.

Following the HZ prescription, we assume that all perturbations have the same amplitude at horizon crossing. Then, we just need to compare the growth rate of density perturbations in both models once perturbations cross the horizon. Even if the subhorizon evolution of density perturbations is the same in the ΛCDM as in the dark energy model, the final power spectrum

could be different. In each model, fixed comoving wavelengths λ_{in} cross the horizon at different times t_{in} and the growth rate from t_{in} to the present time t_0 will be different for each of them. Then, we need to determine: (i) the size of the horizon as a function of time to fix when a perturbation crosses the horizon, and (ii) solve the equations of evolution of subhorizon density perturbations during the radiation, matter and accelerated expansion epochs. If dark matter and dark energy density perturbations evolve independently during the radiation regime, we can expect the evolution of dark matter perturbations to be independent of the model. Specifically, in the radiation era the expansion timescale is $t_{exp} \propto (G\rho_R)^{-1/2}$ while if the free-fall time of matter within a density perturbation is $t_{ff} \propto (G\rho_{CDM})^{-1/2}$, much smaller than the expansion timescale and matter perturbations will not grow significantly during the radiation regime. With this simplifying assumption, if the dark energy model and ΛCDM have the same matter-radiation equality and perturbations cross the horizon at the same time, then the power spectrum at small scales will have the same shape in both models. Without restricting the applicability of our method, this assumption guarantees that the dark energy model will pass the constraints imposed by the galaxy distribution on scales $\lambda \leq 100$ Mpc $/h$ not less well than the ΛCDM model.

Our method is more easily implemented when the equations of evolution of subhorizon sized perturbations after matter-radiation equality form a closed system and can be solved independently for each energy density component. If both models have identical evolution during the radiation era, once the Universe becomes matter dominated the anisotropic stress due to neutrinos will be negligible and, in the Newtonian gauge, it will suffice just one single gravitational potential -say ϕ- to determine the flat metric element

$$ds^2 = -(1+2\phi)dt^2 + a^2(1-2\phi)dx^i dx_i \,. \tag{9.3}$$

From the (0,0) component of Einstein's equations, the evolution of the gravitational potential is given by

$$\frac{k^2}{a^2}\phi + 3H\left(\dot{\phi} + H\phi\right) = -4\pi G \sum \bar{\rho}_i \delta_i \,, \tag{9.4}$$

where the sum extends over all matter components. If the energy components interact only gravitationally between themselves, then the energy-momentum tensors are individually conserved. For a generic component A, by perturbing the conservation equation $T_A^{\mu\nu}{}_{;\mu} = 0$ one obtains

$$\dot{\delta}_A = -(1+w_A)\left(\frac{\theta_A}{a} - 3\dot{\phi}\right) - 3H\left(c_{s,A}^2 - w_A\right)\delta_A, \tag{9.5}$$

$$\dot{\theta}_A = -H(1-3w_A)\theta_A - \frac{\dot{w}_A}{1+w_A}\theta_A + \frac{k^2}{a\,(1+w_A)}c_{s,A}^2\delta_A + \frac{k^2}{a}\phi, \tag{9.6}$$

For a more general treatment, including interaction between dark energy and dark matter, see e.g. [142]. When the evolution is subhorizon, $k \gg aH$ and time derivatives can be neglected compared to spatial gradients, eq. (9.4) reduces to the Poisson equation:

$$k^2\phi = -4\pi G a^2 \sum \rho_i \delta_i \,. \tag{9.7}$$

Equations (9.5) and (9.6) can be specialized to the case of dark matter, baryons and dark energy, $w_{CDM} = w_B = c_{s,CDM} = c_{s,B} = 0$. If the dark energy sound speed is $c_{s,X} = 1$, then it will not cluster at small scales and we can take $\delta_X \approx 0$. Under this assumption, the equations of evolution of matter density perturbations, defined as $\bar{\rho}_M\delta_M = \bar{\rho}_{CDM}\delta_{CDM} + \bar{\rho}_B\delta_B$ are:

$$\dot{\delta}_M = \frac{\theta_M}{a}, \tag{9.8}$$

$$\dot{\theta}_M = -H\theta_M - \frac{k^2\phi}{a}, \tag{9.9}$$

$$k^2\phi = -4\pi G a^2 \bar{\rho}_M \delta_M. \tag{9.10}$$

From this equations, the evolution of matter density perturbations is described by a single second order differential equation:

$$\ddot{\delta}_M + 2H\dot{\delta}_M - 4\pi G\bar{\rho}_M\delta_M = 0. \tag{9.11}$$

This equation does not depend on unknown functions, so the evolution of matter density perturbations can be solved exactly, as required by our method. In terms of the growth function, f, Eq. (9.11) could be transformed into an even simpler, first order, differential equation (see e.g. [39, 99, 121]).

Let $D_+(t)$ be the growing mode solution of Eq. (9.11). To solve the equation, we need to specify the initial conditions at some arbitrary time. In the CMBFAST code, this is done at some initial space-like hypersurface. In HZ, all modes have the same amplitude at horizon crossing, i.e., amplitudes are fixed at different times for different modes. This amplitude will depend on the model, but for the same wavelength the ratio of amplitudes of different

models will be constant, independent of scale, and this factor could be absorbed into the normalization. But even if the amplitudes at horizon crossing were the same, the current amplitudes will differ because of their different growth rates. When a perturbation of a fixed scale k_{in} enters the horizon at time $t_{in,X}$ and $t_{in,\Lambda CDM}$ it grows by a factor $D_{+,X}(t_{0,X})/D_{+,X}(t_{in,X})$ and $D_{+,\Lambda CDM}(t_{0,\Lambda CDM})/D_{+,\Lambda CDM}(t_{in,\Lambda CDM})$, respectively. Therefore, the final amplitudes will differ by a factor

$$Q(k_{in}) = \frac{D_{+,X}(t_{0,X})/D_{+,X}(t_{in,X})}{D_{+,\Lambda CDM}(t_{0,\Lambda CDM})/D_{+,\Lambda CDM}(t_{in,\Lambda CDM})}\,. \tag{9.12}$$

As a result,

$$P_X(k) = Q^2(k) P_{\Lambda CDM}(k). \tag{9.13}$$

This identity holds even if the spectral index differs from unity, $n \neq 1$.

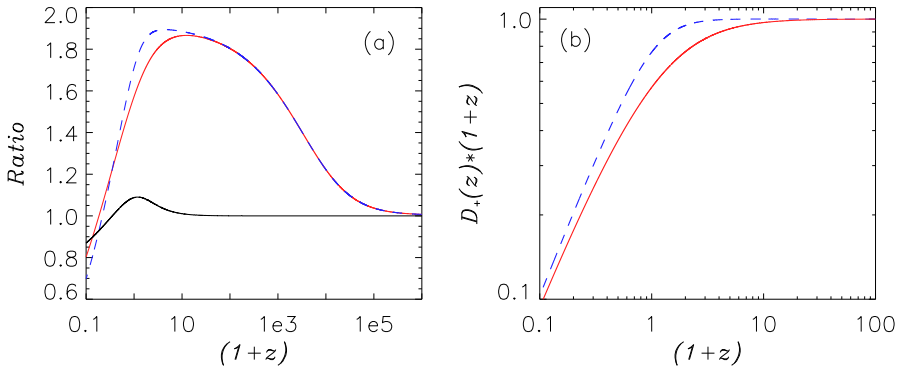

Figure 9.1: (a) Ratios of the horizon radii, d_H, of three cosmological models: standard CDM, concordance ΛCDM, and the $w = -0.5$ dark energy model: $d_{H,\Lambda CDM}(z)/d_{H,CDM}(z)$ (blue dashed line), $d_{H,X}(z)/d_{H,CDM}(z)$ (thick red solid line), and $d_{H,\Lambda CDM}(z)/d_{H,X}(z)$ thin (black) solid line. (b) Growth factors of the ΛCDM (dashed blue line) and dark energy model (solid red line) in units of the growth factor of the standard CDM model, $D_{+,CDM} \sim (1+z)^{-1}$.

To derive $Q(k)$ for each cosmological model we first compute the horizon radius, $d_H(z)$, to determine when a mode enters the horizon, and then solve the dynamical equations to find the subhorizon growth factor $D_+(z)$ after matter-radiation equality. If subhorizon perturbations in ΛCDM and dark

energy models grow at the same rate in the radiation dominated regime, then $Q(k) = \text{const}$ and $\sigma_{8,X} = Q(2\pi/8h^{-1}Mpc)\sigma_{8,\Lambda CDM}$. If both power spectra are normalized at the same amplitude at small scales, then $Q(k \gg k_{eq}) = 1$ and dark energy and ΛCDM spectra will coincide at small scales. The method could be applied to superhorizon scales if the equations of evolution formed a closed system. If not, one can simply extrapolate their amplitude using the HZ prescription. If required, it could also be generalized to include perturbations in other components such as dark energy. It suffices to specify the amplitude of every component at horizon crossing and follow its subsequent evolution.

Figure 9.1a shows the ratio of the comoving size of the horizon between different models; the thick solid (red) and dashed (blue) lines correspond to the ratio of the horizon size of the $w = -0.5$ dark energy and ΛCDM models with respect to the standard ($\Omega_\Lambda = 0$, $\Omega_m = 1$) CDM model. As expected, the size of the horizon is the same in the radiation dominated regime irrespective of the cosmology. The thin (black) solid line represents the ratio of the ΛCDM horizon size to that of the $w = -0.5$ dark energy model, i.e., $d_{H,\Lambda CDM}/d_{H,X}$. In this case the ratio is very similar up to $z \approx 30$. The difference arises because the period of accelerated expansion starts earlier in the dark energy model. In Figure 9.1b we plot the growth factor (in units of the standard CDM growth factor) of the $w = -0.5$ dark energy model, solid (red) line, and the concordance ΛCDM model, dashed (blue) line. All models are normalized so that the amplitudes of the growing modes at recombination are the same: $D_+(z_{rec}) = (1 + z_{rec})^{-1}$, i.e., they coincide with the growth factor of the standard CDM at that redshift ($z_{rec} \approx 1090$).

Figures 9.2a,c,e depict the exact and approximated power spectra. In each panel, the dashed black line represents the power spectra computed numerically using CMBFAST for dark energy with $w = -0.8$ (a), $w = -0.5$ (c), and $w = -0.1$ (e). Solid (blue) lines plot the power spectra derived using our analytic approximation and dot-dashed (red) lines correspond to the concordance ΛCDM model used to construct the approximated solutions. For the first two models, the approximated and exact dark energy spectra are almost indistinguishable on a log-log scale. In Figures 9.2b,d,f we represent the ratio of the approximated to the exact (computed with CMBFAST) power spectrum (solid -blue- line) for (from top to bottom) $w = -0.8, -0.5, -0.1$. The dot-dashed (black) line represents the ratio of the concordance ΛCDM power spectra to the exact dark energy power spectra. The accuracy of our prescription depends on the model parameters. It is within 1-3% for $w = -0.8$, 1-8% for $w = -0.5$, and degrades to 5-35% for $w = -0.1$. Properly speaking, this latter model is not a dark energy model

because it does not lead to a period of accelerated expansion. Even in this extreme case and ignoring the clustering of this "dark energy", the approximation is rather good, the largest error being 35% at $k \sim 5 \times 10^4$Mpc/h. In any case, a certain discrepancy between the numerical and approximated spectra is to be expected, as found around $k \sim 10^{-3}$Mpc/h, since for perturbations that come within the horizon after matter-radiation equality the gravitational potential is still evolving with time and Eq. (9.7) becomes less accurate. Figure. 9.2 is our main result. It shows how useful our prescrip-

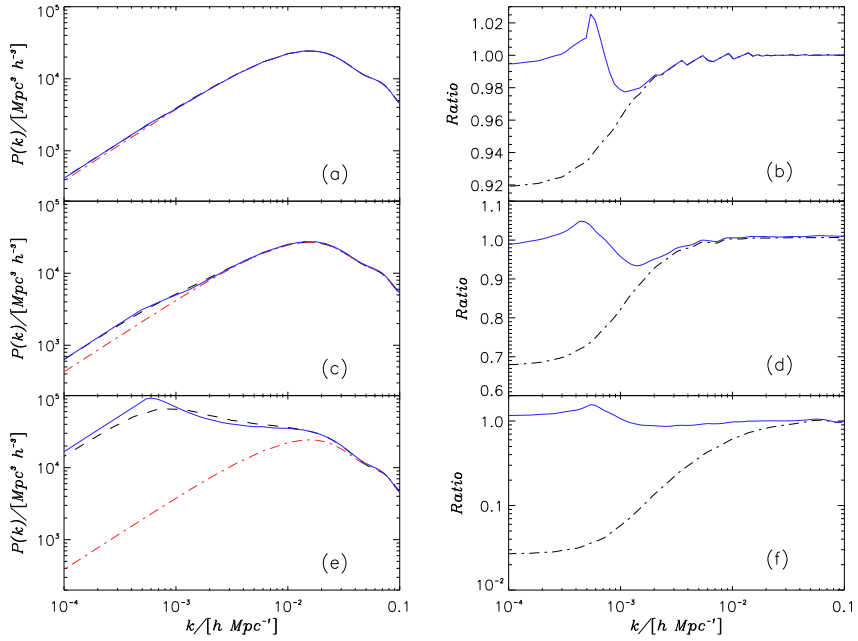

Figure 9.2: (a,c,e) Matter power spectra of the concordance ΛCDM (dot-dashed red line) and the dark energy model (solid blue line) with EoS parameter $w = -0.8$ (a), $w = -0.5$ (c), and $w = -0.1$ (e). The dashed line correspond to the numerical (CMBFAST) solution and the (blue) solid line corresponds to the approximated spectrum derived using eq. (9.13). All other cosmological parameters are the same as in the ΛCDM concordance model: $H_0 = 71$ km/s/Mpc, $\Omega_m = 0.27$, $\Omega_\Lambda = \Omega_X = 0.73$, and $n = 1$. (b,d,f) Ratios between different matter power spectra: $P_{\Lambda CDM}(k)/P_X(k)$ (dot-dashed black line), and $P_{X,approx}(k)/P_X(k)$ (solid blue line). Panel (b) corresponds to $w = -0.8$, (d) to $w = -0.5$, and (f) to $w = -0.1$.

tion is to construct the matter power spectrum of an arbitrary dark energy model. The closer the model parameters are to the matter power spectrum used as a starting point (in the examples above, the ΛCDM model), the more accurate the approximation is. Once the dark energy model parameters differ significantly, our approach is not so accurate but, at the same time, the power spectrum of the dark energy model separates from the concordance model. Therefore, as long as the concordance model is a good fit to the data, the difference between this model and the exact/approximated dark energy spectrum are so large (almost a factor 30 in the $w = -0.1$ case) that the uncertainty of our approximation is irrelevant. Large scale structure data like CMB temperature anisotropies on large scales would certainly rule out the $w = -0.1$ model, even allowing for a 50% uncertainty in the matter power spectrum at all scales. The $w = -0.5$ spectrum is identical to ΛCDM at small scales, but different enough at large scales as to expect that CMB temperature anisotropies on large angular scales could rule out the model. For $w = -0.8$, the approximate spectrum is so close to that of ΛCDM that to discriminate it from the concordance model will require background tests such as SN Ia, BAO, etc. (even if we consider the exact matter power spectrum). As determined by Larson *et al.* [138], WMAP 7yrs data alone yields $w = -1.12^{+0.42}_{-0.43}$ at 1σ, while including data on BAO and high redshift supernova produces $w = -0.980 \pm 0.053$ [70]. Here lies the main advantage of our approach: one can quickly construct an approximate power spectrum for any dark energy model that is more appealing from the theoretical point of view than the ΛCDM concordance model. When the model agrees with the data at the background level, if the matter power spectrum is very different from ΛCDM, it will not fit the observations of galaxy clustering and LSS.

9.4 The Radiation Power Spectrum

After computing the dark energy power spectrum, constraints on the model can be imposed using data on galaxy clustering and LSS. Since the spectral shape at small scales is the same than in the ΛCDM, once the dark energy model is normalized to the measured σ_8, it will reproduce the data on small scales (galaxy clustering, peculiar velocity amplitude, weak lensing convergence spectrum, etc.) as well as the ΛCDM. Of the three models discussed in Fig. 9.2, we shall restrict our analysis to $w = -0.5$ dark energy model. As shown in Figure 9.1, horizon size and perturbation growth between $w = -0.5$ dark energy and ΛCDM start to differ at $z \simeq 20$ and the power spectrum at

$k \leq 4 \times 10^{-3} h/\mathrm{Mpc}$ (see Fig. 9.2c), scale that comes into the horizon well in the matter era. The differences in the matter power spectrum can only be tested using data on large scales, like CMB temperature anisotropies.

Prior to decoupling, baryon and photons are tightly coupled and inhomogeneities in the baryon distribution are also reflected in anisotropies on the radiation field. Several physical mechanisms contribute to the generation of temperature anisotropies [65, 67]. Analytic methods that trace the structure of the cosmic microwave background anisotropies have been used to compute the contribution of different effects such as gravitational redshifts, acoustic oscillations, diffusion damping, Doppler shifts, reionization as well as the effect of curvature, a cosmological constant and their dependence on initial conditions [79]. The gravitational redshifts are the dominant contribution on large scales. These anisotropies are strongly dependent on the underlying matter power spectrum. At $l \leq 10$, the largest contributions come from the SW and ISW effects [66]. Both components can be accurately computed in terms of quadratures involving only the matter power spectrum

$$C_l^{SW} = \frac{\Omega_m^2 H_0^4}{2\pi D_+^2(0)} \int_0^\infty k^2 dk \frac{P(k)}{k^4} j_l^2(kr(z))\,, \qquad C_l^{ISW} = \frac{2}{\pi} \int_0^\infty k^2 dk P(k) I_l^2(k)\,, \tag{9.14}$$

where $I_l(k) = 3\Omega_{M,0} \frac{H_0^2}{c^2 k^2} \int_0^{z_{rec}} dz j_l(kr(z))(d[(1+z)D_+]/dz)$. In these expressions j_l is the spherical Bessel function, $r(z) = \int_0^z H^{-1}(z)dz$ the look-back distance and $\Omega_{CDM\,0}$ the current matter density in units of the critical density and D_+ is the growth factor that verifies $D_+(z) = (1+z)^{-1}$ well in the matter dominated period, so during that epoch there is no significant ISW effect. The total radiation spectrum would contain contributions such as acoustic oscillations and Doppler shifts, so $C_l \geq C_l^{SW} + C_l^{ISW}$. The accuracy of Eq. (9.14) could be improved by including more contributions as discussed in [78, 143] but, as we will see below, the difference in the amplitude of the low multipoles suffices to rule out the $w = -0.5$ model so the current approximation is accurate enough for our purposes. In Fig. 9.3a, the thin (blue) solid and dashed lines represent the radiation spectra of the dark energy and ΛCDM models, respectively, computed using CMBFAST. The models are normalized to the σ_8 obtained from the code, $\sigma_8 = 0.80$ for ΛCDM and $\sigma_8 = 0.53$ for the $w = -0.5$ dark energy model. The thick (red) solid line represents the power spectra computed using Eq. (9.14) and the dot-dashed (green) line the radiation spectra computed with the same equation but with the approximated matter power spectra. All matter power spectra are normalized to $\sigma_8 = 0.801$ [138]. The open squares correspond to the binned power spectrum measured by WMAP 7 yrs data [144]; error bars

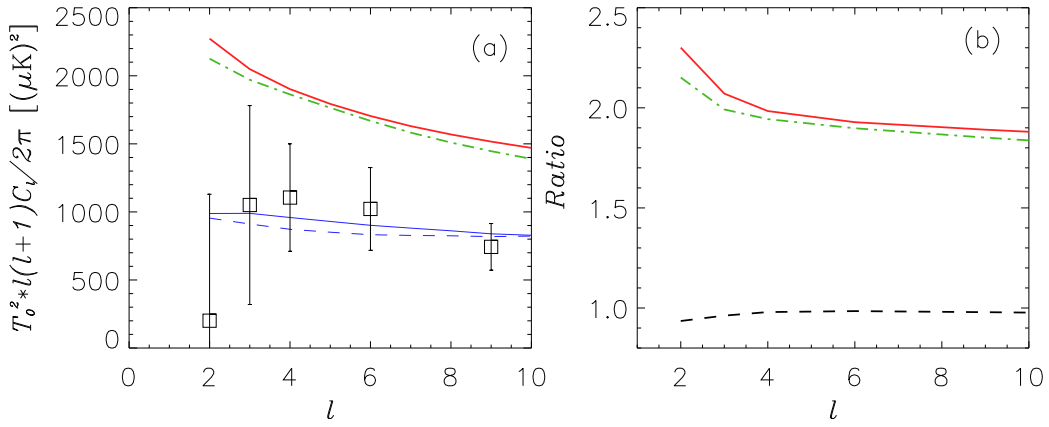

Figure 9.3: (a) Power spectra of the CMB temperature anisotropies. Thin dashed (blue) and solid (blue) lines represent the exact spectrum of the ΛCDM model (with $\sigma_8 = 0.801$) and dark energy model ($\sigma_8 = 0.53$), respectively. Thick (red) solid and dot-dashed (green) lines plot multipoles computed using eq. (9.14) with the exact and approximated matter power spectrum, both normalized to $\sigma_8 = 0.801$. The data are WMAP 7yrs measurements. (b) $C_{l,X,eq}$ 9.14$/C_{l,X,CMBFAST}$ using eq. (9.14) and the exact and approximated matter spectra, solid (red) and dot-dashed (green) lines respectively. The dashed (black) line represents the ratio of the previous two.

include instrumental noise and cosmic variance. To facilitate the comparison between the different approximations, the top two lines in Fig. 9.3b represent the ratio of the dark energy approximated (computed using Eq. (9.14) and the exact matter power spectrum) to the exact dark energy radiation spectrum (solid red line), and the dark energy (using also the approximated matter power spectrum), to the same exact dark energy radiation spectrum (dot-dashed green line). The dashed (black) line is the ratio of the previous two. The error introduced by computing C_l using Eq. (9.14) with the exact or the approximated matter power spectrum is smaller than 10%.

Fig. 9.3 summarizes the comparison of the $w = -0.5$ dark energy model with CMB data. When CMB anisotropies are computed using CMBFAST

and normalized to WMAP 7 yrs data, the CMB power spectrum fits the low multipoles rather well, but then the amplitude of matter density fluctuations is $\sigma_{8,X} = 0.53$, well outside the value $\sigma_8 = 0.801 \pm 0.030$ [138] allowed by the data. As a result, the $w = -0.5$ dark energy model with parameters $\Omega_M = 0.27$, $\Omega_\Lambda = 0.73$, etc. is ruled out. But if the calculation of the CMB power spectrum proves to be difficult, the approximated power spectrum could be used to approach the problem differently. Once the power spectrum of the dark energy model (with $w = -0.5$) is constructed and normalized to $\sigma_8 = 0.801$, the amplitude of temperature anisotropies at $l \leq 10$ would result $l(l+1)C_l^X/2\pi \sim 2000(\mu K)^2$, about a factor of 2 larger than the measured spectrum, a factor larger than the uncertainties introduced by our approximation (less than 10%) or by Eq. (9.14) (less than 15% for $l \leq 10$). Therefore, without the need of further information, a model like dark energy with $w = -0.5$ could be ruled out based on the amplitude of the low order multipoles. Models that differ from ΛCDM also during the radiation regime can be more severely constrained by using weak lensing, peculiar velocities, or galaxy clustering data.

9.5 Conclusions

We have shown in this chapter how to compute the matter power spectrum of dark energy cosmological models using a fiducial ΛCDM model and the growth factor of subhorizon density perturbations of the model under consideration. This allows to use data on CMB temperature anisotropies and galaxy clustering to discriminate models without having to solve the evolution of density perturbations of all matter components, thus economizing much effort. Figure 9.2 shows the advantage of our proposal. In most cosmological models, the equations describing the time evolution of matter density perturbations can be derived from the conservation of the energy momentum tensor and solved for each component individually. Thus, an approximated matter power spectrum can be easily computed. If a model fits the background evolution as determined, for example, by luminosity distances obtained from supernovae data, before proceeding to a detailed study of the evolution of its density perturbations and CMB anisotropies, one can compute an approximated matter power spectrum and predict observables such as the low multipoles of the CMB, the ISW-LSS correlation, the weak lensing convergence spectrum, etc., that can be compared with observations. Even if a model agrees with the data on the expansion rate of the Universe, it could be ruled out by data on temperature anisotropies or galaxy clus-

tering without requiring to solve the first order perturbation equations in full.

Our method has its limitations: it produces an approximated matter power spectrum and only observables derived from it can be used. Since it fixes amplitudes at horizon crossing, it is insensitive to any instability that could occur on superhorizon scales such as those present in some models with interactions in the dark sector [145, 56]. However, as our examples show, the approximated and numerical power spectra are very similar when the model parameters are close to those of the starting model. This is the advantage of our approach: the approximated power spectrum can be used to distinguishing models, that despite reproducing the background observational data, would fail to fit the galaxy clustering and LSS data. In this respect, the $w = -0.8$ model is so close to ΛCDM it should be tested with background data such as SN Ia, BAO etc. to be ruled out (the same happens with the exact matter power spectrum). In the $w = -0.5$ dark energy model, the relative error in the approximated and numerical $P(k)$ is smaller than 8%, but the difference with the concordance model is so significant that the predicted CMB temperature anisotropies on large scales are about a factor of 2 larger than the measurements, a factor much larger than the uncertainty introduced by our approximation or by Eq. (9.14). Finally, the $w = -0.1$ is so different from ΛCDM that it can be ruled out at a glance, irrespectively of the poorer quality of our approximation. When the observables derived from the approximated matter power spectrum fails to fit the data, we can confidently expect the model to fail. But even if a model fits some data on galaxy clustering, it may not necessarily reproduce all the observations, like the full spectrum of CMB temperature anisotropies; it simply means that it deserves further study.

Chapter 10

Three thermodynamically-based parameterizations of the deceleration parameter [1]

10.1 Introduction

The deceleration parameter (2.19), is a key quantity in describing the evolution of the homogeneous and isotropic universe. Its importance lies in the fact that it tells us the rate at which the Universe accelerates or decelerates its expansion. Unfortunately, at present measurements of q suffer from non-small uncertainties that quickly grow with redshift, though it is virtually certain that the Universe is accelerating nowadays, i.e., that $q_0 < 0$ (the zero subscript means present time). Expressions of $q(z)$ provided by cosmological models are of not much help either because none of them rests on sufficiently convincing theoretical grounds. It is to be hoped that things will eventually turn for the better when a successful theory of quantum gravity is in place, though it may well take a long while.

Nevertheless, on the observational side the situation may improve comparatively soon given the variety and range of ongoing and planned major ambitious projects that involve bigger telescopes and advanced techniques -for a short review and a comprehensive list of references see §14 of [147]. In view of the above, it seems reasonable to propose parametrized expressions

[1] This Chapter corresponds to Ref. [146].

of $q(z)$ based not in any specific cosmological model but on practical and empirical reasons that lessen their wide latitude. They can be useful while we patiently wait for a theoretically sound model backed by observation at all scales.

Thus far, different parametrizations, such as $q = q_0 + q_1 z$, $q = q_0 + q_1 z(1+z)^{-1}$, $q = q_1 + q_2 z(1+z)^{-2}$, $q = 1/2 + q_1(1+z)^{-2}$, $q = 1/2 + (q_1 z + q_2)(1+z)^{-2}$, and more complex than these, have been considered in the literature to reconstruct $q(z)$ from observational data (see e.g. [148]-[153]). However, the first parametrization is adequate for $\mid z \mid \ll 1$ only and the others are unsuitable to predict the behavior of the deceleration parameter in the far future; in particular, they diverge as $z \to -1$. Parametrizations whose intended range of validity includes the far future are necessarily more involved and usually contain three or four free parameters [154, 155].

In this paper we propose three model independent parametrizations, with just two free parameters, valid from the matter dominated epoch ($z \gg 1$) onwards (i.e., up to $z = -1$), based on practical and theoretical reasons and independent of any cosmological model. By construction they obey the asymptotic conditions, $q(z \gg 1) = 1/2$, $q(z = -1) = -1$, and a further condition, $dq/dz > 0$, which is valid at least when $q \to -1$. The first condition expresses the conviction that at sufficiently high redshift the Universe was matter dominated (otherwise it would be very hard to account for the observed cosmic structures). At first sight, the other conditions are less compelling. As explained below, they are based on the second law of thermodynamics when account is made of the entropy of the apparent horizon. Usually one parametrizes a function in any specific interval by interpolating it between two given points (one at either end of the interval), modulo one first knows the value taken by the function at these two points. In actual fact, the parametrizations of $q(z)$ proposed so far have just one fixed point: the asymptotic value at high redshift (q must converge to $1/2$ when $z \gg 1$). The other, q_0, is not in reality a fixed point because the value of the deceleration parameter at $z = 0$ is not very well known and therefore left free. The parametrizations proposed in this paper have two fixed points, one at the far past ($z \gg 1$), and other at the far future ($z = -1$). The second fixed point conforms to the thermodynamical constraints imposed by the second law. We believe this means a clear advantage over previous parametrizations of $q(z)$, with just one fixed point. While it can be found in the literature parameterizations that also fix q at $z = -1$ they do so arbitrarily, i.e., not grounded on sound physics.

Here are proposed three model-independent parametrizations of $q(z)$, from $z \gg 1$ up to $z = -1$, that comply with the second law of thermody-

namics and constrain their two free parameters with recent observational data. As it turns out, all of them predict that the present stage of accelerated expansion will never slow down and are consistent with the spatially flat ΛCDM model.

10.2 Thermodynamical constraints on $q(z)$

As is well known, physical systems tend spontaneously to some equilibrium state compatible with the constraints imposed on them. This summarizes the empirical basis of the second law of thermodynamics. Very briefly, this law establishes that isolated, macroscopic systems, evolve to the maximum entropy state consistent with their constraints [156]. As a consequence their entropy, S, cannot decrease at any time, i.e., $dS \geq 0$. Further, in the last phase of the evolution S has to be a convex function of the said variable, $d^2S(z \to -1) < 0$.

Arguably, the entropy of Friedmann-Lemaître-Robertson-Walker (FLRW) universes is dominated by the entropy of the causal horizon, at least at late times -see e.g. [157]. As causal horizon we shall take the apparent horizon, the marginally trapped surface with vanishing expansion of radius $\tilde{r}_A = 1/\sqrt{H^2 + k\,a^{-2}}$ [158], where k denotes the spatial curvature index. Interestingly enough, it has been shown that this horizon represents the appropriate thermodynamic boundary surface [159]. Leaving aside possible quantum corrections its entropy results proportional to area of the latter $(4\pi\tilde{r}_A^2)$ [158],

$$S_A \propto \mathcal{A} = 4\pi\,(H^2 + k\,a^{-2})^{-1}\,. \tag{10.1}$$

Therefore, so long as we can ignore the entropy within the horizon, the second law of thermodynamics imposes $\mathcal{A}' \geq 0$, at any time, as well as $\mathcal{A}'' \leq 0$ at late times -the prime meaning derivative with respect to the scale factor. Both conditions are to be fulfilled if the FLRW universe is to tend to thermodynamic equilibrium at late times [160].

Bearing in mind the definition of the deceleration parameter, for spatially flat ($k = 0$) FLRW universes we can write

$$\mathcal{A}' = 2\mathcal{A}\,\frac{1+q}{a}\,, \qquad \text{and} \qquad \mathcal{A}'' = 2\mathcal{A}\,\left[2\left(\frac{1+q}{a}\right)^2 + \frac{q'}{a} - 2\,\frac{1+q}{a^2}\right]\,. \tag{10.2}$$

The first equation implies $q \geq -1$. Inspection of the second one reveals that when $a \to \infty$ the middle term in the square parenthesis dominates. Thereby,

$dq/da < 0$ in that limit. Thus, for the Universe to tend to thermodynamic equilibrium at late times we must have $q \to -1$ and $dq/dz > 0$ as $z \to -1$.

10.3 Statistical tools

This Section outlines the use of the observational data to fit the parametrizations of the deceleration parameter, $q(z)$. Since the likelihood function is defined by $\mathcal{L} \propto \exp(-\chi^2/2)$ the best fit to the data follows from minimizing the sum $\chi^2_{\rm total} = \chi^2_{SN} + \chi^2_{BAO/CMB} + \chi^2_H$. As detailed below, the best fit values of the parameters can be obtained by contrasting the proposed parametrizations with the empirical data mentioned above and minimizing the $\chi^2_{\rm total}$ by means of the Markov Chain Monte Carlo method.

10.3.1 SN Ia

We compare the theoretical distance modulus with the observed distance modulus $\mu_{obs}(z_i)$ of the 557 supernovae type Ia assembled in the Union2 compilation [60].

10.3.2 BAO and CMB

Here we use the peaks measured at $z = 0.35$ [83] and at $z = 0.2$ [84], together with more recently observed ones: at $z = 0.278$ (with the SDSS [85]), at $z = 0.106$ (in the six degree Field Galaxy Redshift Survey [86]), and at $z = 0.44$, $z = 0.60$, and $z = 0.73$ (by the WiggleZ team [87]).
From each peak the ratio of the comoving sound horizon $r_s(z)$ at decoupling ($z = z_\star \simeq 1090$) and at the drag epoch ($z = z_d$), the epoch at which the acoustic oscillations are frozen in, can be measured. Here c_s is the speed of sound. Likewise, at each peak, a characteristic distance scale, the dilation scale, eq. (4.14), can also be determined. To compute the drag epoch redshift we use the formula (4) of Eisenstein and Hu in [161] and get $z_d \approx 1020$. Multiplying the ratio, $\frac{r_s(z_d)}{D_V(z_{BAO})}$, taken from the BAO peaks by the acoustic scale (4.4), we get $\frac{d_A(z_\star)}{D_V(z_{BAO})}\frac{r_s(z_d)}{r_s(z_\star)}$ at each redshift of the seven BAO data. Here we use the value for l_A derived from Wilkinson microwave anisotropy probe (WMAP)7-years data, namely, $l_A = 302.09 \pm 0.76$ [70]. If we also use the value of the ratio of sound horizon at the drag epoch and at recombination (redshift $z_\star$), computed from the values reported in [70] $\frac{r_s(z_d)}{r_s(z_\star)} = 1.045 \pm 0.015$ we obtain the new estimator $\frac{d_A(z_\star)}{D_V(z_{BAO})}$, shown in table 10.1, as done in [72]. Using this estimator, the dependence in the sound

horizons at decoupling and the drag epoch is suppressed. Thus we just use the ratio between them, which is almost model independent. This follows because both redshifts are rather close and the sound horizon at decoupling and drag essentially depend on the fractional difference between the number of photons and baryons [72]. To obtain the χ^2 for the combined BAO/CMB

z_{BAO}	0.106	0.2	0.278	0.35	0.44	0.6	0.73
$\frac{r_s(z_d)}{D_V(z_{BAO})}$	0.336 ± 0.015	0.1905 ± 0.0061	0.1394 ± 0.0049	0.1097 ± 0.0036	0.0916 ± 0.0071	0.0726 ± 0.034	0.0592 ± 0.0032
$\frac{d_A(z_\star)}{D_V(z_{BAO})}$	30.92 ± 1.45	17.53 ± 0.62	12.83 ± 0.49	10.09 ± 0.36	8.43 ± 0.66	6.68 ± 0.33	5.45 ± 0.30

Table 10.1: Values of $\frac{r_s(z_d)}{D_V(z_{BAO})}$ (reported in [83, 84, 86, 85, 87]) and the derived ratio $\frac{d_A(z_\star)}{D_V(z_{BAO})}$.

data we compute

$$\chi^2_{BAO/CMB} = \mathbf{X}^T \mathbf{C}^{-1} \mathbf{X}\,, \tag{10.3}$$

where

$$\mathbf{X} = \begin{pmatrix} \frac{d_A(z_\star)}{D_V(0.106)} - 30.92 \\ \frac{d_A(z_\star)}{D_V(0.2)} - 17.53 \\ \frac{d_A(z_\star)}{D_V(0.278)} - 12.83 \\ \frac{d_A(z_\star)}{D_V(0.35)} - 10.09 \\ \frac{d_A(z_\star)}{D_V(0.44)} - 8.43 \\ \frac{d_A(z_\star)}{D_V(0.6)} - 6.68 \\ \frac{d_A(z_\star)}{D_V(0.73)} - 5.45 \end{pmatrix}$$

and $\mathbf{X}^T$ the transpose matrix. The elements of covariance matrix $\mathbf{C}$ are given by

$$\mathbf{C}_{ij} = \sum_k \left(\frac{\partial \frac{d_A(z_\star)}{D_V(z)}}{\partial p_k} \right)_{z_i} \left(\frac{\partial \frac{d_A(z_\star)}{D_V(z)}}{\partial p_k} \right)_{z_j} \mathbf{C}_{p_k\, i\, j}\,, \tag{10.4}$$

where the sum is over the estimators used (in our case, $\frac{r_s(z_d)}{D_V(z_{BAO})}$, l_A/π and $\frac{r_s(z_d)}{r_s(z_\star)}$). The elements of the original covariance matrices are $\mathbf{C}_{\frac{l_A}{\pi}} = \theta^2_{\frac{l_A}{\pi}}$, $\mathbf{C}_{\frac{r_s(z_d)}{r_s(z_\star)}} = \theta^2_{\frac{r_s(z_d)}{r_s(z_\star)}}$ and $\mathbf{C}_{BAO\, i\, j} = \theta_{BAO\, i}\ \theta_{BAO\, j}\ r_{i\, j}$ where $\theta_{BAO\, i}$ stand for the errors associated with the estimator $\frac{r_s(z_d)}{D_V(z_i)}$. The only non-zero off-diagonal correlation coefficients $r_{i\, j}$ are $r_{z=0.2\, z=0.35} = 0.337$, $r_{z=0.44\, z=0.6} = 0.369$ and $r_{z=0.6\, z=0.73} = 0.438$, and their symmetric [84, 87]. Thus, the

inverse covariance matrix comes to be

$$\mathbf{C}^{-1} = \begin{pmatrix} 0.492 & -0.084 & -0.126 & -0.136 & -0.025 & -0.081 & -0.088 \\ -0.084 & 3.362 & -0.327 & -2.397 & -0.065 & -0.209 & -0.228 \\ -0.126 & -0.327 & 4.429 & -0.528 & -0.098 & -0.314 & -0.342 \\ -0.136 & -2.397 & -0.528 & 9.712 & -0.106 & -0.338 & -0.368 \\ -0.025 & -0.065 & -0.098 & -0.106 & 2.798 & -2.749 & 1.182 \\ -0.081 & -0.209 & -0.314 & -0.338 & -2.749 & 15.002 & -7.294 \\ -0.088 & -0.228 & -0.342 & -0.368 & 1.182 & -7.294 & 14.587 \end{pmatrix} .$$

10.3.3 History of the Hubble parameter

In addition to the data used in §5.2.5 and §7.3.5, we have included in our analysis 9 more recent correlated data from the WiggleZ survey [162]. The corresponding χ^2

$$\chi^2_H(\mathbf{p}) = \sum_{i=1}^{15} \frac{[H_{th}(z_i) - H_{obs}(z_i)]^2}{\sigma^2(z_i)} + \mathbf{X}_H^T \mathbf{C}_H^{-1} \mathbf{X}_H \ , \qquad (10.5)$$

where

$$\mathbf{X}_H = \begin{pmatrix} H_{th}(0.05) - 69.4 \\ H_{th}(0.15) - 76.6 \\ H_{th}(0.25) - 75.3 \\ H_{th}(0.35) - 78.3 \\ H_{th}(0.45) - 87.3 \\ H_{th}(0.55) - 88.9 \\ H_{th}(0.65) - 101.4 \\ H_{th}(0.75) - 96.9 \\ H_{th}(0.85) - 127.3 \end{pmatrix}$$

and $\mathbf{C}_H^{-1}$ is the inverse covariance matrix given in table 6 of [162].

10.4 Parametrizations

Here we propose and constrain three parametrizations of the deceleration parameter, valid from the matter dominated era up to $z = -1$. These fulfill: (i) $q(z \gg 1) = 1/2$ (as demanded by cosmic structure formation), (ii) $q(z = -1) = -1$ and $dq(z)/dz > 0$ when $q(z) \to -1$ as required by the thermodynamic arguments above (the second law of thermodynamics). In interpolating between $(z = -1,\ q = -1)$ and $(z \gg 1,\ q = 1/2)$ we introduce two free parameters q_1 and q_2 and fit them to the observational sets of data

by the method of last Section. Note that due to the scarcity of $q(z)$ data and their big error bars, we do not constrain the parametrizations directly. We constrain instead the expressions for $H(z)$ that arise from integrating them; namely,

$$H(z) = H_0 \exp\left\{\int_0^z [1+q(x)]\, d\ln(1+x)\right\}, \tag{10.6}$$

which holds for all parametrizations. This has the advantage of a much bigger and robust statistics. Notice that the Hubble constant also enters this expression as a free parameter. Its value for each parametrization is obtained by fitting it to the $H(z)$ data, [95, 96, 97, 98, 162].

10.4.1 Parametrization I

As a first parametrization we propose

$$q(z) = -1 + \frac{3}{2}\left(\frac{(1+z)^{q_2}}{q_1+(1+z)^{q_2}}\right), \tag{10.7}$$

where to avoid divergences q_1 and q_2 must be positive-definite. Introducing (10.7) in (10.6), it follows

$$H(z) = H_0\left(\frac{q_1+(1+z)^{q_2}}{q_1+1}\right)^{\frac{3}{2q_2}}. \tag{10.8}$$

(We note in passing that for $q_2 = 3$ the ΛCDM behavior is reproduced). By using the method outlined in last section in conjunction with the observational data (SN Ia (557), CMB/BAO (7) and $H(z)$ (15)), we fit the three free parameters occurring in (10.8). The result is $q_1 = 2.87^{+0.70}_{-0.53}$, $q_2 = 3.27\pm0.55$, and $H_0 = 70.5^{+1.5}_{-1.6}$ km/s/Mpc. Table 10.2 shows the χ^2 values of the best fit.

Data sets	χ^2_{SN}	$\chi^2_{BAO/CMB}$	χ^2_H	$\chi^2_{\rm tot}$	$\chi^2_{{\rm tot}\ dof}$
Union2+BAO/CMB+H(z)	542.6	2.6	17.9	563.3	0.96

Table 10.2: Best fit χ^2 values of parametrization I, Eq. (10.7). The free parameters are q_1, q_2 and H_0.

Figure 10.1 shows the evolution of the q for the best fit values of parametrization I (solid line), with its 1σ confidence region (shadowed area), and the spatially flat ΛCDM model (dashed line) as determined by the WMAP 7-years team [70] (the latter graph is included for the sake of comparison), in

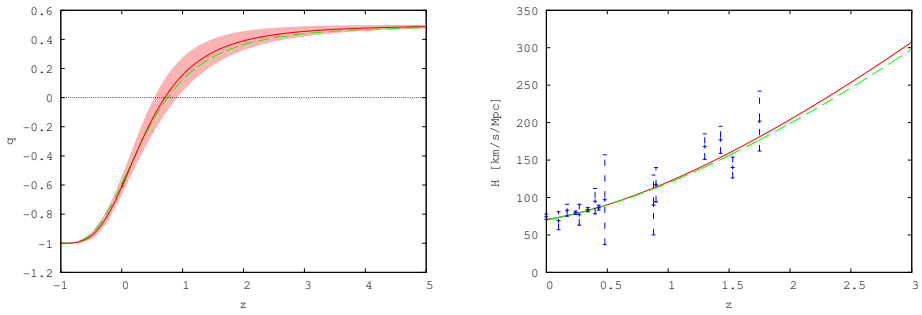

Figure 10.1: Left panel: deceleration parameter vs. redshift. The shaded area shows the 1σ confidence region. Right panel: Hubble function vs. redshift (the observational data are borrowed from Refs. [95, 96, 97, 98]). In both panels the solid (red) and the dashed (green) lines are used for the best fit of parametrization I (Eq. (10.7)) and for the ΛCDM model with $\Omega_{M0} = 0.27$ and $H_0 = 72.1\,\mathrm{km/s/Mpc}$ -see [70]-, respectively. The latter graph is shown for comparison.

the interval $-1 \leq z \leq 5$ (left panel), and the evolution of the Hubble function in the interval $0 \leq z \leq 3$ (right panel). Figure 10.2 depicts the 1σ and 2σ contour plots of the pairs $(q_1,\, q_2)$ (left panel) and $(H_0,\, q_0)$ (right panel). Upon assuming that the expansion is dominated by pressureless matter and

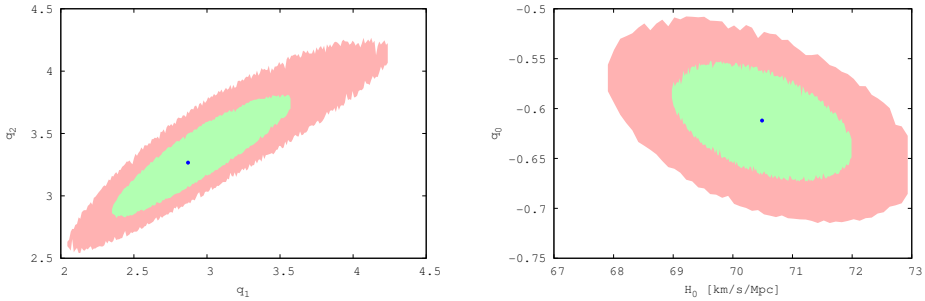

Figure 10.2: Left panel: 1σ and 2σ confidence regions of the pair of free parameters (q_1, q_2) of parametrization I, Eq. (10.7). Right panel: 1σ and 2σ regions of the pair of free parameters (H_0, q_0). The dot signals the best fit values.

some other (unspecified) component, non-interacting with each other except gravitationally, the effective EoS parameter is given by

$$w(z) = \frac{2q(z) - 1}{3(1 - \Omega_M(z))}\,. \tag{10.9}$$

Parametrizations of $q(z)$ and $w(z)$ are somewhat equivalent but not quite because in the latter case some assumptions about the energy budget of the Universe, as well on the existence or not of possible interactions between the different components, have to be made while in the former (as in our case) not necessarily. Having said this, it is interesting to confront (10.9) with the widely used Chevallier-Polarsky-Linder (CPL) parametrization [163, 164]

$$w = w_0 + w_1 \frac{z}{1+z}\,, \tag{10.10}$$

not far from $z = 0$, in the redshift range $-0.3 \leq z \leq 0.3$. We restrict ourselves to comparative small redshift around $z = 0$ because it diverges at $z \to -1$. After numerically linearizing our expression for $w(z)$ we get $w_0 = -0.92 \pm 0.10$ and $w_1 = 0.31^{+0.28}_{-0.25}$, values in very good agreement with those reported in [70], for the CPL parameters, namely: $w_0 = -0.93 \pm 0.12$ and $w_1 = -0.38^{+0.66}_{-0.65}$. As Fig. 10.3 reveals, comparison in the extended interval $-0.5 \leq z \leq 5$ shows that for $z \geq 2.5$ the evolution of the effective of both EoS disagree in excess of 1σ. This is consistent with claims that the CPL parametrization is not appropriate to fit data simultaneously at low and high redshifts [165, 166].

10.4.2 Parametrization II

As a second parametrization we propose,

$$q(z) = -\frac{1}{4}\left(3q_1 + 1 - 3(q_1+1)\frac{q_1 e^{q_2(1+z)} - e^{-q_2(1+z)}}{q_1 e^{q_2(1+z)} + e^{-q_2(1+z)}}\right)\,. \tag{10.11}$$

In this case the Hubble function must be obtained by numerically integrating Eq. (10.6). Proceeding as before we obtain, $q_1 = 0.078^{+0.086}_{-0.043}$, $q_2 = 0.95^{+0.23}_{-0.20}$, and $H_0 = 70.4 \pm 1.6$ km/s/Mpc for the three parameters entering $H(z)$. The χ^2 best fit values are shown in table 10.3.

Left panel of Fig. 10.4 shows the evolution of q for the best fit value of parametrization II (with its 1σ confidence region) and the ΛCDM model obtained by Komatsu *et al.* [70]. The right panel depicts the evolution of the Hubble function versus redshift in the interval $0 \leq z \leq 3$.

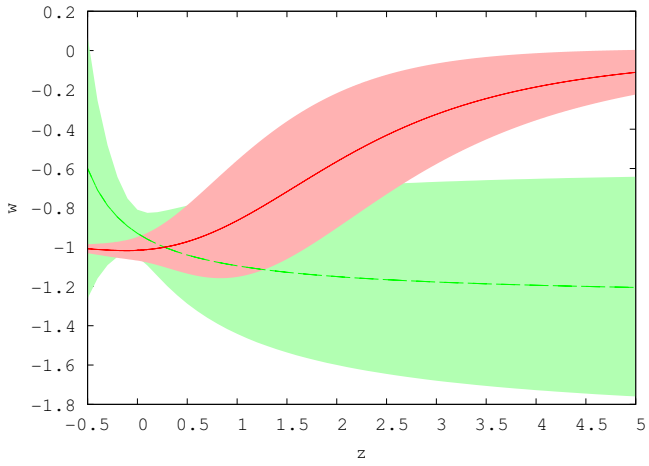

Figure 10.3: EoS parameters vs. redshift. The shaded area shows the 1σ confidence region. The solid (red) and the dashed (green) lines are used for the best fit of parametrization I (Eq. (10.7)) and for the CPL parameterization, Eq. (10.10), both with $\Omega_{M0} = 0.27 \pm 0.03$. For the CPL parameterization the values $w_0 = -0.93 \pm 0.12$ and $w_1 = -0.38^{+0.66}_{-0.65}$ obtained by Komatsu *et al.* [70] were used.

Data sets	χ^2_{SN}	$\chi^2_{BAO/CMB}$	χ^2_H	$\chi^2_{\rm tot}$	$\chi^2_{\rm tot\ dof}$
Union2+CMB/BAO+H(z)	542.7	2.7	17.7	563.1	0.96

Table 10.3: Same as Table 10.2 but for parametrization II, Eq. (10.11)

.

Figure 10.5 shows the 1σ and 2σ contour plots of the pair (q_1, q_2) (left panel), and (H_0, q_0) (right panel). Note that q_0 results more degenerate than in the previous parametrization (as well as in the next one). This arises because -as direct inspection shows- in the other two parametrizations q_0 depends on just one free parameter, q_1, while in this parametrization it depends on both, q_1 and q_2.

Considering the effective EoS parameter (10.9), as in the previous section, we obtain after linearization $w_0 = -0.97^{+0.33}_{-0.21}$ and $w_1 = -0.15^{+0.70}_{-0.47}$. As Fig. 10.6 shows, the evolution of the said effective EoS and the CPL in an extended redshift interval is similar to the previous one but with the 1σ uncertainty interval significantly wider.

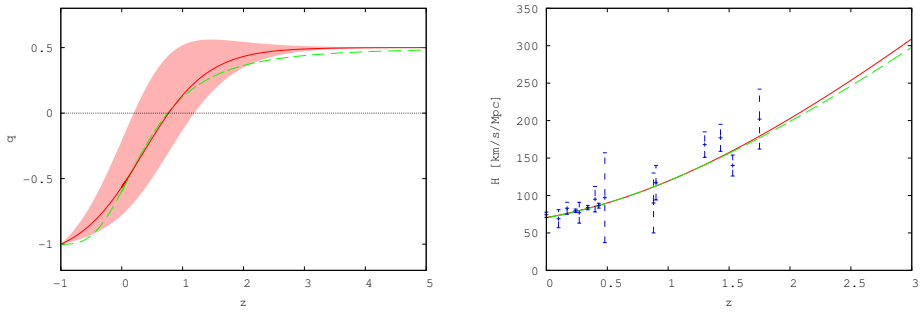

Figure 10.4: Same as Fig. 10.1 but for parametrization II, Eq. (10.11).

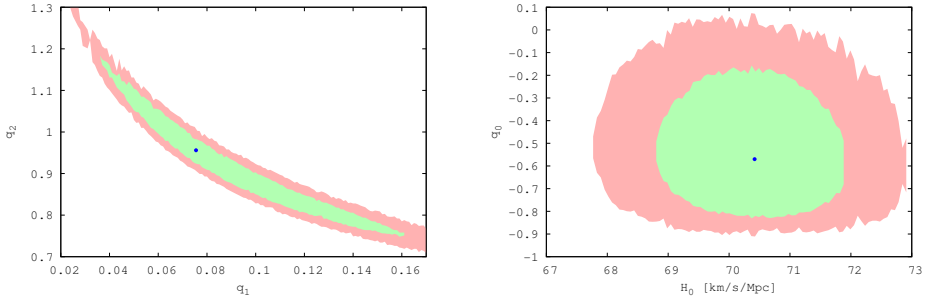

Figure 10.5: Same as Fig. 10.2 but for parametrization II, Eq. (10.11).

10.4.3 Parametrization III

The previous parametrization presents the inconvenience of a significant uncertainty in q_0 since it depends on the two free parameters. The following parametrization

$$q(z) = -\frac{1}{4} + \frac{3}{4}\,\frac{q_1 e^{q_2 \frac{z}{\sqrt{1+z}}} - e^{-q_2 \frac{z}{\sqrt{1+z}}}}{q_1 e^{q_2 \frac{z}{\sqrt{1+z}}} + e^{-q_2 \frac{z}{\sqrt{1+z}}}}\,, \tag{10.12}$$

avoids this as q_0 depends on q_1 only. Again, $H(z)$ must be obtained numerically. Then, proceeding as in the two previous instances, we obtain $q_1 = 0.36^{+0.07}_{-0.08}$, $q_2 = 1.57^{+0.27}_{-0.33}$, and $H_0 = 70.5^{+1.4}_{-1.6}$ km/s/Mpc. The χ^2 values of the best the fit are indicated in table 10.4. Figure 10.7 shows the evolution of the deceleration parameter for the best fit parametrization (with its 1σ confidence region) and the ΛCDM model as determined the WMAP

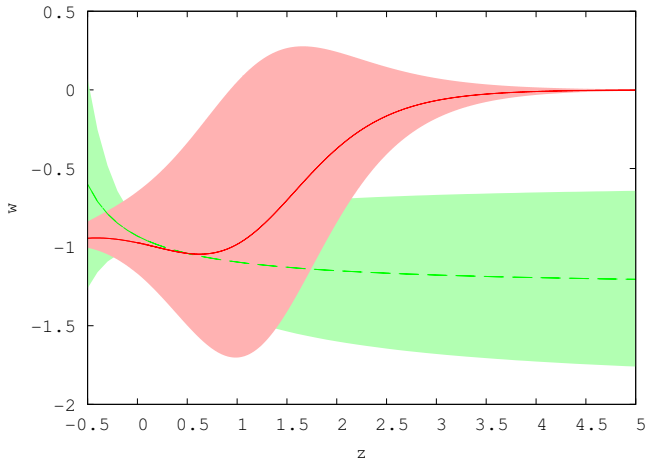

Figure 10.6: EoS parameters vs. redshift. The shaded area shows the 1σ confidence region. The solid (red) and the dashed (green) lines are used for the best fit of parametrization I (Eq. (10.7)) and the CPL parametrization, Eq. (10.10), respectively, both assuming $\Omega_{M0} = 0.27 \pm 0.03$. For the CPL parametrization the values $w_0 = -0.93 \pm 0.12$ and $w_1 = -0.38^{+0.66}_{-0.65}$ obtained by Komatsu *et al.* [70] were used.

Data sets	χ^2_{SN}	$\chi^2_{BAO/CMB}$	χ^2_H	$\chi^2_{\rm tot}$	$\chi^2_{{\rm tot}\ dof}$
Union2+CMB/BAO+H(z)	542.6	1.7	17.9	563.2	0.96

Table 10.4: Same as Table 10.2 but for parametrization III, Eq. (10.12).

team [70] (left panel), and the evolution of the Hubble function (right panel). Fig. 10.8 shows the 1σ and 2σ contour plots of the pairs (q_1, q_2) (left panel) and (H_0, q_0) (right panel). As for the effective EoS parameter (10.9), proceeding as in the previous subsections, we obtain $w_0 = -1.01 \pm 0.06$ and $w_1 = 0.03 \pm 0.16$. Again, the evolution of the said effective EoS and the CPL in an extended redshift interval is rather similar to the one in Fig. 10.3; thereby, we do not feel it necessary to show it here.

10.4.4 Discussion

Figure 10.9 compares the parametrizations. All three yield rather similar results being really close between one another from the statistical standpoint ($\chi^2_{dof} = 0.96$ for all of them). However, parametrization II looks somewhat

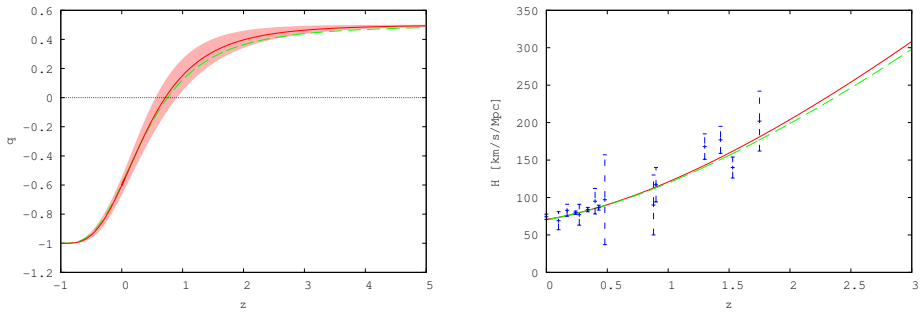

Figure 10.7: Same as Fig. 10.1 but for parametrization III, Eq. (10.12).

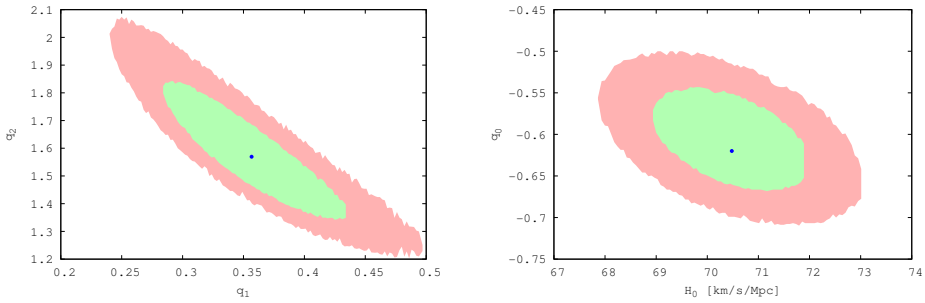

Figure 10.8: Same as Fig. 10.2 but for parametrization III, Eq. (10.12).

less favored than the other two because of the noticeably wider 1σ region of q vs. z, as seen in the left panel of Fig. 10.4.

All of them are consistent with a present stage of accelerated expansion, never to end or slow down. Further, the best fit plots of $H(z)$ and $q(z)$ are alike the corresponding plots of the ΛCDM model as determined by Komatsu *et al.* [70]. From Table 10.5 we learn that all H_0 best fit values are within 1σ of each other and consistent with the H_0 value reported in [70]. The same holds true for the best fits of the age of the Universe, t_0, q_0 and the redshift, z_t, at which the transition deceleration-acceleration occurred (i.e., $q(z_t) = 0$), though the central values of the latter are not so close between each other as the corresponding values of the other two parameters. At any rate, the three of them are consistent with the $z_t \approx 0.5$ value obtained by Wu *et al.* using the history of the strong energy condition [167], as well as

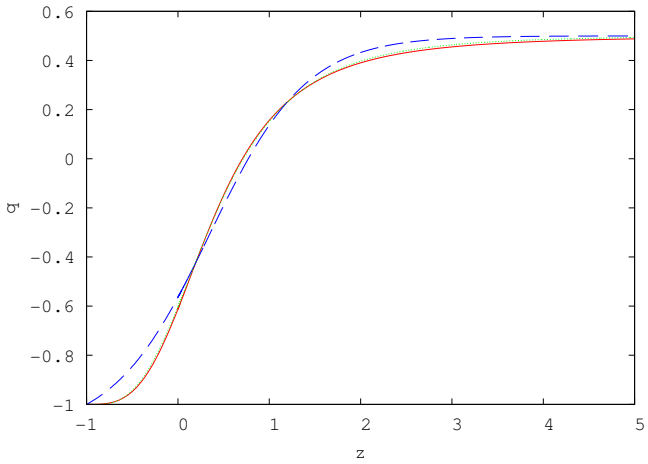

Figure 10.9: Deceleration parameters vs. redshift. Solid (red), long dashed (blue) and short dashed (green) lines are for parametrizations I, II and III respectively. The graphs of parameterizations I and III practically overlap each other.

with the findings of Riess *et al.* [168], Cunha and Lima [150], and Lu *et al.* [169].

As table 10.5 shows, the values predicted for Hubble's constant, H_0, by the three parametrizations are within 1σ between one another and with the value predicted by the ΛCDM model that best fit identical sets of observational data. This is also true for t_0, q_0 and z_t.

	Param. I	Param. II	Param. III	ΛCDM
H_0	$70.5^{+1.5}_{-1.6}$	70.4 ± 1.6	$70.5^{+1.4}_{-1.6}$	70.2 ± 1.4
t_0	13.6 ± 0.5	13.7 ± 0.4	13.6 ± 0.2	13.4 ± 0.1
q_0	$-0.61^{+0.06}_{-0.07}$	$-0.56^{+0.35}_{-0.22}$	-0.60 ± 0.06	-0.60 ± 0.03
z_t	$0.71^{+0.14}_{-0.17}$	$0.77^{+0.52}_{-0.57}$	$0.72^{+0.27}_{-0.21}$	0.76 ± 0.05

Table 10.5: Hubble's constant, H_0 (in km/s/Mpc), the age of the Universe, t_0 (in Gyr), the deceleration parameter, q_0, and the redshift, z_t, of the transition deceleration-acceleration for the three parametrizations, and the flat ΛCDM model fitted to the same data sets.

A direct and model-independent determination of $q(z)$ in the redshift interval $0 \leq z \leq 1$ was carried out by Daly and coworkers [108] who applied

the expression [170]

$$q(z) = -1 \, - \, (1+z) \left[\frac{d^2y/dz^2}{dy/dz} \, + \, \frac{\Omega_{k0}\, y\, dy/dz}{1 \, + \, \Omega_{k0} y^2} \right] \tag{10.13}$$

to the 192 SN I data points of Davis *et al.* [171] and 30 radiogalaxy data points of Daly *et al.* [172] -see Fig. 10 in [108]. In (10.13) $y(z) = H_0(a_0\, r)$ is the dimensionless coordinate distance, r the radial coordinate of the FLRW metric, and $\Omega_{\kappa\, 0} \, = \, -\kappa/(H_0\, a_0)^2$. Notice that it just assumes the FLRW metric; i.e., it holds regardless the energy components of the Universe or the specific theory of gravity adopted. Figure 10.10 shows the best fit graphs of $q(z)$ of each parametrization superimposed to experimental results of Daly *et al.* [108]. As it is seen, these lines fall within the 1σ region of $q(z)$ as determined in Ref. [108].

One may wonder up to what extent the imposing of the thermodynamic-based, far future, constraint $q(z = -1) = -1$ biases the parametrizations toward the ΛCDM model. We have studied this by letting the value of $q(z = -1)$ as an additional free-parameter and fitting it using solely the observational data. The results are: $q(z = -1) = -0.65^{+0.21}_{-0.50}$, $q(z = -1) = -1.1^{+0.2}_{-1.7}$, and $q(z = -1) = -0.82^{+0.07}_{-0.4}$ for parametrizations I, II and III, respectively. Except for the second one, the quintessence cold dark matter (CDM) model is somewhat preferred but, in all the cases, the physically motivated choice $q(z = -1) = -1$ results compatible within 1σ. The drawback of letting $q(z = -1)$ free, aside from violating thermodynamics, is that the other two free-parameters present a wide degeneracy.

Likewise, the derived values for the Hubble constant (first row in Table 10.5) differ from the recently obtained by Riess et al., $H_0 \, = \, 74.2 \, \pm \, 3.6$ km/s/Mpc, [95], who used 240 Cepheids variables at $z \, < \, 0.1$, by about 6% (but they all agree with the latter at 1σ). We have considered this by repeating the analysis of subsection IIIC but this time leaving aside the mentioned value of Riess et al. The results now are: $H_0 \, = \, 70.0^{+1.7}_{-1.5}$, $H_0 = 70.0^{+1.5}_{-1.6}$, and $H_0 = 70.1^{+1.6}_{-1.6}$ Km/s/Mpc for parametrizations I, II and III, respectively. Thus, both sets of results are essentially coincident (they differ by less than 1%). They also agree very well with the Hubble constant value observationally derived by Komatsu et al., 70.4 ± 2.5 km/s/Mpc [70], using WMAP 7-year data. So, while there is a significant difference between the Hubble constant value of Riess et al. and ours, it is not a substantial one; after all, they agree at 1σ confidence level. At any rate, the root of the discrepancy may be rightly traced at the difference in methods employed. While Riess et al. essentially used astrophysical data, we (as well as Komatsu et al.) resorted to cosmological data instead.

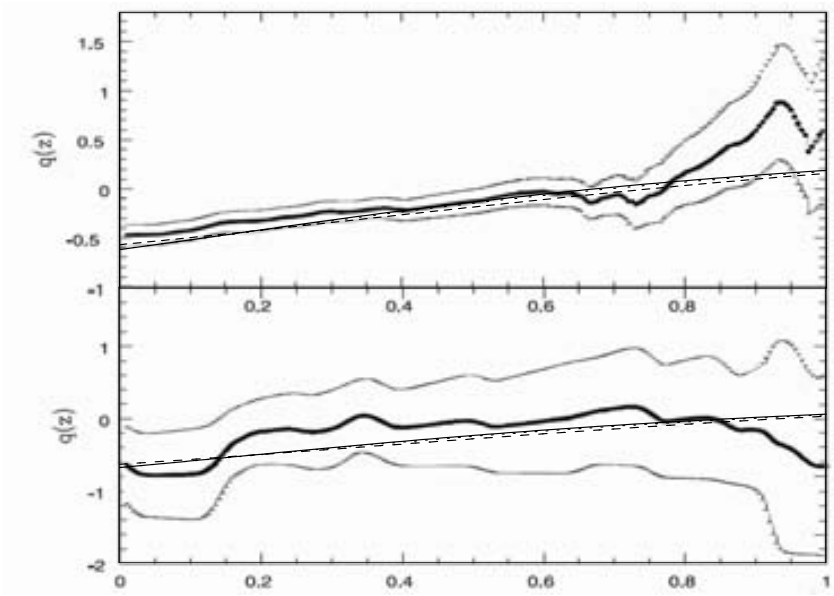

Figure 10.10: Top panel: observational constraints, at 1σ confidence level, on the deceleration parameter versus redshift, obtained by Daly *et al.* using the combined sample 192 supernovae and 30 radio galaxies (top panel of Fig. 10 in [108]); the thick solid line corresponds to the central experimental value of $q(z)$. Solid, dashed, and dot-dashed lines correspond to parametrizations I (Eq. (10.7)), II (Eq. (10.11)) and III (Eq. (10.12)), respectively. Bottom panel: The same as the top panel except that the observational constraints on $q(z)$ were obtained solely from the sample of 30 radio galaxies (bottom panel of Fig. 10 in [108]). In both panels parametrizations I and III practically overlap each other.

10.5 Concluding remarks

In this Chapter we proposed three different two-parameter parametrizations of $q(z)$ valid from the matter era ($z \gg 1$) up to the infinite future ($z = -1$), modulo $H(z) > 0$. These rest in the following hypotheses: (i) at cosmological scales the Universe is homogeneous and isotropic, thereby well described

by the FLRW metric; (*ii*) in the matter dominated era $q = 0.5$; (*iii*) at least at late times the entropy of the Universe is dominated by the entropy of the apparent horizon. The second an third hypotheses furnish two fixed points (at $z \gg 1$ and $z = -1$, respectively), thereby drastically reducing the ample latitude one faces in parameterizing $q(z)$. By smoothly interpolating between these two points one can obtain useful parametrizations, but with shrunk arbitrariness.

Except for the existence of a matter dominated era at early times, the parametrizations are independent on any specific cosmological model; and, on the other hand, they are flexible enough to accommodate many homogeneous and isotropic models. We constrained the free parameters with the latest observational data (SN Ia, BAO, CMB, and $H(z)$). Accordingly if to accommodate a given cosmological model the free parameters, q_1 and q_2, in the three parametrizations should take values widely apart from their respective best fits (which are consistent within 1σ with the flat ΛCDM model), we may confidently discard the said model.

Thermodynamics in spatially flat ($\kappa = 0$) FLRW universes demands that $q(z = -1) = -1$. This provides us with an additional and very useful fixed point to parametrize $q(z)$ in a model independent manner. Note that in the absence of a physically motivated value of the deceleration parameter at $z = -1$ one is led to choose some or other random value. By contrast, in our case we have taken $q(z = -1) = -1$ on solid thermodynamic grounds.

Albeit we have considered just the particular set of spatially flat FLRW universes, it is not a big restriction at all. Indeed, recalling that in the case of non-flat metrics the area of the apparent horizon is given by Eq. (10.1) it follows that $\mathcal{A}' = \mathcal{A}^2/(2\pi a)\,[H^2(1+q) + k\,a^{-2}]$. When $a \to \infty$ and $k = -1$, the last term on the right hand side is necessarily subdominant otherwise one would have $\mathcal{A}' < 0$, contrary to the second law. Hence the condition $\mathcal{A}' \geq 0$ in that limit reduces to the one in flat space, namely, $q \geq -1$. In the positively curved case, and again in the same limit, one can assume that $H \propto a^n$, n being some real number. As it can be straightforwardly checked, the aforementioned last term results, once more, subdominant provided that $n > -1$ which is the case of most realistic cosmologies. Thus, ($z = -1$, $q = -1$) is an asymptotic fixed point not only for spatially flat universes but also for open universes and for a rather ample set of closed universes.

Our results suggest that from the era of matter domination onward q decreases monotonously with expansion (i.e., $dq/dz > 0$), the transition deceleration acceleration occurred at a redshift of about 0.7, and that $q_0 \simeq -0.6$. They do not support recent claims that the cosmic expansion is today reverting to a decelerated phase (i.e., that $dq/dz|_0 < 0$) [166], [173]-[176]. On

the contrary, they show overall consistency with the findings of [148]-[155], [108], [177], as well as with those of Serra *et al.,* [107]. The latter authors showed that the equation of state of dark energy has not varied noticeably in the redshift interval $0 \leq z \leq 1$.

Chapter 11

Overall conclusions

In this Memoir we have dealt with cosmological models of interacting dark energy, especially with those in which the latter is holographic.

- We constrained two different models of holographic interacting dark energy with several cosmological data sets in §5, §7 and §6. In all of them, the non interacting case was discarded at least at 2σ level. When the infrared cutoff is described by the Hubble length it is discarded at 30σ. The result are compatible with the actual value of the cosmological parameters determined by Komatsu and collaborators [70], albeit the ΛCDM model presents a marginally better fit and more statistical power. So, if dark energy is holographic, what is a very reasonable assumption, dark energy and dark matter must interact (also non-gravitationally) with each other.

- Any holographic interacting dark energy model can be recast as a non interacting one endowed with a c^2 parameter that slowly varies with time -see §6. The non interacting models seem to fit the data better, since the best fit models are close to the ΛCDM model.

- We have shown that an equation of state describing the dark sector, can be seen as a unified dark matter model or a cold dark matter plus vacuum energy. The former ones have problems in fitting the data and so far, generally, only models behaving close to the standard ΛCDM model are compatible with current observations. By contrast, the interacting models are compatible with data in spite of departing from the ΛCDM.

- We proposed a novel method to compute the matter power spectrum

in (exotic) dark energy models that save computational time since it suffices to calculate the matter power spectrum of the ΛCDM model and the growth function after recombination of the model under consideration. The errors introduce by the method remain below 8%.

- Many parameterizations of the deceleration parameter (or nearly equivalently the equation of state parameter) diverge in the far future and sometimes at high redshifts. We proposed three different parameterizations, based on thermodynamical arguments, that are well behaved at all times. They also fit the geometric cosmological data and are close to the predictions of the standard ΛCDM model.

Appendix A

A.1 Some geometric quantities associated to the background FLRW metric

The homogeneous and isotropic metric in cosmic time is described by

$$ds^2 = -dt^2 + a^2\gamma_{ij}dx^i dx^j \ , \tag{A.1}$$

and in conformal time by

$$ds^2 = a^2\left(-d\tau^2 + \gamma_{ij}dx^i dx^j\right) \ ; \tag{A.2}$$

where the 3-space metric tensor reads

$$\gamma_{ij} = \begin{pmatrix} \frac{1}{1-kr^2} & 0 & 0 \\ 0 & r^2 & 0 \\ 0 & 0 & r^2\sin^2\theta \end{pmatrix} \ .$$

The Christoffel symbols are defined trough the metric tensor by

$$\Gamma^{\alpha}_{\mu\nu} \equiv \frac{1}{2}g^{\alpha\beta}\left(g_{\beta\nu,\mu} + g_{\mu\beta,\nu} - g_{\mu\nu,\beta}\right). \tag{A.3}$$

Thus, being the metric (A.1) diagonal and g_{00} a constant quantity, we have

$$\Gamma^{0}_{\mu\nu} = -\frac{1}{2}g^{00}g_{\mu\nu,0} = \frac{1}{2}g_{\mu\nu,0} \ . \tag{A.4}$$

Then,

$$\Gamma^{0}_{00} = 0 \qquad \text{and} \qquad \Gamma^{0}_{ij} = \dot{a}a\gamma_{ij} \ . \tag{A.5}$$

All the other Christoffel symbols for the FLRW metric in coordinate as well as in conformal time can be derived in a similar fashion. All of them are

Christoffel symbols

cosmic time t	conformal time τ
$\Gamma^0_{\ 00} = 0$	$\Gamma^0_{\ 00} = \frac{a'}{a}$
$\Gamma^0_{\ i0} = 0$	$\Gamma^0_{\ i0} = 0$
$\Gamma^0_{\ ij} = \dot{a} a \gamma_{ij}$	$\Gamma^0_{\ ij} = \frac{a'}{a}\gamma_{ij}$
$\Gamma^i_{\ 00} = 0$	$\Gamma^i_{\ 00} = 0$
$\Gamma^i_{\ 0j} = \frac{\dot{a}}{a}\delta^i_j$	$\Gamma^i_{\ 0j} = \frac{a'}{a}\delta^i_j$
$\Gamma^i_{\ jk} = {}^s\Gamma^i_{\ jk}$	$\Gamma^i_{\ jk} = {}^s\Gamma^i_{\ jk}$

Table A.1: Christoffel symbols for the FLRW metric. Bear in mind that the Christoffel symbols are symmetric in the lower indices. ${}^s\Gamma^i_{\ jk}$ denotes the Christoffel symbol of the 3-space metric γ_{ij}.

Riemann tensor

cosmic time t	conformal time τ
$R^0_{\ i0j} = a\ddot{a}\gamma_{ij}$	$R^0_{\ i0j} = \left(\frac{a'}{a}\right)' \gamma_{ij}$
$R^i_{\ 00j} = \frac{\ddot{a}}{a}\delta_{ij}$	$R^i_{\ 00j} = \left(\frac{a'}{a}\right)' \delta_{ij}$
$R^i_{\ jkl} = \left(\kappa + \dot{a}^2\right)\left(\delta^i_k\gamma_{jm} - \delta^i_m\gamma_{jk}\right)$	$R^i_{\ jkl} = \left(\kappa + \left(\frac{a'}{a}\right)^2\right)\left(\delta^i_k\gamma_{jm} - \delta^i_m\gamma_{jk}\right)$
$R^0_{\ 00i} = R^0_{\ 0ij} = R^0_{\ ijk} = R^i_{\ 0jk} = R^i_{\ j0k} = 0$	

Table A.2: Riemann tensor components for the FLRW metric.

listed in table A.1. From the Christoffel symbols, the Riemann and Ricci tensors and the Ricci scalar

$$R^\alpha_{\mu\nu\beta} \equiv \Gamma^\alpha_{\mu\nu,\beta} - \Gamma^\alpha_{\mu\beta,\nu} + \Gamma^\lambda_{\mu\nu}\Gamma^\alpha_{\beta\lambda} - \Gamma^\lambda_{\mu\beta}\Gamma^\alpha_{\nu\lambda}\ , \tag{A.6}$$

$$R_{\mu\nu} \equiv R^\alpha_{\mu\alpha\nu}\ , \tag{A.7}$$

$$R \equiv g^{\mu\nu}R_{\mu\nu}\ , \tag{A.8}$$

listed in tables A.2 and A.3, respectively, follow. From them the Einstein's tensor reads

$$G^{\mu\nu} \equiv R^{\mu\nu} - \frac{1}{2}g^{\mu\nu}R\ . \tag{A.9}$$

It's components are listed in table A.4.

Ricci tensor

cosmic time t	conformal time τ
$R^0{}_0 = 3\frac{\ddot{a}}{a}$	$R^0{}_0 = \frac{3}{a^2}\left(\frac{a'}{a}\right)^2$
$R^i{}_j = \left\{\frac{\ddot{a}}{a} + 2\left[\left(\frac{\dot{a}}{a}\right)^2 + \frac{\kappa}{a^2}\right]\right\}\delta^i_j$	$R^i{}_j = \frac{1}{a^2}\left[\frac{a''}{a} + \left(\frac{a'}{a}\right)^2 + 2\kappa\right]\delta^i_j$
$R^0{}_i = R^i{}_0 = 0$	

Ricci scalar

$R = 6\left\{\frac{\ddot{a}}{a} + \left[\left(\frac{\dot{a}}{a}\right)^2 + \frac{\kappa}{a^2}\right]\right\}$	$R = \frac{3}{a^2}\left[2\frac{a''}{a} + \left(\frac{a'}{a}\right)^2 + 2\kappa\right]$

Table A.3: Ricci tensor components and Ricci scalar for the FLRW metric.

Einstein tensor

cosmic time t	conformal time τ
$G^0{}_0 = -3\left[\left(\frac{\dot{a}}{a}\right)^2 + \frac{\kappa}{a^2}\right]$	$G^0{}_0 = -\frac{3}{a^2}\left[\left(\frac{a'}{a}\right)^2 + \kappa\right]$
$G^i{}_j = -\left\{2\frac{\ddot{a}}{a} + \left[\left(\frac{\dot{a}}{a}\right)^2 + \frac{\kappa}{a^2}\right]\right\}\delta^i_j$	$G^i{}_j = -\frac{1}{a^2}\left[2\frac{a''}{a} - \left(\frac{a'}{a}\right)^2 + \kappa\right]\delta^i_j$
$G^0{}_i = G^i{}_0 = 0$	

Table A.4: Einstein tensor components for the FLRW metric.

A.2 Some geometric quantities in the perturbed FLRW metric

This Appendix present the perturbed geometrical quantities in the spatially flat case ($\kappa = 0$). The perturbed FLRW metric is described in conformal time by the line element

$$ds^2 = a^2 \left\{ -(1+2\phi)d\tau^2 - B_{,i}dx^i d\tau + \left[(1-2\psi)\delta_{ij} + 2E_{,ij}\right] dx^i dx^j \right\} . \tag{A.10}$$

The components of the contravariant tensor $g^{\mu\nu}$ at first order are

$$g^{00} = -a^{-2}(1-2\phi) , \qquad g^{0i} = -a^{-2}B^{,i} , \qquad g^{ij} = a^{-2}\left[(1+2\psi)\gamma^{ij} - 2E^{,ij}\right] . \tag{A.11}$$

Then, at first order, since the metric (A.10) is no longer diagonal, we have that

$$\Gamma^0_{\ 00} = \frac{1}{2}g^{0\alpha}\left(g_{\alpha 0,0} + g_{0\alpha,0} - g_{00,\alpha}\right) \approx \frac{1}{2}\left[g^{00}g_{00,0} + g^{0i}g_{00,i}\right] \approx \frac{a'}{a} + \phi' \tag{A.12}$$

All the other perturbed Christoffel symbols for the perturbed FLRW metric follow in a similar fashion. Table A.5 lists them. From them, the Riemann

Perturbed Christoffel symbols in conformal time
$\Gamma^0_{\ 00} = \frac{a'}{a} + \phi'$
$\Gamma^0_{\ i0} = \phi_{,i} - \frac{a'}{a}B_{,i}$
$\Gamma^0_{\ ij} = \left[\frac{a'}{a} - 2\frac{a'}{a}\phi - a^{-2}(a^2\psi)'\right]\delta_{ij} - B_{,ij} + a^{-2}(a^2E_{,ij})'$
$\Gamma^i_{\ 00} = \phi^{,i} - \frac{a'}{a}B^{,i} - B'^{,i}$
$\Gamma^i_{\ 0j} = \frac{a'}{a}\delta^i_j - \psi'\delta^i_j + E'^{,i}_{\ ,j}$
$\Gamma^i_{\ jk} = \frac{a'}{a}B^{,i}\delta_{jk} + 3E^{,i}_{\ ,jk} + \psi^{,i}\delta_{jk} - \psi_{,j}\delta^i_k - \psi_{,k}\delta^i_j$

Table A.5: Christoffel symbols for a general (spatially flat) perturbed FLRW metric.

tensor, Ricci tensor and Ricci scalar can be obtained. Likewise, one can derive the Einstein tensor as in the non perturbed case. Its components are listed in table A.4.

.

Einstein tensor in conformal time τ

$\delta G^0{}_0 = \frac{2}{a^2}\left[3\mathcal{H}^2\phi + \mathcal{H}\nabla^2(B+E') + 3\mathcal{H}\psi' - \nabla^2\psi\right]$
$\delta G^0{}_i = -\frac{2}{a^2}\left(\mathcal{H}\phi + \psi'\right)_{,i}$
$\delta G^i{}_j = \frac{2}{a^2}\left\{\left[\left(2\mathcal{H}' + \mathcal{H}^2\right)\phi + \mathcal{H}\phi' + 2\mathcal{H}\psi' + \psi'' + \frac{1}{2}\nabla^2 D\right]\delta^i_j + \frac{1}{2}D^{,i}_{,j}\right\}$
$D \equiv -\phi + \psi + 2\mathcal{H}\left(B + E'\right) + \left(B + E'\right)'$

Table A.6: Einstein tensor components for a general (spatially flat) perturbed FLRW metric. Recall that $\nabla^2 \equiv g^{ij}\partial_i\partial_j$.

hb		**m**					
	p	1	2	3	4	5	6
	68.3 %	1.00	2.30	3.53	4.72	5.89	7.04
	95.5 %	4.00	6.18	8.02	9.72	11.3	12.8

Table A.7: $\Delta\chi^2$ for 1σ and 2σ confidence level.

A.3 Data analysis

When measuring a set of observables $y_i(x_i)$, if the errors, σ_i, follow a Gaussian distribution, the probability of obtaining a value "y_{th}" from a given model with M free parameters θ_j, is given through the *likelihood function*

$$\mathcal{L}(\theta_i) \propto \exp^{\sum_{i=1}^{n} -\frac{\left[y_i - y_{th}(x_i;\theta_j)\right]^2}{2\sigma_i^2}} , \tag{A.13}$$

where n is the number of measured data. To obtain the most probable value for the parameters, one must maximize $\mathcal{L}(\theta_i)$ or, alternatively, minimize the χ^2 estimator defined as

$$\chi^2 \equiv \sum_{i=1}^{n} \frac{\left[y_i - y_{th}(x_i;\theta_j)\right]^2}{2\sigma_i^2} . \tag{A.14}$$

It has the advantage that if the errors in the data are normally distributed or the sample is large enough, the probability distribution for the different values of χ^2 at its minimum, χ^2_{min}, follow a chi-square distribution with $n - m$ degrees of freedom [178]. So it will have a mean $n - m$ and variance $2(n - m)$. Moreover, the quantities $\Delta\chi^2 \equiv \chi^2 - \chi^2_{min}$ are distributed as a chi-square distribution with m degrees of freedom. This allows to set the confidence region for any m parameter space -see table A.7. To maximize $\mathcal{L}$ (or minimize χ^2) within a model of a few parameters, a suitable way

to move through the m dimensional parameter grid is to use the Markov Chain Monte Carlo (MCMC). It is a random sampling method to move toward the maximum likelihood parameter region. The chain has $m+1$ elements for every step it takes, one for every parameter value plus one for their likelihood. The algorithm that operates to reach the maximum is

1. Set the initial conditions of the chain (can be random).
2. Calculate the likelihood for the parameters chosen $\mathcal{L}_1$.
3. Save the value of the parameters and the likelihood in the chain.
4. Change randomly the value of a parameter to generate a new set. The step is defined by a Gaussian distribution with rms σ_i.
5. Compute the new likelihood $\mathcal{L}_2$.
6. Save the new value of the parameters and the likelihood in the chain.
7. If $\mathcal{L}_2 > \mathcal{L}_1$ the set is accepted and the next step is taken from the actual set of parameters and proceed again to 4.
8. If $\mathcal{L}_2 < \mathcal{L}_1$ a new random number, x, is generated:
   - If $x < \mathcal{L}_2/\mathcal{L}_1$ the step is accepted and a next step is taken from the actual set and proceeds as in 4.
   - If $x > \mathcal{L}_2/\mathcal{L}_1$ the step is rejected and the next step is taken from the last accepted set of parameters, going then back to 4.

Several chains are usually run (8 in our case) to avoid the relatives maximums in the likelihood. The number of steps to have a good convergence should be around 30000 [179], but generally it suffices to fulfill the Gelman-Rubin test [180]. It consists in defining a number $\hat{R}$ that estimates the variance of the chains once they reach a stationary state. First one needs to compute the mean and the variance of the M chains $\mathbf{y}$

$$\bar{y}^j = \frac{1}{N}\sum_{i=1}^{N} y_i^j \qquad \text{and} \qquad W = \frac{1}{M(N-1)}\sum_{i,j=1}^{M,N}\left(y_i^j - \bar{y}^j\right)^2, \tag{A.15}$$

respectively, each one with $2N$ parameters (one computes the mean and variances of the last N). Thus, the mean of all the chains and the variance between them are

$$\bar{y} = \frac{1}{NM}\sum_{i,j=1}^{MN} y_i^j \qquad \text{and} \qquad B_n = \frac{1}{M-1}\sum_{j=1}^{M}\left(\bar{y}^j - \bar{y}\right)^2, \tag{A.16}$$

respectively. Then, the quantity

$$\hat{R} = \frac{\frac{N-1}{N}W + B_n\left(1+\frac{1}{M}\right)}{W}\,, \tag{A.17}$$

estimates the degree of convergence of the chain. In our work we have taken $\hat{R} < 1.1$ as the full convergence value, as in [179]. For more details and exhaustive description of the Markov Chains theory, see [181].

A.4 Legendre polynomials

These polynomials, solutions to the Legendre differential equations, are given by the expression

$$\mathcal{P}_l(\mu) = \frac{1}{2^l l!}\frac{d^l}{d\mu^l}\left(\mu^2-1\right)^l \qquad (l \in \mathcal{N}), \tag{A.18}$$

of particular interest are

$$\mathcal{P}_0(\mu) = 1\,, \quad \mathcal{P}_1(\mu) = \mu \quad \text{and} \quad \mathcal{P}_2(\mu) = \frac{3\mu^2-1}{2}. \tag{A.19}$$

A.5 Spherical Bessel functions

They are related to the Legendre Polynomials by

$$j_l(x) = \frac{(-i)^l}{2}\int_{-1}^{1} d\mu Y_{lm}^*(\theta,\phi)e^{ix\mu}\,, \tag{A.20}$$

and have the property

$$j_l(x) = (-i)^l j_l(-x). \tag{A.21}$$

A.6 Spherical harmonics

They are eigenfunctions of the angular part of the Laplacian

$$\left[\frac{1}{\sin\theta}\frac{\partial}{\partial\theta}\left(\sin\theta\frac{\partial}{\partial\theta}\right) + \frac{1}{\sin^2\theta}\frac{\partial^2}{\partial\phi^2}\right] Y_{lm}(\theta,\phi) = -l(l+1)Y_{lm}(\theta,\phi)\,, \tag{A.22}$$

and are orthogonal and normalized by

$$\int d\Omega Y_{lm}^*(\theta,\phi)Y_{lm}^*(\theta,\phi) = \delta_{ll'}\delta_{mm'}\,. \tag{A.23}$$

They are related to Legendre polynomials by

$$\mathcal{P}_l(\mu) = \frac{4\pi}{2l+1} \sum_{m=-l}^{l} Y_{lm}^*(\hat{\mathbf{x}}) Y_{lm}^*(\hat{\mathbf{x}}') \;, \tag{A.24}$$

where $\mu = \hat{\mathbf{x}} \cdot \hat{\mathbf{x}}'$.

12

References

[1] A. G. Riess *et al.* [Supernova Search Team], Astron. J. 116, 1009 (1998).

[2] S. Perlmutter *et al.* [Supernova Cosmology Project], Astrophys. J. 517, 565 (1999).

[3] P. A. R. Ade *et al.*, [Planck Collaboration], arXiv: 1303.5076 (2012).

[4] R. Durrer and R. Maartens, Gen. Relativ. Grav. 40, 301 (2008); J. A. Friemann, M. S. Turner and D. Huterer, Ann. Rev. Astron. Astrophys. 46, 385 (2008); M. Bartelmann, Rev. Mod. Phys. 82, 331 (2010); L. Amendola and Tsujikawa, *Dark Energy. Theory and Observations* (CUP, Cambridge, 2010); G. F. R Ellis, R. Maartens and M. A. H. MacCallum, *Relativistic Cosmology*, Cambridge university Press, Cambridge (2012).

[5] http://lambda.gsfc.nasa.gov/product/cobe/

[6] http://map.gsfc.nasa.gov/

[7] http://planck.esa.int

[8] S. Weinberg, *Gravitation and Cosmology*, Wiley and Sons, New York (1972).

[9] C. W. Misner, K. S. Thorne and J. A. Wheeler, *Gravitation*, Freeman, New York (1973).

[10] T. Padmanabhan, *Structure formation in the Universe*, Cambridge university Press, Cambridge (1995).

[11] Ya. B. Zel'dovich, Uspekhi. Fizika Nauk 95, 209 (1968).

[12] S. Weinberg, Rev. Mod. Phys., 61, 1 (1989); S. Weinberg, arXiv:astro-ph/0005265.

[13] P. J. Steinhardt, in *Critical Problems in Physics*, Princeton University Press, Princeton, New Jersey (1997).

[14] N. Sivanandam, Phys. Rev. D 87, 083514 (2012).

[15] T. Clifton, P. G. Ferreira, A. Padilla and C. Skordis, Physics Reports 513, 1 (2012).

[16] R. R. Caldwell, R. Dave, and P. J. Steinhardt, Phys. Rev. Lett. 80, 1582 (1998).

[17] R. R. Caldwell, M. Kamionkowski, Ann. Rev. Nucl. Part. Sci. 59, 397 (2009).

[18] R. M. Wald, General Relativity, The University of Chicago press, Chicago (1984).

[19] I. Zlatev, L. Wang, and P. Steinhardt, Phys. Rev. Lett. 82, 896 (1999).

[20] L. Amendola, Phys. Rev. D 62, 043511 (2000).

[21] W. Zimdahl, D. Pavón, L. P. Chimento, Phys. Lett. B, 521, 3 (2001).

[22] S. Tsujikawa, arXiv:1304.1961.

[23] R. R. Caldwell, Phys. Lett. B 545, 23 (2002).

[24] S. M. Carroll, M. Hoffman and M. Trodden, Phys. Rev. D 68, 023509 (2003).

[25] R. R. Caldwell, M. Kamionkowski and N. N. Weinberg, Phys. Rev. Lett. 91, 071301 (2003); B. McInnes, JHEP 0208, 029 (2002).

[26] L. P. Chimento and R. Lazkoz, Phys. Rev. Lett. 91, 211301 (2003); S. Nojiri and S. D. Odintsov, Physics Letters B 562, 3 (2003); E. Elizalde, S. Nojiri and S. D. Odintsov, Phys. Rev. D 70, 043539 (2004); T. Chiba, R. Takahashi and N. Sugiyama, Class. Quant. Grav. 22, 3745 (2005).

[27] J. Solà and H. Štefančić, Phys. Lett. B 624, 147 (2005).

[28] C. Armendariz-Picon, T. Damour and V. F. Mukhanov, Phys. Lett. B 458, 209 (1999).

[29] G.'t Hooft, "Dimensional reduction in quantum gravity", preprint gr-qc/9310026; L. Susskind, J. Math. Phys. (N.Y.) 36, 6377 (1995).

[30] A. G. Cohen, D. B. Kaplan and A.E. Nelson, Phys. Rev. Lett. 82, 4971 (1999).

[31] M. Li, Phys. Lett. B 603, 1 (2004).

[32] D. Pavón and W. Zimdahl, Phys. Lett. B 628, 206 (2005).

[33] N. Radicella and D. Pavón, JCAP10 (2010) 005.

[34] S. D. H. Hsu, Phys. Lett. B 594, 13 (2004);

[35] E. Elizalde, S. Nojiri and S. D. Odintsov, Phys. Rev. D 71, 103504 (2005).

[36] C. Gao, F. Wu, X. Chen, and Y.G. Shen, Phys. Rev. D 79, 043511 (2009).

[37] L. Xu, W. Li, and J. Lu, Mod. Phys. Lett. A 24, 1355 (2009).

[38] M. Suwa, T. Nihei, Phys. Rev. D 81, 023519 (2010).

[39] I. Duran and D. Pavón, Phys. Rev. D 83, 023504 (2011).

[40] M. Li, R-X. Miao, arXiv:1210.0966 (2012).

[41] R. Brustein, "Cosmological entropy bounds", in *String Theories and Fundamental Interactions*, Lecture Notes Physics 737, 619 (2008).

[42] A. Y. Kamenshchik, U. Moschella and V. Pasquier, Phys. Lett. B 511, 265 (2001).

[43] M. C. Bento, O. Bertolami and A. A. Sen, Phys. Rev. D 66, 043507 (2002).

[44] J. C. Fabris, H. E. S. Velten, and W. Zimdahl, Phys. Rev. D 81, 087303 (2010); O. F. Piattella, JCAP03 (2010) 012.

[45] O. F. Piattella *et al.*, JCAP01 (2010) 014.

[46] D. Bertacca *et al.*, JCAP02 (2011) 018 .

[47] J. L. Cervantes-Cota, A. Avilés and J. De-Santiago, arXiv:1303.2658

[48] A. Einstein and W. de Sitter, Nat. Acad. Sci. 18, 213 (1932).

[49] S. Dodelson, *Modern Cosmology*, Academic Press, San Diego (2003).

[50] H. Kodama and M. Sasaki, Progress of Theoretical Physics, 78 (1984).

[51] V. F. Mukhanov, H. A. Feldman and R. H. Brandenberger, Phys. Rep. 215, 203 (1992).

[52] C. P. Ma and E. Bertschinger, Astrophys. J. 455, 7 (1995).

[53] F. Bernardeau, S. Colombi, E. Gaztañaga and R. Scoccimarro, Phys. Rept. 367, 1 (2002).

[54] R. Crittenden *et al.*, Phys. Rev. Lett. 71, 324 (1993).

[55] K. A. Malik and D. Wands, Phys. Rep. 475, 1 (2009).

[56] J. Valiviita, E. Majerotto and R. Maartens, JCAP07 (2008) 020.

[57] D. Wands, J. De-Santiago and Y. Wang, Class. Quantum Grav. 29 145017 (2012).

[58] J. M. Bardeen, Phys. Rev. D 22, 1882 (1980).

[59] A. G. Riess , W. H. Press and R. P. Kirshner, Astrophys. J. 473 88 (1996).

[60] R. Amanullah *et al.* [The Supernova Cosmology Project], Astrophys. 716, 712 (2010).

[61] S. Nesseris and L. Perivolaropoulos, Phys. Rev. D 72, 123519 (2005).

[62] A. A. Penzias and R. W. Wilson, Astrophys. J. 142, 419 (1965).

[63] R. H. Dicke, P. J. E. Peebles, P. G. Roll and D. T. Wilkinson, Astrophys. J. 142, 414 (1965).

[64] R. A. Alpher and R. C. Herman, Phys. Rev. 74, 1737 (1948).

[65] W. Hu, N. Sugiyama and J. Silk, Nature 386, 37 (1997).

[66] R. K. Sachs and A. M. Wolfe, Astrophys. J. 147, 73 (1967).

[67] R. Durrer, *The Cosmic Microwave Background*, Cambridge University Press, Cambridge (2008).

[68] Y. Wang and P. Mukherjee, Astrophys. J. 650, 1 (2006).

[69] J. R. Bond, G. Efstathiou, and M. Tegmark, Mon. Not. R. Astron. Soc. 291, L33 (1997).

[70] E. Komatsu *et al.*, Astrophys. J. Supl. Series, 192, 18 (2011).

[71] M. Kowalski *et al.*, Astrophys. J. 686, 749 (2008).

[72] J. Sollerman *et al.*, Astrophys. J. 703, 1374 (2009).

[73] S. Boughn and R. Crittenden, Nature 427, 45 (2004).

[74] P. Fosalba, E. Gaztañaga and F. J. Castander, Mon. Not. Roy. Astron. Soc. 399, 1663 (2009).

[75] L. F. Abbott and M. B. Wise, Nucl. Phys. B244, 541 (1984).

[76] U. Seljak, Astrophys. J. 460, 549 (1996).

[77] M. Bartelmann and P. Schneider, Phys. Rep. 340, 291 (2001).

[78] F. Atrio-Barandela, and A. Doroshkevich, A. Klypin, Astrophys. J. 378, 1 (1991);

[79] W. Hu and N. Sugiyama, Astrophys. J. 444, 489 (1995).

[80] U. Seljak and M. Zaldarriaga, Astrophys. J. 469, 437 (1996).

[81] http://camb.info/

[82] http://class-code.net/

[83] D. J. Eisenstein *et al.* [DSS Collaboration] Astrophys. J. 633, 560 (2005).

[84] W. J. Percival *et al.*, Mon. Not. R. Astron. Soc. 401, 2148 (2010).

[85] E. A. Kazin *et al.*, Astrophys. J. 710, 1444 (2010).

[86] F. Beutler *et al.*, Mon. Not. R. Astron. Soc. 416, 3017 (2011).

[87] A. Blake *et al.*, Mon. Not. R. Astron. Soc. 418, 1707 (2011).

[88] S. Nesseris and L. Perivolaropoulos, JCAP01 (2007) 018.

[89] P. Mészáros, Astron. Astrophys. 37, 22 (1974).

[90] E. R. Harrison, Phys. Rev. D 1, 2726 (1970).

[91] Ya. B. Zel'dovich, Mon. Not. R. Astron. Soc. 160, 1 (1972).

[92] M. Tegmark and M. Zaldarriaga, Phys. Rev. D 66, 103508 (2002).

[93] S. M. D. White, J. F. Navarro, A. Evrard, and C.S. Frenk, Nature 366, 429 (1993).

[94] S. W. Allen *et al.*, Mon. Not. R. Astron. Soc. 383, 879 (2008).

[95] A. G. Riess, *et al.*, Astrophys. J. 699, 539 (2009).

[96] E. Gaztañaga, A. Cabré, and L. Hui, Mon. Not. R. Astron. Soc. 399, 1663 (2009).

[97] J. Simon, L. Verde, and R. Jiménez, Phys. Rev. D 71, 123001 (2005).

[98] D. Stern, R. Jiménez, L. Verde, M. Kamionkowski, and S.A. Stanford, JCAP02 (2010) 008.

[99] I. Duran, D. Pavón and W. Zimdahl, JCAP07 (2010) 018.

[100] W. Zimdahl and D. Pavón, Class. Quantum Grav. 24, 5461 (2007).

[101] E. Abdalla, L.R. Abramo, and J.C.C. Souza, Phys. Rev. D 82, 023508 (2010).

[102] C. Wetterich, Nucl. Phys. B 302, 668 (1988); *ibid.* Astron. Astrophys. 301, 321 (1995).

[103] L. Amendola, Phys. Rev. D 62, 043511 (2010); L. Amendola and D. Tocchini-Valentini, Phys. Rev. D 64, 043509 (2001).

[104] L. P. Chimento, A. S. Jakubi, D. Pavón, and W. Zimdahl, Phys. Rev. D., Phys. Rev. D 67, 083513 (2003).

[105] Ph. Brax and J. Martin, JCAP11 (2006) 008.

[106] S. del Campo, R. Herrera, and D. Pavón, Phys. Rev. D 78, 021302(R) (2008); *ibid.* JCAP01 (2009) 020.

[107] P. Serra *et al.*, Phys. Rev. D 80, 121302 (2009).

[108] R. A. Daly *et al.*, Astrophys. J. 677, 1 (2008).

[109] J. Dunlop *et al.*, "Old Stellar Populations in Distant Radio Galaxies", in *The Most Distant Radio Galaxies*, eds. H. J. A. Rottgering, P. Best and M. D. Lehnert, Kluwer, Dordrecht, (1999), p. 71.

[110] J. Dunlop *et al.*, Nature (London) 381, 581 (1996).

[111] H. Spinrad *et al.*, Astrophys. J. 484, 581 (1997).

[112] G. Hasinger *et al.*, Astrophys. J. 573, L77 (2002); S. Komossa and G. Hasinger, in Proc. of the Workshop "XEUS -studying the evolution of the hot universe", eds. G. Hasinger *et al.*, astro-ph/0207321.

[113] A. C. S. Friaça, J. S. Alcaniz, and J. A. S. Lima, Mon. Not. R. Astron. Soc. 362, 1295 (2005).

[114] H. Wei and S.N. Zhang, Phys. Rev. D 76, 063003 (2007).

[115] J. Cui and X. Zhang, Phys. Lett. B 690, 233 (2010).

[116] C.-G. Park, J. Hwang, J. Lee, and H. Noh, Phys. Rev. Lett. 103, 151303 (2009).

[117] Y. Gong, Phys. Rev. D 78, 123010 (2008).

[118] P. J. E. Peebles and A. Nusser, Nature 465, 565 (2010).

[119] A. Mangilli, L. Verde, and M. Beltran, JCAP10 (2010) 009.

[120] I. Duran and L. Parisi, Phys. Rev. D 85, 123538 (2012).

[121] L. Wang and P. J. Steinhardt, Astrophys. J. 508, 483 (1998).

[122] C. Armendariz-Picón, V. Mukhanov and P. J. Steinhardt, Phys. Rev. D 63, 103510 (2001).

[123] D. Pavón and B. Wang, Gen. Relativ. Grav. 41, 1 (2009).

[124] E. Komatsu *et al.*, Astrophys. J. Suppl. 180, 330 (2009).

[125] S. Lepe and F. Pena, Eur. Phys. J. C 69, 575 (2010).

[126] I. Duran, F. Atrio-Barandela, and D. Pavón, JCAP04 (2012) 008.

[127] A.R Liddle, Monthly Not. R. Astron. Soc. 351, L49 (2004).

[128] L. Amendola, M. Quartin, S. Tsujikawa, I. Waga, Phys. Rev. D 74, 023525 (2006).

[129] P. J. E. Peebles, B. Ratra, Rev. Mod. Phys. 75, 559 (2003); F. Atrio-Barandela and D. Pavón in "Dark Energy: Current Advances and Ideas", Jeong R. Choi Ed., Research Signpost, Kerala (India), p51 (2009).

[130] G. Olivares, F. Atrio-Barandela, and D. Pavón, Phys. Rev. D 71, 063523 (2005); G. Olivares, F. Atrio-Barandela, and D. Pavón, Phys. Rev. D 74, 043521 (2006).

[131] R. Lazkoz, and E. Majerotto, JCAP 07, 15 (2007); C. G. Böhmer, G. Caldera-Cabral, R. Lazkoz, and R. Maartens, Phys. Rev. D 78, 023505 (2008); J. Beltrán Jiménez, R.Lazkoz, and A. L. Maroto, Phys. Rev. D 80, 023004 (2009).

[132] G. Olivares, F. Atrio-Barandela, and D. Pavón, Phys. Rev. D 77, 063513 (2008); G. Olivares, F. Atrio-Barandela, and D. Pavón, Phys. Rev. D 77, 103520 (2008); J.-H. He, B. Wang, and Y. P. Jing, JCAP 07, 030 (2009); X.-D. Xu, J.-H. He, and B. Wang, Phys. Lett. B 701, 513 (2011); J.-H. He, B. Wang, and E. Abdalla, Phys. Rev. D 83, 063515 (2011).

[133] H-C Kao, W-L Lee, and F-L Lin, Phys. Rev. D 71, 123518 (2005); D. Rowland and I. B. Whittingham, Mon. Not. R. Astron. Soc. 390, 1719 (2008); E. M. Barboza Jr. and J. S. Alacaniz, Phys. Lett. B 666, 415 (2008); L. Amendola, M. Baldi, and C. Wetterich, Phys. Rev. D 78, 023015 (2008); M. Li, X-D Li, S. Wang, Y. Wang, and X. Zhang, JCAP 12, 014 (2009); Y. Chen, Z-H Zhu, L. Xu and J. S. Alcaniz, Phys. Lett. B 698, 175 (2011); S. del Campo, J. C. Fabris, R. Herrera, and W. Zimdahl, Phys. Rev. D 83, 123006 (2011); L. P. Chimento, M. Forte, and M. G. Richarte, Mod. Phys. Lett. A 28, 1250235 (2013).

[134] A. Kashlinsky, and B. J. T. Jones, Nature 349, 753 (1991).

[135] M. Strauss, and J. Willick, Phys. Rep. 261, 271 (1995).

[136] B. M. Schaefer, G. A. Caldera-Cabral, and R. Maartens (2008), arXiv:0803.2154.

[137] R. G. Crittenden and N. Turok, Phys. Rev. Lett. 76, 575 (1996); A. Cooray, Phys. Rev. D 65, 103510 (2002).

[138] D. Larson *et al.*, Astrophys. J. Supplement Series 192, 16 (2011).

[139] A. Kashlinsky, F. Atrio-Barandela, D. Kovecski, H. Ebeling, Astrophys. J. 686, L49 (2008); R. Watkins, H. A. Feldman, M. J. Hudson, Mon. Not. R. Astron. Soc. 392, 743 (2009); A. Kashlinsky, F. Atrio-Barandela, H. Ebeling, A. Edge, D. Kovecski, Astrophys. J. 712, L81 (2010); A. Kashlinsky, F. Atrio-Barandela, H. Ebeling, Astrophys. J. 732, 1 (2011); J. Colin, R. Mohayaee, S. Sarkar, A. Shafieloo, Mon. Not. R. Astron. Soc. 414, 264 (2011); S. J. Turnbull *et al.*, Mon. Not. R. Astron. Soc. 420, 447 (2012).

[140] G. Olivares, F. Atrio-Barandela and D. Pavón, Phys. Rev. D 77, 103520 (2008); R. Kimura, T. Kobayashi and K. Yamamoto, Phys. Rev. D 85, 123503 (2012).

[141] B. Wang, Y. Gong and E. Abdalla, Phys. Lett. B 624, 141 (2005).

[142] G. Caldera-Cabral, R. Maartens, and B. M. Schaefer, JCAP07 (2009) 027.

[143] F. Atrio-Barandela, and A. Doroshkevich, Astrophys. J. 420, 26 (1994); A. G. Doroshkevich, and R. Schneider, Astrophys. J. 469, 445 (1996); V. Mukhanov, Int. J. Theoretical Phys. 43, 623 (2004).

[144] The data can be downloaded from http://lambda.gsfc.nasa.gov/.

[145] H. B. Sandvik, M. Tegmark, M. Zaldarriaga and I. Waga, Phys. Rev. D 69, 123524 (2004);

[146] S. del Campo, I. Duran, R. Herrera and D. Pavón, Phys. Rev. D 86, 083509 (2012);

[147] M. Li, X.D. Li, S. Wang, and Y. Wang, Commun. Theor. Phys. 56, 525 (2011).

[148] Ø. Elgarøy and T. Multamäki, JCAP 09(2006)002.

[149] C. A. Shapiro and M. S. Turner, Astrophys. J. 649, 563 (2006).

[150] J. V. Cunha and J. A. S. Lima, Mon. Notices R. Astron. Soc. 390, 210 (2008).

[151] L. Xu and J. Lu, Mod. Phys. Lett. A 24, 369 (2009).

[152] B. Santos, J. C. Carvalho, and J.S. Alcaniz, arXiv:1009.2733.

[153] R. Nair, S. Jhingan, and D. Jain, JCAP 01(2012)018.

[154] E. E. O. Ishida, R. R. R. Reis, A. V. Toribio, and I. Waga, Astroparticle Physics 28, 547 (2008).

[155] R. Giostri, M. Vargas dos Santos, I. Waga, R. R. R. Reis, M. O. Calvão, and B.L. Lago, JCAP03 (2012) 027.

[156] H. B. Callen, *Thermodynamics*, J. Wiley, New York (1960).

[157] C. A. Egan and C.H. Lineweaver, Astrophys. J. 710, 1825 (2010).

[158] D. Bak and S.J. Rey, Class. Quantum Grav. 17, L83 (2000).

[159] B. Wang, Y. Gong, and E. Abdalla, Phys. Rev. D. 74, 083520 (2006).

[160] N. Radicella and D. Pavón, Gen. Relativ. Grav. 44, 685 (2012).

[161] D. J. Eisenstein and W. Hu, Astrophys. J. 496, 605 (1998).

[162] C. Blake *et al.*, Mon. Not. R. Astron. Soc. 425, 405 (2012).

[163] M. Chevallier and D. Polarski, Int. J. Mod. Phys. D 10, 213 (2001).

[164] E. V. Linder, Phys. Rev. Letters 90, 091301 (2003).

[165] Z. Li, P. Wu, and H. Yu, Phys. Letters B 695, 1 (2011).

[166] V. Cardenas, and M. Rivera, Phys. Lett. B 710, 251 (2012).

[167] C.-J. Wu, C. Ma, and T.-J. Zhang, Astrophys. J. 753, 97 (2012).

[168] A.G. Riess *et al.*, Astrophys. J. 659, 98 (2007).

[169] J. Lu, L. Xu, and M. Liu, Phys. Letters B 699, 246 (2011).

[170] R. A. Daly Advances in Space Research 35, 116 (2005).

[171] T.M. Davis *et al.*, Astrophys. J. 666, 716 (2007).

[172] R.A. Daly *et al.*, Astrophys. J. 691, 1058 (2009).

[173] A. Shafieloo, V. Sahni and A. A. Starobinsky, Phys. Rev. D 80, 101301 (2009).

[174] Z. Li, P. Wu, and H. Yu, Phys. Lett. B 695, 1 (2011).

[175] A. C. C. Guimarães and J.A.S. Lima, Class. Quantum Grav. 28, 125026 (2011).

[176] C. Zuñiga-Vargas, W.S. Hipólito-Ricaldi, and W. Zimdahl, JCAP 04 (2012) 032.

[177] A. C. C. Guimarães, J. V. Cunha, and J. A. S. Lima, JCAP 10 (2009) 010.

[178] W. H. Press, S. A. Teukolski, W. T. Vetterling and B. P. Flannery, *Numerical Recipes*, 3rd Edition, Cambridge University Press, Cambridge (2007).

[179] L. Verde *et al.*, Astrophys. J. Suppl. 148, 195 (2003).

[180] A. Gelman and D. Rubin, Statistical Science 7, 457 (1992).

[181] W. R. Gilks, S. Richardson and D. J. Spielhalter, *Markov Chain Monte Carlo in Practice*, Chapman & Hall/CRC, Boca Ratón, Florida (1996).